

# REPORT DOCUMENTATION PAGE

Form Approved  
OMB NO. 0704-0188

Public Reporting burden for this collection of information is estimated to average 1 hour per response, including the time for reviewing instructions, searching existing data sources, gathering and maintaining the data needed, and completing and reviewing the collection of information. Send comment regarding this burden estimates or any other aspect of this collection of information, including suggestions for reducing this burden, to Washington Headquarters Services, Directorate for Information Operations and Reports, 1215 Jefferson Davis Highway, Suite 1204, Arlington, VA 22202-4302, and to the Office of Management and Budget, Paperwork Reduction Project (0704-0188), Washington, DC 20503.

1. AGENCY USE ONLY (Leave Blank)	2. REPORT DATE October 30, 2002	3. REPORT TYPE AND DATES COVERED Final Report, 8/1/1998 – 10/31/2002	
4. TITLE AND SUBTITLE Microstructure and Dynamic Behavior Correlation in Two-phase TiB <sub>2</sub> +Al <sub>2</sub> O <sub>3</sub> Ceramic		5. FUNDING NUMBERS DAAG55-98-1-0454	
6. AUTHOR(S) Naresh N. Thadhani and Min Zhou		8. PERFORMING ORGANIZATION REPORT NUMBER 10. SPONSORING / MONITORING AGENCY REPORT NUMBER 37763-MS .1	
7. PERFORMING ORGANIZATION NAME(S) AND ADDRESS(ES) School of Materials Science and Engineering Georgia Institute of Technology Atlanta, GA 30332-0245			
9. SPONSORING / MONITORING AGENCY NAME(S) AND ADDRESS(ES) U. S. Army Research Office P.O. Box 12211 Research Triangle Park, NC 27709-2211			
11. SUPPLEMENTARY NOTES The views, opinions and/or findings contained in this report are those of the author(s) and should not be construed as an official Department of the Army position, policy or decision, unless so designated by other documentation.			
12 a. DISTRIBUTION / AVAILABILITY STATEMENT Approved for public release; distribution unlimited.		12 b. DISTRIBUTION CODE	
13. ABSTRACT (Maximum 200 words)  The high-strain-rate deformation and damage response of four types of microstructurally-biased two-phase (nominally 30:70) TiB <sub>2</sub> +Al <sub>2</sub> O <sub>3</sub> ceramics, produced by SHS or mechanical milling techniques, have been investigated in this work.. The microstructural-bias includes differences in phase (grain) size and phase distribution, such that in one case a continuous (interconnected) TiB <sub>2</sub> network surrounds the Al <sub>2</sub> O <sub>3</sub> phase (qualitatively termed 'T@A'), and in the other case the TiB <sub>2</sub> and Al <sub>2</sub> O <sub>3</sub> phases are interdispersed and uniformly inter-twined with each other (qualitatively termed 'TinA'). The work performed has focussed on correlation of time-resolved measurements of dynamic spall and compressive yield strengths obtained from gas gun experiments and from split-Hopkinson bar experiments, with quantitative determination of the two-phase biased microstructure. Micromechanical modeling based on a cohesive surface formulation model that provides explicit account for arbitrary microstructures and arbitrary fracture patterns has also been developed to study the deformation and damage sub-structure evolution during impact loading. Deterministic and stochastic characterization of fracture resistance has also been performed and implemented			
14. SUBJECT TERMS two-phase ceramics, biased microstructures, high-strain-rate damage response, dynamic mechanical properties		15. NUMBER OF PAGES	
		16. PRICE CODE	
17. SECURITY CLASSIFICATION OR REPORT UNCLASSIFIED	18. SECURITY CLASSIFICATION ON THIS PAGE UNCLASSIFIED	19. SECURITY CLASSIFICATION OF ABSTRACT UNCLASSIFIED	20. LIMITATION OF ABSTRACT UL

NSN 7540-01-280-5500

Standard Form 298 (Rev.2-89)  
Prescribed by ANSI Std. Z39-18  
298-102

20030321 092

---

REPORT DOCUMENTATION PAGE (SF298)  
(Continuation Sheet)

---

ARO PROJECT No. DAAG55-98-1-0454  
*MICROSTRUCTURE AND DYNAMIC BEHAVIOR*  
*CORRELATION IN TWO-PHASE  $TiB_2-Al_2O_3$  CERAMIC*  
(*P.I.s Naresh Thadhani and Min Zhou, Georgia Tech, Atlanta*)

## 1. INTRODUCTION

The dynamic, high-strain-rate deformation behavior of materials (and consequently their ballistic performance) is dramatically influenced by their microstructural characteristics, including phase size, phase morphology, composition and texture. Such a trend has been revealed not only for steels used as heavy armor, but also for ceramics considered for lightweight armor applications [1]. In addition to their low density, ceramics exhibit superior hardness and high compressive strength that enables erosion and "interface defeat" of projectiles. This mechanism makes ceramics highly desirable for use as armor materials. Over the last thirty years a number of studies on ballistic performance and dynamic behavior [1-19] have been performed on various ceramics (e.g., AlN,  $Al_2O_3$ ,  $B_4C$ , SiC,  $TiB_2$ , WC,  $ZrO_2$ ). These studies have suggested that the desirable characteristics of ceramics that are beneficial for the defeat of projectiles include the combination of high yield strength or hardness, high tensile spall strength, high fracture toughness, high Poisson's ratio, and high coefficient of friction [15]. The properties typically measured to characterize the dynamic behavior of ceramics are the Hugoniot Elastic Limit ( $\sigma_{HEL}$ ) and spall strength. In general, the spall strength is lower than the elastic limit. Materials such as  $TiB_2$  have a spall strength that decreases with increasing impact stress and becomes negligible at the  $\sigma_{HEL}$ . In contrast,  $Al_2O_3$  maintains its original spall strength even at impact stress levels that exceed the  $\sigma_{HEL}$  [3].

It has been demonstrated that SiC and  $TiB_2$  exhibit the most desirable ballistic properties based on results of experiments performed to determine the transition between interface defeat and penetration involving W-projectiles [14-16]. The impact velocity for dwell/penetration transition for SiC and  $TiB_2$  is higher than that for  $B_4C$ , in spite of the higher yield strength of the latter. This trend is consistent with the predictions from the dwell/penetration transition model [17] which accounts for damage mechanism based on the extension of mode-I wing cracks. The predictions illustrate that SiC and  $TiB_2$  ceramics have the ability to suppress the formation of wing cracks due to plastic relaxation of pre-existing flaws, while  $B_4C$  shows a brittle behavior dominated by growth of wing cracks. Brittle fracture is also expected to dominate the behavior of  $Al_2O_3$ . Measurements of shock wave profiles have also illustrated the ability of SiC and  $TiB_2$  ceramics to undergo deformation-induced hardening [18], which may give rise to improved ballistic properties.

Most dynamic behavior studies performed to-date, have focused on single-phase monolithic ceramics, although ceramics with glassy (impurity) phases, e.g., AD85  $Al_2O_3$ , have also been investigated. In such ceramics, the presence of intergranular oxide glass has been shown to significantly lower the tensile (spall) strength, and therefore, the fracture resistance [19]. Dynamic behavior of ductile metal-matrix composites, e.g., Al-alloys consisting of

**DISTRIBUTION STATEMENT A**  
Approved for Public Release  
Distribution Unlimited

embedded ceramic particles, has been studied to a limited extent [20]. It has been shown that both, the dynamic yield strength and the spall strength are reduced, in comparison to strength increases observed in particle-reinforced composite materials under quasi-static loading conditions. The composite structure acts as a mechanical energy trap due to scattering of waves from incoherent boundaries and interfaces between the matrix and reinforcement phases having dissimilar shock impedance. The high-strain-rate mechanical behavior of ceramic-ceramic composites shows a strain rate dependence significantly different from that observed in metal-matrix composites.

Dynamic behavior of ceramic-composites has been limited only to the study of two-phase  $\text{Al}_2\text{O}_3+\text{TiB}_2$  ceramics (70/30 mass ratio). Past work on these two-phase ceramics has revealed an 80% increase in compressive strength with increasing strain rate (3.5 GPa at  $10^4 \text{ s}^{-1}$  to 5.8 GPa at  $10^3 \text{ s}^{-1}$ ) as shown in Fig 1(a) [21]. In addition, as illustrated in Figure 1 (b), the two-phase  $\text{Al}_2\text{O}_3+\text{TiB}_2$  ceramics have superior static and dynamic mechanical properties than their monolithic constituents [21-23]. The  $\text{Al}_2\text{O}_3+\text{TiB}_2$  ceramics have also shown better penetration resistance than monolithic  $\text{Al}_2\text{O}_3$ , and the system in which  $\text{TiB}_2$  is an interconnected phase surrounding  $\text{Al}_2\text{O}_3$  has been shown to exhibit a superior ballistic performance compared with the system in which the two phases are simply uniformly interdispersed [21,24]. Micromechanical simulations have also demonstrated the effect of microstructural bias on failure resistance [25,26]. However, the influence of micro-structural bias on the fundamental dynamic properties of these ceramics has not been fully established.

The objective of the present work is to quantitatively characterize the microstructure and the high-strain-rate deformation and damage response of four types of microstructurally-biased, two-phase  $\text{TiB}_2+\text{Al}_2\text{O}_3$  ceramics. The microstructural bias of the four ceramics falls into two morphological categories. The first category involves a continuous (interconnected)  $\text{TiB}_2$  network that surrounds  $\text{Al}_2\text{O}_3$  (qualitatively termed 'T@A') and the second category involves  $\text{TiB}_2$  and  $\text{Al}_2\text{O}_3$  phases that are interdispersed and uniformly inter-twined with each other (qualitatively termed 'TinA') [21,27]. Quantitative stereology methods [28] were used to determine the two-phase biased microstructure. Normal plate-impact experiments, as well as Hopkinson bar experiments were performed to measure the compressive yield strength, the Hugoniot Elastic Limit ( $\sigma_{\text{HEL}}$ ) and the tensile spall strengths of the materials. The measured responses were then correlated with the microstructure morphological characteristics and the phase size scales. Micromechanical modeling based on a cohesive surface formulation model that provides explicit account for arbitrary microstructures and arbitrary fracture patterns was also developed to study the deformation and damage sub-structure evolution during impact loading. Deterministic and stochastic characterization of fracture resistance has also been performed and implemented.

The main findings of the work performed in this investigation, are compiled in the following sections. Only a brief description is provided along with a listing of thesis and papers describing the work. Copies of the abstracts of thesis and reprints of some of the key papers are attached in the appendix.

## 2. MICROSTRUCTURAL CHARACTERIZATION AND QUANTIFICATION

Four types of microstructurally-biased  $\text{TiB}_2+\text{Al}_2\text{O}_3$  ceramics have been produced: (a) SHS with  $\text{TiB}_2$  surrounding  $\text{Al}_2\text{O}_3$  (T@A), (b) SHS with intermixed  $\text{TiB}_2$  and  $\text{Al}_2\text{O}_3$  (TinA), (c) MM with  $\text{TiB}_2$  surrounding  $\text{Al}_2\text{O}_3$  (T@A), and (d) MM with intermixed  $\text{TiB}_2$  and  $\text{Al}_2\text{O}_3$  (TinA). An automated quantitative metallography technique was developed to determine the connectivity of the  $\text{TiB}_2$  phase, based on measurement of the average integral curvature defined by:  $k_{ave} = 2\pi N_A^{net} / \ell = 2\pi N_A^{net} / (P_h + P_p)$ , where,  $N_A^{net}$  is the net numbers of loops of phase A per unit area,  $\ell$  is the mean linear intercept, and  $P_h$  and  $P_p$  are numbers of  $\text{TiB}_2$  particles and  $\text{Al}_2\text{O}_3$  holes, respectively. The number counts and perimeters for size measurement are performed on several montages of micrographs obtained from both planar and cross-sectional surfaces using the SCOPE-PRO software and MATERIALS-PRO software, which allow reliable and repeatable measurements. Quantitative metallography measurements performed on the four sets of samples with the different microstructure illustrate that the samples do not reveal a 100% microstructural bias. The general trend reveals Sample 'C' having the most interconnected  $\text{TiB}_2$  phase surrounding the  $\text{Al}_2\text{O}_3$  phase, and Sample 'D' having the least interconnected  $\text{TiB}_2$ .

### Published Work:

1. Louis Ferranti, Processing and Quantitative Microscopy Characterization of Microstructurally-biased  $\text{TiB}_2+\text{Al}_2\text{O}_3$  two-phase ceramic, M.S. thesis, Georgia Institute of Technology, October 2001.
2. G. Kennedy, L. Ferranti, R. Russell, M. Zhou, and N.N. Thadhani, Dynamic High-Strain-Rate Behavior of Microstructurally-biased two-phase  $\text{TiB}_2+\text{Al}_2\text{O}_3$  Ceramics, Journal of Applied Physics vol.91, no.4 p.1921-7, 2002.
3. L. Ferranti and N.N. Thadhani, "Quantitative Characterization of Microstructurally Biased Two-Phase  $\text{TiB}_2+\text{Al}_2\text{O}_3$  Ceramics Using Mean Integral Curvature," submitted to Metallurgical Transactions, October 2002.

## 3. CHARACTERIZATION OF HIGH-STRAIN-RATE MECHANICAL PROPERTIES

**Hugoniot Elastic Limit:** Measurements of the Hugoniot Elastic Limit ( $\sigma_{HEL}$ ) were obtained from gas-gun impact experiments conducted at a nominal 750 m/s impact velocity. Input- and backer-wave stress profiles were recorded using the PVDF stress gauges, from which the Hugoniot elastic limit ( $\sigma_{HEL}$ ) and wave-speed were determined. The Hugoniot Elastic Limit ( $\sigma_{HEL}$ ), a measure of the axial stress at which a solid loaded under uniaxial compression can no longer support elastic deformation and begins to flow plastically or undergoes fracture, is observed to be a strong function of the microstructure including the phase size. The  $\sigma_{HEL}$  is found to be the lowest for Sample-B ( $4.4 \pm 1.2$  GPa), due to its ~4% porosity and highest for Sample-D ( $8.5 \pm 4.5$  GPa), although its standard deviation is also large. The  $\sigma_{HEL}$  values reported previously by Grady for  $\text{TiB}_2$  is 9-18 GPa, and ~6.7 for  $\text{Al}_2\text{O}_3$ . While ( $\sigma_{HEL}$ ) identifies the limit of elastic response in a dynamic (shock) uniaxial strain loading, it is also common to assume a von Mises condition of yield which asserts that yield initiates when the second deviatoric stress invariant attains a critical value. Through this formalism, the yield stress in simple tension can be easily related to ( $\sigma_{HEL}$ ) through  $\sigma_{YS} = 2 (C_s^2 / C_L^2) \times (\sigma_{HEL})$ . The yield stress in simple tension ( $\sigma_{YS}$ ) for the various samples follows the same trend as the Hugoniot Elastic Limit.

**Tensile (spall) Strength Properties:** Tensile (spall) strength experiments were performed (using VISAR interferometry) on samples of microstructure 'A' at impact velocities corresponding to input stresses above and below the HEL, and on samples of microstructures 'C' and 'D' under elastic loading conditions to ensure that the compression-induced damage does not influence the tensile response. The spall strength for sample-'A' is 0.320 MPa at input stresses of 3.7 and 7.9 GPa. However, with input stress increasing to 11.8 GPa, the tensile spall strength decreases to 0.160 GPa. Tensile spall experiments were also performed on samples of microstructures 'C' and 'D', at an input stress of ~3.8 GPa. A spall strength of 0.311 GPa for Sample-C and 0.222 GPa for Sample- D, was observed. The comparison of spall test results between Sample-C and Sample-D illustrate that the latter sample with dispersed microstructure, has a lower spall strength, while ceramic with  $TiB_2$  interconnected microstructure has a higher spall strength. The measured high value of the spall strength of the two-phase ceramic is similar to the published spall strength of  $TiB_2$  (0.33 GPa) but lower than that of  $Al_2O_3$  (0.45 GPa).

**Dynamic Compressive Strength:** Experimental measurement of dynamic compressive strength has been carried out at strain rates of  $10^3$  s<sup>-1</sup>, using the split Hopkinson compression bar configuration. Experiments conducted so far show that the compressive strength of the four materials is between 4-5.2 GPa. There is clearly a dependence of strength on microstructure. It is found that there is up to 15% difference in strength between the four microstructures, and order of decreasing strength is similar to that predicted by numerical simulations.

**Published Work:**

1. A. Keller, "An Experimental Analysis of the Dynamic Failure Resistance of  $TiB_2/Al_2O_3$  Composites," Georgia Tech M.S. Thesis, October 2000.
2. Greg Kennedy, "Effect of Microstructural Bias on the High Strain Rate Properties of  $TiB_2+Al_2O_3$  two-phase ceramic," M.S. thesis (in progress).
3. G. Kennedy, J. Zhai, R. Russell, M. Zhou, and N. Thadhani, High-Strain-Rate Behavior of Microstructurally-biased Two-Phase  $TiB_2+Al_2O_3$  Ceramics, *Proceedings of the 24th Annual Cocoa Beach Conference of The American Ceramic Society*, January 23-28, 2000.
4. Greg Kennedy, Rod Russell, Louis Ferranti, and Naresh Thadhani, "Fabrication of Microstructurally-biased Two-phase  $TiB_2+Al_2O_3$  Ceramics and their Dynamic Properties," in *Processing and Fabrication of Advanced Materials*, ASM Conf. Proc., eds. T.S. Srivatsan and R.A. Varin.
5. Greg Kennedy, Andrew Keller, Rod Russell, Louis Ferranti, Jun Zhai, Min Zhou, and Naresh Thadhani; "Dynamic Mechanical Properties of Microstructurally-biased Two-phase  $TiB_2+Al_2O_3$  Ceramics," in *Proc. of EXPLOMET 2000 Conference*, eds. K.P. Staudhammer, L.E. Murr, and M.A. Meyers.
6. G. Kennedy, L. Ferranti, R. Russell, M. Zhou, and N. Thadhani, Dynamic High-Strain-Rate Mechanical Behavior of Microstructurally-biased Two-Phase  $TiB_2+Al_2O_3$  Ceramics, *J. Applied Physics*, 91(4), 1921-1927, 2002;
7. A. R. Keller and M. Zhou, Effect of Microstructure on Dynamic Failure Resistance of  $TiB_2/Al_2O_3$  Ceramics, submitted to *Journal of the American Ceramic Society*, 2001;
8. A. Keller and M. Zhou, Microscopic and Nanoscopic Fracture in Heterogeneous in a Heterogeneous Material System, *Proceedings of 2002 SEM Annual Conf. and Expo. on Exp. & Appl. Mechanics*, June 10-12, 2002;
9. A. Keller, G. Kennedy, L. Ferranti, M. Zhou, and N. Thadhani, Correlation of Dynamic Behavior with Microstructural-bias in Two-phase  $TiB_2+Al_2O_3$  Ceramics, *Impact Engineering and Application*, *Proceedings of the Fourth International Symposium on Impact Engineering (ISIE/4)*, pp. 321-326, July 16-18, Kumamoto, Japan, Elsevier, 2001;
10. A. R. Keller and M. Zhou, Experimental characterization of the dynamic failure of  $TiB_2/Al_2O_3$  composites, *Shock compression of condensed matter-2001*, ed. M. D. Furnish, N. N. Thadhani, and Y. Horie, American Institute of Physics, 795-798, 2001;

11. G. Kennedy, L. Ferranti, R. Russell, M. Zhou, and N. Thadhani, Influence of microstructural bias on the Hugoniot elastic limit and spall strength of two-phase TiB<sub>2</sub>+Al<sub>2</sub>O<sub>3</sub> ceramics, Shock compression of condensed matter-2001, ed. M. D. Furnish, N. N. Thadhani, and Y. Horie, American Institute of Physics, 755-758, 2001

#### **4. MICROMECHANICAL MODELING OF DYNAMIC BEHAVIOR**

A micromechanical model that explicitly describes arbitrary microstructures and arbitrary fracture patterns was formulated using the cohesive finite element (CFEM) method. The approach uses both a constitutive law for the bulk solid constituents and a constitutive law for fracture surfaces. The model based on a phenomenological characterization for atomic forces on potential crack/microcrack surfaces was used to analyze dynamic crack propagation in the four types of TiB<sub>2</sub>+Al<sub>2</sub>O<sub>3</sub> samples. The analysis considered arbitrary phase distributions in the actual microstructures of the two-phase ceramics. Numerical results reveal that interfacial bonding strength significantly influences failure. At the same load intensity, weak interfacial bonding strengths give rise to microcrack nucleation and coalescence. In the presence of strong interfacial bonding strength, the extension and branching of a main crack is found to be the primary failure mode. Crack speeds are found to be <60% of the Rayleigh wave speed of the more compliant constituent in the microstructure. Analyses of the effects of microstructure on dynamic fracture resistance showed that (a) fine phase size is beneficial to enhancement of fracture resistance and significant gains (up to 60%) in fracture resistance can be realized through manipulation of phase morphology and phase distribution.

#### **Published Work:**

1. Jun Zhai, "Micromechanical Modeling of Dynamic Fracture in Heterogeneous Materials," Ph.D. dissertation, Georgia Institute of Technology, January 2000.
2. J. Zhai and M. Zhou, "Finite Element Analysis of Micromechanical Failure Modes in Heterogeneous Brittle Solids", *International Journal of Fracture*, special issue on *Failure Mode Transition in Solids*, R. C. Batra, Y. D. S. Rajapakse, and A. J. Rosakis, eds., 101, pp. 161-180, 2000;
3. M. Zhou and J. Zhai, Micromechanical Characterization of the Fracture Resistance of A TiB<sub>2</sub>/Al<sub>2</sub>O<sub>3</sub> Ceramic Composite System, American Ceramic Society 102nd Annual Meeting & Exposition, St. Louis, Missouri, April 30 - May 3, 2000;
4. J. Zhai, V. Tomar and M. Zhou, (2002) Explicit Analysis of Microscopic Fracture Processes Using a Cohesive Finite Element Method, Part I-Mesh Dependence and Convergence, *manuscript in preparation*.
5. J. Zhai, V. Tomar and M. Zhou, (2002) Explicit Analysis of Microscopic Fracture Processes Using a Cohesive Finite Element Method, Part II-Numerical Results, *manuscript in preparation*.

#### **5. STOCHASTIC CHARACTERIZATION OF FRACTURE RESISTANCE**

A combined deterministic and stochastic framework for explicit fracture modeling at the microscopic scale has been developed and implemented. This framework allows the variations in constitutive and interfacial properties of materials to be quantified. This description is used to analyze the stochastic outcome of deformation and failure. The expected value and range of variation of energy dissipation rate can be obtained. It is found that a 10% variation in stiffness and cohesive strengths can lead to much higher levels of variation in failure resistance.

## **6. SUMMARY OF RESULTS**

The two-phase  $TiB_2+Al_2O_3$  ceramics made either by the SHS or mechanical milling methods, reveal differences in microstructure which qualitatively show  $TiB_2$  as a continuous (interconnected) phase surrounding  $Al_2O_3$  (T@A), or the  $TiB_2$  and  $Al_2O_3$  intermixed with each other (TinA). Quantitative microscopy analysis methods based on the determination of the integral curvature, as a measure of phase connectivity, have been developed to quantitatively characterize the samples of varying degrees of microstructural bias. Normal plate-impact experiments, as well as Hopkinson bar experiments were performed to measure the compressive yield strength, the Hugoniot Elastic Limit ( $\sigma_{HEL}$ ) and the tensile spall strengths of the materials. The measured responses exhibit a strong correlation with the microstructure morphological characteristics and the phase size scales. Micromechanical modeling based on a cohesive surface formulation model that provides explicit account for arbitrary microstructures and arbitrary fracture patterns has been developed to study the deformation and damage sub-structure evolution during impact loading. The Ph.D. and M.S. thesis, as well as publications and presentations resulting from this work, are listed below.

## **7. GRADUATE THESIS (COMPLETED and IN PROGRESS)**

1. Jun Zhai, "Micromechanical Modeling of Dynamic Fracture in Heterogeneous Materials," Ph.D. dissertation, Georgia Institute of Technology, January 2000. *(currently Research Scientist at Motorola)*
2. A. Keller, "An Experimental Analysis of the Dynamic Failure Resistance of  $TiB_2/Al_2O_3$  Composites," Georgia Tech M.S. Thesis, October 2000 (currently at Ford Motor Company)
3. Louis Ferranti, Processing and Quantitative Microscopy Characterization of Microstructurally-biased  $TiB_2+Al_2O_3$  two-phase ceramic, M.S. thesis, October 2001 (currently Ph.D. student at Georgia Tech working on graduate research internship through EGLIN AFB, Florida).
4. Greg Kennedy, "Effect of Microstructural Bias on the High Strain Rate Properties of  $TiB_2+Al_2O_3$  two-phase ceramic," M.S. thesis (in final stage of thesis writing; currently on a 3-month international research experience program funded through an award from Kumamoto University in Japan).
5. Vikas Tomar, "Stochastic analysis of failure resistance of two-phase ceramics", PhD thesis in progress.

## **8. LIST OF PUBLICATIONS**

1. J. Zhai and M. Zhou, "Finite Element Analysis of Micromechanical Failure Modes in Heterogeneous Brittle Solids", *International Journal of Fracture*, special issue on *Failure Mode Transition in Solids*, R. C. Batra, Y. D. S. Rajapakse, and A. J. Rosakis, eds., **101**, pp. 161-180, 2000;
2. M. Zhou and J. Zhai, Micromechanical Characterization of the Fracture Resistance of A  $TiB_2/Al_2O_3$  Ceramic Composite System, American Ceramic Society 102nd Annual Meeting & Exposition, St. Louis, Missouri, April 30 - May 3, 2000;
3. G. Kennedy, J. Zhai, R. Russell, M. Zhou, and N. Thadhani, High-Strain-Rate Behavior of Microstructurally-biased Two-Phase  $TiB_2+Al_2O_3$  Ceramics, *Proceedings of the 24th Annual Cocoa Beach Conference of The American Ceramic Society*, January 23-28, 2000;
4. Greg Kennedy, Rod Russell, Louis Ferranti, and Naresh Thadhani, "Fabrication of Microstructurally-biased Two-phase  $TiB_2+Al_2O_3$  Ceramics and their Dynamic Properties," in

Processing and Fabrication of Advanced Materials, ASM Conf. Proc., eds. T.S. Srivatsan and R.A. Varin.

5. Greg Kennedy, Andrew Keller, Rod Russell, Louis Ferranti, Jun Zhai, Min Zhou, and Naresh Thadhani; "Dynamic Mechanical Properties of Microstructurally-biased Two-phase  $TiB_2+Al_2O_3$  Ceramics," in Proc. of EXPLOMET 2000 Conference, eds. K.P. Staudhammer, L.E. Murr, and M.A. Meyers.
6. G. Kennedy, L. Ferranti, R. Russell, M. Zhou, and N. Thadhani, Dynamic High-Strain-Rate Mechanical Behavior of Microstructurally-biased Two-Phase  $TiB_2+Al_2O_3$  Ceramics, *J. Applied Physics*, 91(4), 1921-1927, 2002;
7. A. R. Keller and M. Zhou, Effect of Microstructure on Dynamic Failure Resistance of  $TiB_2/Al_2O_3$  Ceramics, submitted to *Journal of the American Ceramic Society*, 2001;
8. J. Zhai, V. Tomar and M. Zhou, (2002) Explicit Analysis of Microscopic Fracture Processes Using a Cohesive Finite Element Method, Part I-Mesh Dependence and Convergence, *manuscript in preparation*.
9. J. Zhai, V. Tomar and M. Zhou, (2002) Explicit Analysis of Microscopic Fracture Processes Using a Cohesive Finite Element Method, Part II-Numerical Results, *manuscript in preparation*.
10. A. Keller and M. Zhou, Microscopic and Nanoscopic Fracture in Heterogeneous in a Heterogeneous Material System, Proceedings of 2002 SEM Annual Conf. and Expo. on Exp. & Appl. Mechanics, June 10-12, 2002;
11. A. Keller, G. Kennedy, L. Ferranti, M. Zhou, and N. Thadhani, Correlation of Dynamic Behavior with Microstructural-bias in Two-phase  $TiB_2+Al_2O_3$  Ceramics, Impact Engineering and Application, Proceedings of the Fourth International Symposium on Impact Engineering (ISIE/4), pp. 321-326, July 16-18, Kumamoto, Japan, Elsevier, 2001;
12. M. Zhou, Numerical Simulation of Micro and Nano Scale Fracture, Proceedings of The 10<sup>th</sup> International Congress of Fracture, December 2-7, 2001, Honolulu, Hawaii;
13. A. R. Keller and M. Zhou, Experimental characterization of the dynamic failure of  $TiB_2/Al_2O_3$  composites, Shock compression of condensed matter-2001, ed. M. D. Furnish, N. N. Thadhani, and Y. Horie, American Institute of Physics, 795-798, 2001;
14. G. Kennedy, L. Ferranti, R. Russell, M. Zhou, and N. Thadhani, Influence of microstructural bias on the hugoniot elastic limit and spall strength of two-phase  $TiB_2+Al_2O_3$  ceramics, Shock compression of condensed matter-2001, ed. M. D. Furnish, N. N. Thadhani, and Y. Horie, American Institute of Physics, 755-758, 2001;
15. G. Kennedy and N.N. Thadhani, Investigation of the spall strength of microstructurally-biased two-phase  $TiB_2+Al_2O_3$  ceramics, 2001 (in preparation);

## **9. PRESENTATIONS: (♦invited talk)**

1. Greg Kennedy, Micromechanical Characterization of the Fracture Resistance of A  $TiB_2/Al_2O_3$  Ceramic Composite System, 102nd Annual Meeting & Exposition of the American Ceramic Society, St. Louis, MO, April 30 - May 3, 2000;
2. Min Zhou, Effect of Microstructure on Dynamic Fracture Resistance of Ceramic Composites, The 20<sup>th</sup> Southeastern Conference on Theoretical and Applied Mechanics, April 16-18, 2000, Callaway Gardens, GA;
3. Computational Characterization of the effect of Phase Morphology and Interphase bonding on Fracture Toughness of Ceramic Composites, ASME IMECE, Orlando, FL, Nov. 2000;

4. Naresh Thadhani (♦), "Fabrication of Microstructurally-biased Two-phase  $TiB_2+Al_2O_3$  Ceramics and their Dynamic Properties," in Ninth Intl. Conf. on Processing and Fabrication of Advanced Materials, ASM Meeting, St. Louis, October 2000.
5. Naresh Thadhani; "Dynamic Mechanical Properties of Microstructurally-biased Two-phase  $TiB_2+Al_2O_3$  Ceramics," EXPLOMET 2000 Conference, Albuquerque, June 2000.
6. Naresh Thadhani "Influence Of Microstructural Bias On The Hugoniot Elastic Limit And Spall Strength Of Two-Phase  $TiB_2+Al_2O_3$  Ceramics," at the APS Topical Group Meeting in Shock-compression of Condensed Matter - 2001, June 24-29, 2001.
7. M. Zhou (♦), Microscopic and Nanoscopic Fracture in Heterogeneous in a Heterogeneous Material System, 2002 SEM Annual Conf. and Expo. on Exp. & Appl. Mechanics, June 10-12, 2002;
8. M. Zhou (♦), Computational and Experimental Characterization of Micro and Nano Scale Deformation and Fracture, NASA Langley Research Center, Hampton, August 2001
9. M. Zhou, Correlation of Dynamic Behavior with Microstructural-bias in Two-phase  $TiB_2+Al_2O_3$  Ceramics, *The Fourth International Symposium on Impact Engineering (ISIE/4)*, July 16-18, 2001, Kumamoto, Japan;
10. Numerical Simulation of Micro and Nano Scale Fracture, The 10<sup>th</sup> International Congress of Fracture, December 2-7, 2001, Honolulu, Hawaii;
11. Experimental Characterization of the Dynamic Failure Resistance of Effect  $TiB_2/Al_2O_3$  Composites, APS SCCM meeting, June 27-29, 2001, Atlanta, GA;
12. A. Keller and M. Zhou, Microscopic and Nanoscopic Fracture in Heterogeneous in a Heterogeneous Material System, 2002 SEM Annual Conf. and Expo. on Exp. & Appl. Mechanics, June 10-12, 2002;

#### **10. LIST OF PERSONNEL INVOLVED**

Faculty: Prof. Naresh N. Thadhani and Prof. Min Zhou

Grad Students: Jun (Charlie) Zhai (Ph.D./ME), Andrew Keller (M.S./ME),  
Greg Kennedy (M.S./MSE) and Louis Ferranti (M.S./MSE), Vikas Tomar (ME)

UG Students: Andy Gapin (UG/MSE), Thomas Frosell (ME), and Nicholas Liggett (ME/MSE)

Summer Undergraduate Research Assistants: Reinhard Powell (Georgia Tech, 1999), Joshua Clarke (Georgia Tech, 2000), Celeste Davis (California State University, Pomona, 2001), Adam Rowe (Colorado School of Mines, 2002)

High School Teacher Participants: Marie Johnson (Chamblee HS, Atlanta, 2000 and 2001)

#### **11. LIST OF HONORS AND AWARDS**

- Prof. Min Zhou was awarded the NSF Career Award
- Prof. Naresh Thadhani was elected FELLOW of ASM International
- Greg Kennedy, awarded ASM Atlanta Chapter outstanding graduate student award
- Greg Kennedy, International Research Fellowship Award for research at Kumamoto University in Japan.

#### **12. INTERACTION WITH ARL SCIENTISTS**

Interactions have been maintained with Ernie Chin, Jim McCauley, Datta Dandekar, Jane Adams, and Gary Guildy at ARL. Through the financial support provided by ARL, Greg Kennedy was able to spend two 2-month internships at ARL. Greg worked on microstructural characterization of samples hot-pressed at ARL.

## REFERENCES

1. D.J. Viechnicki, M.L. Slavin, and M.I. Kliman, *Ceram. Bull.*, **70** (1991), p. 1035.
2. D.A. Shockley, A.H. Marchand, S.R. Skaggs, G.E. Cort, M.W. Burkett, and R. Parker, *Int. J. of Impact Eng.*, Vol. 9(3), (1990) p. 263.
3. D.E. Grady, "Dynamic Material Properties of Armor Ceramics," Sandia National Laboratories Reports, SAND91-0147 (March 1991).
4. D.E. Grady and J.L. Wise, Sandia National Laboratories Reports, SAND93-0610 (Sept '93).
5. D.P. Dandekar and D.C. Benfanti, *J. Appl. Phys.*, **73**, (1993) pp. 673-679.
6. D.E. Grady, Sandia National Laboratories Reports, SAND94-3266 (February 1995).
7. D.L. Orphal, R.R. Franzen, A.C. Charters, T.L. Menna, and A.J. Piekutowski, *Int. J. Impact Eng.*, Vol. 19 (1997) p. 15.
8. R. Feng, Y.M. Gupta, and M.K. Wong, *J. Appl. Phys.*, **82** (1997) pp. 2845-2854.
9. J. Lankford, W.W. Predebon, J.M. Staehler, G. Subhash, B.J. Plekta, and C.E. Anderson, *Mech. Matls.*, **29** (1998) p. 205.
10. G.R. Johnson and T.J. Holmquist, *J. Appl. Phys.*, **85**(12) (1999) p. 8060.
11. D.P. Dandekar and P.I. Bartkowski, "Spall Strength of Silicon Carbides Under Shock Loading," in *Fundamental Issues and Applications of Shock Wave and High Strain rate Phenomena*, eds. K.P. Staudhammer, L.E. Murr, and M.A. Meyers, Elsevier, (2001), 71-77.
12. G.E. Hauer, P.H. Netherwood, R.F. Blenck, and L.K. Kecske, *19<sup>th</sup> Army Science Conference*, Florida, June 20-24, 1994.
13. H.D. Espinosa, N.S. Brar, G. Yuan, Y. Xu, and V. Arrietta, *Int. J. Solids Structures*, **37** [36], (2000), p. 4893.
14. F.I. Grace, "Interface Defeat of impacting rods against ceramic targets," in *Fundamental Issues and Applications of Shock Wave and High Strain rate Phenomena*, eds. K.P. Staudhammer, L.E. Murr, and M.A. Meyers, Elsevier Science, (2001), pp. 421-428.
15. J.C. LaSalvia, E.J. Horwarth, E. Rapacki, C. James Shih, and M.A. Meyers, "Microstructural and micromechanical aspects of ceramic/long-rod projectile interactions: dwell/penetration transitions," in *Fundamental Issues and Applications of Shock Wave and High Strain rate Phenomena*, eds. K.P. Staudhammer, et al., Elsevier, (2001), 437-446.
16. P. Lundberg, R. Renstrom, and B. Lundberg, *Int. J. Impact Eng.*, **24** (2000) 259.
17. H. Horii and S. Nemat-Nasser, *Phil. Trans. R. Soc. London, A*, **319** (1986), 337.
18. D.E. Grady, *Mechanics of Materials*, Vol. 29, (1998) pp. 181-203.
19. S. Sundaram and R.J. Clifton, *Mechanics of Materials*, Vol. 29, (1997), pp. 233-251.

20. J.N. Johnson, R.S. Hixon, and G.T. Gray, *J. Appl. Phys.*, 76 (10) (1994) 5706-5718.
21. K.V. Logan, Ph.D. dissertation, Georgia Institute of Technology, 1993.
22. A. Keller, "An Experimental Analysis of the Dynamic Failure Resistance of  $TiB_2/Al_2O_3$  Composites," Georgia Tech M.S. Thesis, October 2000.
23. Andrew Keller, Greg Kennedy, Louis Ferranti, Min Zhou, and Naresh Thadhani, "Correlation of Dynamic Behavior With Microstructural-Bias In Two-Phase  $TiB_2+Al_2O_3$  Ceramics," to be published in Proc. of Fourth International Symposium on Impact Engineering, Kumamoto, Japan, July 2001.
24. G. Gilde, J.W. Adams, M. Burkins, M. Motyka, P.J. Patel, E. Chin M. Sutaria, M. Rigali, and L. Prokurat Franks, "Processing of Aluminum oxide and Titanium Diboride Composites for Penetration Resistance," in Proceedings of the 25th Annual Cocoa Beach Conference of The American Ceramic Society, January 23-28, 2001.
25. J. Zhai and M. Zhou, "Finite Element Analysis of Micromechanical Failure Modes in Heterogeneous Brittle Solids", *International Journal of Fracture*, special issue on *Failure Mode Transition in Solids*, R. C. Batra, Y. D. S. Rajapakse, and A. J. Rosakis, eds., 101, pp. 161-180, 2000.
26. M. Zhou and J. Zhai, Micromechanical Characterization of the Fracture Resistance of A  $TiB_2/Al_2O_3$  Ceramic Composite System, American Ceramic Society 102nd Annual Meeting & Exposition, St. Louis, Missouri, April 30 - May 3, 2000.
27. K.V. Logan, "Shaped Refractory Products and the Method of Making the Same," U.S. Patent, # 5,141,900, August 25, 1992
28. E.E. Underwood, *Quantitative Stereology*, Addison Wesley Publishing Company, 1970.
29. G. Kennedy, J. Zhai, R. Russel, M. Zhou, and N.N. Thadhani, "Dynamic High Strain Rate Mechanical Behavior of Microstructurally-Biased Two-phase  $TiB_2+Al_2O_3$  Ceramic," 24<sup>th</sup> Annual Int. Conf. On Advanced Ceramics and Composites, Cocoa Beach, Jan 23-28, 2001.

## APPENDIX

### RE- and PRE-PRINTS of PAPERS PUBLISHED

Based on  
ARO-SUPPORTED RESEARCH

Processing and Characterization of Microstructually Biased Two-Phase  
Titanium Diboride/Alumina Ceramic ( $TiB_2 + Al_2O_3$ )

A Thesis  
Presented to  
the Academic Faculty

by

Louis Ferranti Jr.

In Partial Fulfillment  
of the Requirements for the Degree  
Master of Science in Materials Science and Engineering

Georgia Institute of Technology  
October 2001

## SUMMARY

The development of microstructurally biased two-phase titanium diboride/alumina ( $TiB_2 + Al_2O_3$ ) ceramic is influenced by several factors during processing. A standard method for quantitatively characterizing the different types of microstructures produced is necessary to comprehend the mechanism(s) that control the microstructural bias (e.g. phase distribution and morphology) generated during processing, and their subsequent effect on mechanical properties. In this study, two-phased  $TiB_2 + Al_2O_3$  ceramic powders were fabricated using self-propagating high temperature synthesis (SHS) reactions, and by manually mixing (MM) commercially purchased pure  $TiB_2$  and  $Al_2O_3$  powders. Dense ceramic disks were formed by hot-pressing MM and SHS formed powders after various ball-milling times. The microstructures developed as a function of powder processing technique (SHS reaction or MM), ball-milling time, and varying hot-pressing parameters including varying degrees of connectivity of the  $TiB_2$  minor phase surrounding  $Al_2O_3$  and different phase sizes and size distributions. These features were characterized by stereological measurements of two-dimensional cross-sections of the samples, based on phase size and morphology in terms of phase connectivity and dispersion of the minor phase ( $TiB_2$ ). Mean integral curvature was used to quantitatively describe the connectivity of the  $TiB_2$  phase around an  $Al_2O_3$  matrix. It was observed that the  $TiB_2$  phase connectivity is established directly during the SHS synthesis process, and extended periods of ball-milling only reduce the inherent connectivity while decreasing the phase size and altering the phase distribution. Thus, an optimal ball-milling time of about 4 hours for the SHS synthesized powders and lesser for the manually mixed

powders was needed to achieve the maximum degree of  $TiB_2$  phase connectivity and phase/particle size distribution for maximum final densification during hot-pressing. Microhardness and fracture toughness measurements performed on the dense compacts showed that the presence of  $TiB_2$  dramatically improves the fracture toughness of the two-phase ceramic in contrast to monolithic alumina.

**MICROMECHANICAL MODELING OF DYNAMIC FRACTURE  
IN CERAMIC COMPOSITES**

A Thesis  
Presented to  
The Academic Faculty

By

Jun Zhai

In Partial Fulfillment  
Of the Requirement for the Degree  
Doctor of Philosophy in Mechanical Engineering

Georgia Institute of Technology

January, 2000

## Summary

Recently, alumina/titanium diboride ( $\text{Al}_2\text{O}_3/\text{TiB}_2$ ) two phase ceramic composites having a wide range of micro and nano phase sizes and phase morphologies have been developed. variations in processing conditions have allowed formation of these ceramics with biased microstructures which are expected to influence the dynamic failure behavior. In order to understand failure mechanisms in this material system and the influence of phase morphologies and phase size on fracture resistance, a numerical framework is needed to explicitly account for arbitrary microstructures and fracture patterns.

Micromechanical modeling and simulation provide an important approach for analyzing the effects of material inhomogeneity and anisotropy over a range of microscopic length scales. A framework is proposed in this research for explicit modeling and simulation of microscopic damage/fracture/failure processes. The model and approach account for the real arbitrary microstructural morphologies. A cohesive finite element method (CFEM) based on cohesive surface theory is used. A fully dynamic kinetic framework and finite deformation kinematic formulation are used. Mesh independence of solution is studied and verified.

Idealized microstructures containing circular and elliptical particles and real microstructures with arbitrary morphologies are used to investigate the effects of phase morphologies, phase size and phase anisotropy on fracture of this ceramic composite system. Numerical results show that microstructural variations give rise to a range of fracture resistance. It is found that small inter-phase spacing, small phase size, uniform distribution of reinforcements and microstructures with enhanced bridging effects will contribute to increasing fracture resistance of materials.

The failure mode is found to be significantly influenced by the interfacial bonding strength between the phases. Two distinct failure modes are observed for strong and weak bonding. While the primary failure mode is the main crack propagation and branching in microstructures with strong interfaces, the primary failure mode is microcrack nucleation and coalescence in microstructures with weak interfaces.

The loading rate effects are also investigated. It is found that energy release rate increases with loading rates, due to the extensive damage development at higher loading rates.

This research contributes to the elucidation of microscopic deformation and failure mechanisms of microscopically inhomogeneous materials over a range of size scales. The research is important for the development of more failure resistant ceramic composites through microstructural design and revision.

An Experimental Analysis of the Dynamic Failure Resistance of  
 $TiB_2/Al_2O_3$  Composites

A Thesis Presented to the Academic Faculty

By Andrew R. Keller

In Partial Fulfillment  
of the Requirements for the Degree  
Master of Science in Mechanical Engineering

Georgia Institute of Technology

October 2000

under quasi-static conditions. Clearly, there is a strong dependence of failure stress on the strain rate. The strength at higher rates is approximately 27% greater than that observed at quasi-static loading rates.

The use of a soft recovery mechanism in the experiment allowed the specimen fragments to be recovered for postmortem analysis. Scanning electron microscopy (SEM) and Energy Dispersive Spectrometry (EDS) were used to analyze the post mortem fracture surfaces. Inspection of the fracture surfaces indicated that failure associated with the  $\text{Al}_2\text{O}_3$  phase of the composite is characterized by transgranular cleavage in all four materials. Depending upon the microstructure, failure associated with the  $\text{TiB}_2$  phase was characterized by a combination of transgranular cleavage and intergranular pull out.

In addition to the SEM analysis of the post mortem fragments, a quantification of the fragment size distribution was conducted for each of the four materials. Materials with larger grain sizes and higher strength tended to yield larger average fragment sizes. The distribution of the fragment sizes were compared to theoretical models suggested by Lienau (1936), Mott and Linfoot (1943), and Grady and Kipp (1985, 1990). It was found that the models of Grady and Kipp provided the best fit to the distribution of the fragments in these experiments.

# Dynamic high-strain-rate mechanical behavior of microstructurally biased two-phase $\text{TiB}_2 + \text{Al}_2\text{O}_3$ ceramics

Greg Kennedy and Louis Ferranti

*School of Materials Science and Engineering, Georgia Institute of Technology, Atlanta, Georgia 30332-0245*

Rod Russell

*Institute for Advanced Technology, University of Texas, Austin, Texas 78759*

Min Zhou

*Woodruff School of Mechanical Engineering, Georgia Institute of Technology, Atlanta, Georgia 30332-0245*

Naresh Thadhani<sup>a)</sup>

*School of Materials Science and Engineering, Georgia Institute of Technology, Atlanta, Georgia 30332-0245*

(Received 10 June 2001; accepted for publication 1 November 2001)

The dynamic high-strain-rate behavior of two-phase  $\text{TiB}_2 + \text{Al}_2\text{O}_3$  ceramics with biased microstructures was investigated in this study. The microstructural bias includes differences in phase (grain) size and phase distribution such that in one case a continuous (interconnected)  $\text{TiB}_2$  network surrounds the  $\text{Al}_2\text{O}_3$  phase (qualitatively termed “T@A”) and in another case the  $\text{TiB}_2$  and  $\text{Al}_2\text{O}_3$  phases are interdispersed and uniformly intertwined with each other (qualitatively termed “TinA”). Quantitative microscopy was used to characterize the phase size and the integral curvature which is taken as a measure of  $\text{TiB}_2$  phase connectivity around  $\text{Al}_2\text{O}_3$ . Dynamic compression and tension (spall) properties were measured using plate impact experiments. The measurements used piezoelectric polyvinylidene fluoride stress gauges to obtain the loading profile and to determine the Hugoniot elastic limit. In addition, velocity interferometry system for any reflector interferometry was used to obtain the spall signal and the tensile dynamic strengths of the materials. Experimental results reveal that while the  $\sigma_{\text{HEL}}$  and the compressive strengths of  $\text{TiB}_2 + \text{Al}_2\text{O}_3$  ceramics are dependent on the average grain (phase) size, the tensile (spall) strength scales with the  $\text{TiB}_2$ -phase connectivity. This result suggests that the interconnected  $\text{TiB}_2/\text{Al}_2\text{O}_3$  microstructural morphology provides a stronger impediment to failure in tension compared with the morphology with simply interdispersed phases. © 2002 American Institute of Physics. [DOI: 10.1063/1.1429770]

## I. INTRODUCTION

The dynamic, high-strain-rate deformation behavior of materials (and consequently their ballistic performance) is dramatically influenced by their microstructural characteristics, including phase size, phase morphology, composition and texture. Such a trend has been revealed not only for steels used as heavy armor, but also for ceramics considered for lightweight armor applications.<sup>1</sup> In addition to their low density, ceramics exhibit superior hardness and high compressive strength that enables erosion and “interface defeat” of projectiles. This mechanism makes ceramics highly desirable for use as armor materials. Over the last 30 years a number of studies on ballistic performance and dynamic behavior<sup>1–19</sup> have been performed on various ceramics (e.g.,  $\text{AlN}$ ,  $\text{Al}_2\text{O}_3$ ,  $\text{B}_4\text{C}$ ,  $\text{SiC}$ ,  $\text{TiB}_2$ ,  $\text{WC}$ ,  $\text{ZrO}_2$ ). These studies have suggested that the desirable characteristics of ceramics that are beneficial for the defeat of projectiles include the combination of high yield strength or hardness, high tensile spall strength, high fracture toughness, high Poisson’s ratio, and high coefficient of friction.<sup>15</sup> The properties typically measured to characterize the dynamic behavior of ceramics are the Hugoniot elastic limit ( $\sigma_{\text{HEL}}$ ) and spall strength. In

general, the spall strength is lower than the elastic limit. Materials such as  $\text{TiB}_2$  have a spall strength that decreases with increasing impact stress and becomes negligible at the  $\sigma_{\text{HEL}}$ . In contrast,  $\text{Al}_2\text{O}_3$  maintains its original spall strength even at impact stress levels that exceed the  $\sigma_{\text{HEL}}$ .<sup>3</sup>

It has been demonstrated that  $\text{SiC}$  and  $\text{TiB}_2$  exhibit the most desirable ballistic properties based on results of experiments performed to determine the transition between interface defeat and penetration involving  $\text{W}$  projectiles.<sup>14–16</sup> The impact velocity for dwell/penetration transition for  $\text{SiC}$  and  $\text{TiB}_2$  is higher than that for  $\text{B}_4\text{C}$ , in spite of the higher yield strength of the latter. This trend is consistent with the predictions from the dwell/penetration transition model<sup>17</sup> which accounts for damage mechanism based on the extension of mode-I wing cracks. The predictions illustrate that  $\text{SiC}$  and  $\text{TiB}_2$  ceramics have the ability to suppress the formation of wing cracks due to plastic relaxation of preexisting flaws, while  $\text{B}_4\text{C}$  shows a brittle behavior dominated by growth of wing cracks. Brittle fracture is also expected to dominate the behavior of  $\text{Al}_2\text{O}_3$ . Measurements of shock wave profiles have also illustrated the ability of  $\text{SiC}$  and  $\text{TiB}_2$  ceramics to undergo deformation-induced hardening,<sup>18</sup> which may give rise to improved ballistic properties.

Most dynamic behavior studies performed to date have focused on single-phase monolithic ceramics, although ce-

<sup>a)</sup>Electronic mail: naresh.thadhani@mse.gatech.edu

ramics with glassy (impurity) phases, e.g., AD85  $\text{Al}_2\text{O}_3$ , have also been investigated. In such ceramics, the presence of intergranular oxide glass has been shown to significantly lower the tensile (spall) strength, and, therefore, the fracture resistance.<sup>19</sup> Dynamic behavior of ductile metal-matrix composites, e.g., Al alloys consisting of embedded ceramic particles, has been studied to a limited extent.<sup>20</sup> It has been shown that both the dynamic yield strength and the spall strength are reduced, in comparison to strength increases observed in particle-reinforced composite materials under quasi-static loading conditions. The composite structure acts as a mechanical energy trap due to scattering of waves from incoherent boundaries and interfaces between the matrix and reinforcement phases having dissimilar shock impedance. The high-strain-rate mechanical behavior of ceramic-ceramic composites shows a strain rate dependence significantly different from that observed in metal-matrix composites. Dynamic behavior of ceramic composites has been limited only to the study of two-phase  $\text{Al}_2\text{O}_3 + \text{TiB}_2$  ceramics (70/30 mass ratio). Past work on these two-phase ceramics has revealed an 80% increase in compressive strength with increasing strain rate (3.5 GPa at  $10^{-4} \text{ s}^{-1}$ –5.8 GPa at  $10^3 \text{ s}^{-1}$ ) as shown in Fig. 1(a).<sup>21</sup> In addition, as illustrated in Fig. 1(b), the two-phase  $\text{Al}_2\text{O}_3 + \text{TiB}_2$  ceramics have static and dynamic mechanical properties superior to their monolithic constituents.<sup>21–23</sup> The  $\text{Al}_2\text{O}_3 + \text{TiB}_2$  ceramics have also shown better penetration resistance than monolithic  $\text{Al}_2\text{O}_3$ , and the system in which  $\text{TiB}_2$  is an interconnected phase surrounding  $\text{Al}_2\text{O}_3$  has been shown to exhibit a superior ballistic performance compared with the system in which the two phases are simply uniformly interdispersed.<sup>21,24</sup> Micro-mechanical simulations have also demonstrated the effect of microstructural bias on failure resistance.<sup>25,26</sup> However, the influence of microstructural bias on the fundamental dynamic properties of these ceramics has not been fully established.

The objective of the present work is to characterize the high-strain-rate deformation and damage response of four types of microstructurally biased, two-phase  $\text{TiB}_2 + \text{Al}_2\text{O}_3$  ceramics. The microstructural bias of the four ceramics falls into two morphological categories. The first category involves a continuous (interconnected)  $\text{TiB}_2$  network that surrounds  $\text{Al}_2\text{O}_3$  (qualitatively termed “T@A”) and the second category involves  $\text{TiB}_2$  and  $\text{Al}_2\text{O}_3$  phases that are interdispersed and uniformly intertwined with each other (qualitatively termed “TinA”).<sup>21</sup> Normal plate impact experiments were used to measure the  $\sigma_{\text{HEL}}$  and the spall strength of the materials. The measured responses were then correlated with the microstructure morphological characteristics and the phase size scales.

## II. PREPARATION AND CHARACTERIZATION OF THE TWO-PHASE CERAMICS

The two-phase  $\text{TiB}_2 + \text{Al}_2\text{O}_3$  ceramics were fabricated as  $\sim 80$  mm diameter by 20-mm-thick disks by hot-pressing powders. The powders were produced through either self-propagating high-temperature synthesis (SHS) reactions between powder precursors ( $3\text{TiO}_2 + 3\text{B}_2\text{O}_3 + 10\text{Al} = 3\text{TiB}_2 + \text{Al}_2\text{O}_3$ ; 33:67 weight ratio), or through manual mixing (MM) of the constituents (nominally, 30 wt%  $\text{TiB}_2$  + 70 wt%  $\text{Al}_2\text{O}_3$ ) which are obtained using conventional powder processing techniques. Following the SHS synthesis or manual mixing, the powders were also ball milled to generate the microstructural bias. Details of the processing approaches used for fabricating these two-phase  $\text{TiB}_2 + \text{Al}_2\text{O}_3$  ceramics are described elsewhere.<sup>21,27</sup>

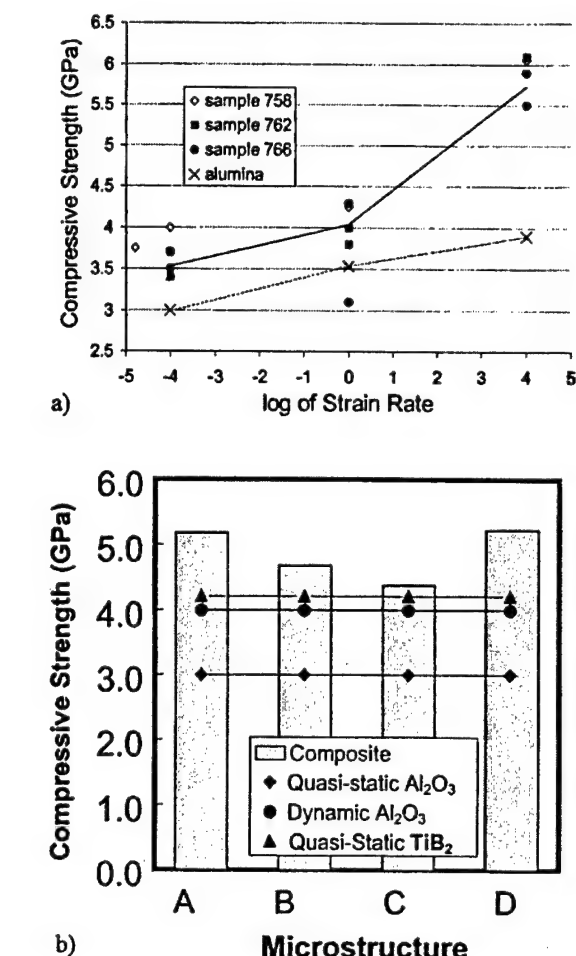


FIG. 1. (a) Strain-rate dependence of compressive strength for  $\text{Al}_2\text{O}_3 + \text{TiB}_2$  (solid line) in contrast to that for  $\text{Al}_2\text{O}_3$  (dashed line) (see Ref. 23). (b) A comparison of the dynamic compressive strengths of two-phase  $\text{TiB}_2 + \text{Al}_2\text{O}_3$  with those of the monolithic constituents (see Ref. 23).

+  $\text{Al}_2\text{O}_3$ ; 33:67 weight ratio), or through manual mixing (MM) of the constituents (nominally, 30 wt%  $\text{TiB}_2$  + 70 wt%  $\text{Al}_2\text{O}_3$ ) which are obtained using conventional powder processing techniques. Following the SHS synthesis or manual mixing, the powders were also ball milled to generate the microstructural bias. Details of the processing approaches used for fabricating these two-phase  $\text{TiB}_2 + \text{Al}_2\text{O}_3$  ceramics are described elsewhere.<sup>21,27</sup>

Quantitative metallography<sup>28</sup> was performed to determine the phase size (as measured by the linear intercept length) and phase connectivity (based on measurement of integral curvature). The connectivity of a phase in a multi-phase material can be related to a quantitative measurement of curvature,  $k$ , defined as the angle,  $d\theta$ , of a finite segment of an arc divided by the length of the arc  $d\lambda$ , or

$$k = d\theta/d\lambda. \quad (1)$$

Through a division of line integrals, the average curvature,  $k_{\text{ave}}$  can be calculated by dividing the angle of arc  $\theta_A^{\text{net}}$  (in phase A) by total length of arc,  $L_A$ . Hence,

$$k_{\text{ave}} = \theta_A^{\text{net}}/L_A = \{\theta_A^+ - \theta_A^-\}/L_A, \quad (2)$$

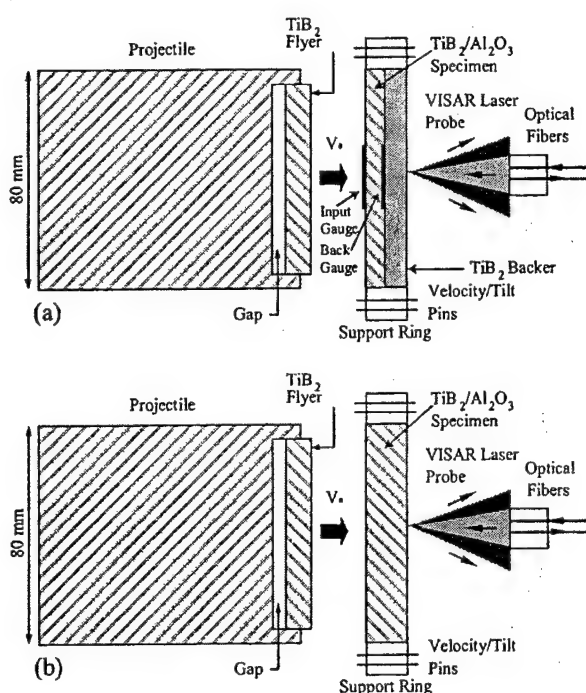


FIG. 2. Schematic illustrations of the setups used for measurements of (a) stress profiles with PVDF gauges and (b) free-surface velocity traces with VISAR interferometry.

where,  $\theta_A^+$  is angle for a convex arc and  $\theta_A^-$  is angle for a concave arc in phase A. If the phases are considered as closed (as in the case of our two-phase ceramic), then the angle of the arc is  $2\pi$ . Hence the above equation can be written as

$$k_{\text{ave}} = (2\pi)N_A^{\text{net}}/L_A = 2\pi\{N_A^+ - N_A^-\}/L_A, \quad (3)$$

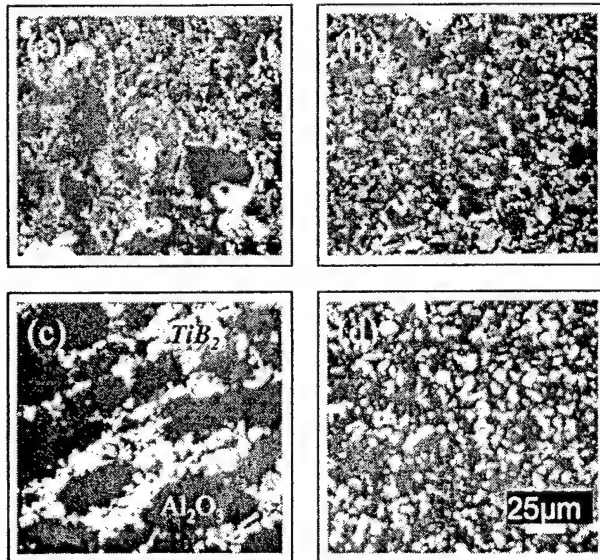


FIG. 3. Optical micrographs of two-phase ceramics (TiB<sub>2</sub> white and Al<sub>2</sub>O<sub>3</sub> dark phase). (a) Sample A, SHS, T@A microstructure, (b) sample B, SHS, TinA microstructure, (c) sample C, MM, T@A microstructure, and (d) sample D, MM, TinA microstructure.

TABLE I. Measured average values of integral curvature, and sizes of constituent phases.

Microstructure type	Average integral curvature ( $\mu\text{m}^{-1}$ )	TiB <sub>2</sub> phase size ( $\mu\text{m}$ )	Al <sub>2</sub> O <sub>3</sub> phase size ( $\mu\text{m}$ )
A	$-0.316 \pm 0.022$	7.0	10.4
B	$-0.476 \pm 0.046$	6.2	9.1
C	$-0.074 \pm 0.028$	8.7	25.1
D	$-0.375 \pm 0.031$	7.9	12.3

where,  $N_A^{\text{net}}$ ,  $N_A^+$ , and  $N_A^-$  are the net, positive, and negative numbers of loops of phase A. The length of the arc,  $L_A$ , of a closed loop is the perimeter and can be related to the mean linear intercept length  $L$  using  $L_A = (\pi/2)(1/L)$ . The average integral curvature of phase A can then be expressed as

$$k_{\text{ave}} = 4N_A^{\text{net}}L. \quad (4)$$

In the present work, the average integral curvature values were determined using Eq. (4). The mean linear intercept length  $L$  and the number of net loops of "A" (or TiB<sub>2</sub>) phase around the "B" (or Al<sub>2</sub>O<sub>3</sub>) phase were determined using IMAGEPRO-PLUS, a commercial software package (product of Media Cybernetics). To account for anisotropy effects, the analysis was performed on at least ten micrographs of both planar and cross-sectional surfaces. However, the differences due to anisotropy were found to be in the range of the standard deviation.<sup>29</sup>

The impact experiments used an 80-mm-diam, single-stage gas gun. Measurements of the  $\sigma_{\text{HEL}}$  and the shock wave speeds under dynamic compression were obtained from stress profiles recorded using polyvinylidene fluoride (PVDF) stress gauges. As shown in Fig. 2(a), a TiB<sub>2</sub> flyer plate backed by an air gap and mounted at the head of an aluminum projectile, was used to impact the target assembly consisting of ~3-mm-thick ceramic sample backed by a TiB<sub>2</sub> backer plate. Impact experiments were conducted at a nominal velocity of ~0.750 km/s (~15 GPa nominal impact stress) to ensure shock loading of samples under similar conditions. The impact velocity was measured using arrival time pins. One PVDF gauge package was placed at the impact surface and another was placed between the sample and TiB<sub>2</sub>

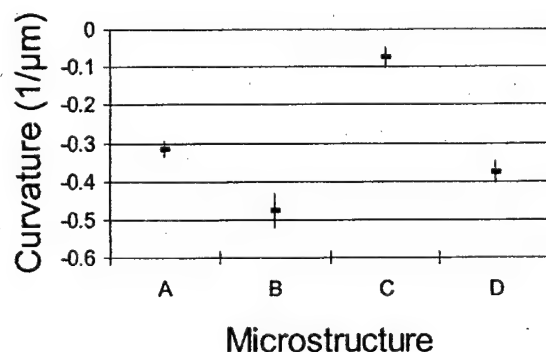


FIG. 4. Plot comparing the average integral curvature values of the TiB<sub>2</sub> + Al<sub>2</sub>O<sub>3</sub> ceramic samples of four different types of microstructures. Note that the TiB<sub>2</sub> phase connectivity is greater in sample A than in sample B, and likewise in sample C than in sample D.

TABLE II. Measured values of density, elastic wave velocity, and Young's and shear moduli of the four types of microstructurally biased ceramic samples.

Sample type	Density (g/cm <sup>3</sup> ; %TD)	Long. vcl (km/s)	Shear vcl. (km/s)	Young's mod (GPa)	Shear mod (GPa)
A	4.095; 99.4%	11.114	6.477	505.8	171.8
B	3.939; 95.6%	10.336	6.145	420.8	148.7
C	4.108; 99.7%	10.796	6.527	478.8	175.0
D	4.083; 99.1%	10.773	6.523	473.9	173.7
TiB <sub>2</sub> <sup>a</sup>	4.509	10.790	7.43	524.9	248.9
Al <sub>2</sub> O <sub>3</sub> <sup>a</sup>	3.55	9.280	5.47	306.2	106.4

<sup>a</sup>Values of TiB<sub>2</sub> and Al<sub>2</sub>O<sub>3</sub> are from D. E. Grady, Sandia Report No. SAND-91-014, UC-704, 1991.

backer plate. The experimental setup was designed such that a planar-parallel shock wave propagates through the target and the input and propagated stress profiles are measured with little interference from radial reflected waves. The PVDF gauges were connected to current viewing resistors to allow current versus time data acquisition with a 1 GHz frequency oscilloscope. The current versus time data were then numerically integrated to yield stress versus time profiles for the impact and propagated wave gauges. The arrival time at the respective gauges was taken as the travel time through the sample thickness, from which the shock wave speed was determined.

Figure 2(b) shows the experimental setup, illustrating the target sample (without any backer) being impacted by a projectile consisting of a 4140 steel (or silicon carbide) flyer plate and an aluminum sabot. An air gap exists between the flyer plate and the sabot to allow full unloading required for the spall strength measurements. All sample surfaces were lapped for flatness and parallelism. The ceramic targets were polished with 5  $\mu\text{m}$  diamond paste to ensure reflectivity required by the velocity interferometer system for any reflector (VISAR) beam. The time-resolved longitudinal motion of the sample free surface was measured in the form of interference fringes with a Valyn VISAR and recorded on a digital oscilloscope. The interference fringes were then converted to time-resolved history of particle velocity.

### III. RESULTS AND DISCUSSIONS

#### A. Microstructural characterization

Optical micrographs of the four types of microstructurally biased samples studied are shown in Figs. 3(a)–3(d). The micrographs correspond to sample A made by the SHS process with TiB<sub>2</sub> surrounding Al<sub>2</sub>O<sub>3</sub> (T@A); sample B also made by SHS with intermixed TiB<sub>2</sub> and Al<sub>2</sub>O<sub>3</sub> (TinA) phases; sample C made by MM with TiB<sub>2</sub> surrounding Al<sub>2</sub>O<sub>3</sub> (T@A); and sample D made by MM with intermixed TiB<sub>2</sub> and Al<sub>2</sub>O<sub>3</sub> (TinA) phases. It should be noted that the samples do not reveal 100% microstructural bias, i.e., while the micrographs of samples A and C generally illustrate a nearly continuous (interconnected) TiB<sub>2</sub> phase surrounding Al<sub>2</sub>O<sub>3</sub>, regions where the converse is true are also present. Likewise, samples B and D show not only an intermixed structure but also the continuous phase microstructures.

Table I lists the values of average integral curvature and the average size of TiB<sub>2</sub> and Al<sub>2</sub>O<sub>3</sub> phases. In general, the

average sizes of TiB<sub>2</sub> and Al<sub>2</sub>O<sub>3</sub> phases in both SHS samples (A and B) are smaller than those in the manually mixed samples (C and D), with sample C showing the largest size for both constituents. Sample C also represents the microstructure with the highest value of connectivity for TiB<sub>2</sub>, as illustrated in Fig. 4. All samples, in fact, show a negative curvature, since, within a given area of measurement, the number of loops around smaller particles is greater than that surrounding the larger particles. This skews the average integral curvature towards negative values. Nevertheless, the measured values provide a quantitative measure of the microstructural bias on the basis of phase connectivity, and illustrate that the connectivity of TiB<sub>2</sub> phase is greater in sample A than in sample B, and likewise in sample C than in sample D. The grain size of the respective phases also shows a similar trend, with sample A being coarser than sample B, and sample C being coarser than sample D.

#### B. Characterization of elastic properties

The elastic properties of the ceramics were characterized using an Ultran Laboratories ultrasonic test apparatus. The setup allows determination of the longitudinal and shear wave velocities from which the elastic moduli are obtained using densities measured on individual samples by the Archimedean method. Table II lists the results of elastic wave velocity measurements and corresponding Young's and shear moduli. It can be seen that the moduli of the various ceramic samples are relatively similar except in the case of sample B, which has ~4.4% porosity.

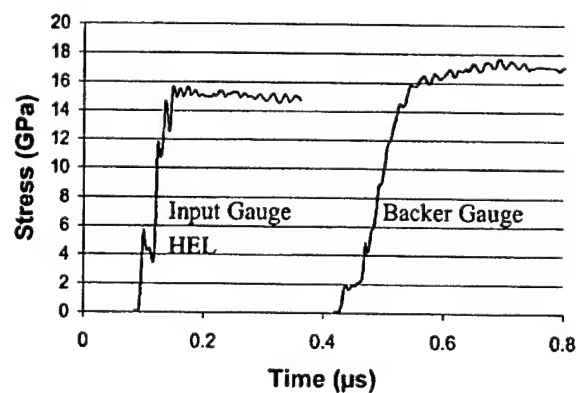


FIG. 5. Typical input and backer gauges stress profiles (sample B) obtained from Expt. 9916.

TABLE III. Summary of results of impact experiments under dynamic compression.

Sample type and expt. No.	Target thickness (mm)	Density (%TMD)	Wave speed (km/s)	Hugoniot elastic limit $\sigma_{HEL}$ (GPa)	Tensile yield str. $\sigma_{YS}$ (GPa)
A-9914	3.03	99.4%	8.24 $\pm$ .83	6.2 $\pm$ 3.1	4.2 $\pm$ 2.1
B-9916	3.42	95.6%	9.67 $\pm$ 1.0	4.4 $\pm$ 1.2	3.11 $\pm$ 0.84
C-9920	3.36	99.7%	9.08 $\pm$ .74	5.5 $\pm$ 2.3	4.02 $\pm$ 1.7
D-9921	3.06	99.1%	8.31 $\pm$ .78	8.5 $\pm$ 4.5	6.23 $\pm$ 3.3

### C. Measurements of dynamic high-strain-rate mechanical behavior

Stress wave profiles obtained using PVDF stress gauges were used to determine the mechanical behavior under dynamic compression. VISAR interferometry was used to obtain free-surface velocity profiles to determine the tensile (spall) strength.

#### 1. Dynamic compression behavior

Measurements of the Hugoniot elastic limit ( $\sigma_{HEL}$ ) were obtained from normal planar impact experiments conducted at an impact velocity of 750 m/s. Figure 5(b) shows examples of stress histories recorded by the "input" and "backer" PVDF stress gauges from experiment 9916, for the sample B ceramic. Table III lists the sample thickness, density, impact velocity measured using shorting pins, wave speed measured by considering the times of travel through the sample thickness as recorded by input and backer gauges, the  $\sigma_{HEL}$ , and the yield stress in simple tension ( $\sigma_{YS}$ ) calculated from the  $\sigma_{HEL}$ .

The wave speed in the material, which is a function of sample density and microstructure in addition to loading conditions, is measured to be similar for all four samples (within the range of experimental scatter). The Hugoniot elastic limit ( $\sigma_{HEL}$ ), the axial stress at which a solid loaded under conditions of uniaxial strain begins to exhibit plastic deformation, is observed to be a strong function of the microstructure including phase size. The  $\sigma_{HEL}$  was determined by considering one half the value between the peak and trough of the elastic precursor wave [Fig. 5(b)], and one half the difference was considered as the range. The  $\sigma_{HEL}$  is found to be the lowest for sample B ( $4.4 \pm 1.2$  GPa), due to its high level of porosity ( $\sim 4\%$ ) and highest for sample D ( $8.5 \pm 4.5$  GPa) (with a large standard deviation). The  $\sigma_{HEL}$  values reported previously by Grady<sup>4,6</sup> are 9–18 GPa for  $TiB_2$ , and  $\sim 6.7$  for  $Al_2O_3$ . While  $\sigma_{HEL}$  identifies the limit of elastic response under dynamic (shock) uniaxial strain loading, it is also common to assume a Von Misses-type yield condition which asserts that plastic flow initiates when the second deviatoric stress invariant attains a critical value. Through this formalism, the yield stress in simple tension has been shown to be related to ( $\sigma_{HEL}$ ) through  $\sigma_{YS} = 2(C_s^2/C_L^2) \times (\sigma_{HEL})$ .<sup>6</sup> The yield stress in simple tension,  $\sigma_{YS}$  for the various microstructurally biased samples follows the same trend as the Hugoniot elastic limit, with sample D showing the highest and sample B the lowest yield strength.

#### 2. Tensile (spall) strength

Spall experiments were performed (with VISAR interferometry) on samples of microstructure A at impact velocities corresponding to input stresses above and below the  $\sigma_{HEL}$ , and on samples of microstructures 'C' and 'D' under elastic loading conditions to ensure that the compression-induced damage does not influence the tensile response. Figure 6 shows the free-surface velocity traces obtained on samples of microstructure A at 237, 495, and 758 m/s, using a 2.66-mm-thick AISI 4140 steel flyer plate. Arrows indicate spall signal.

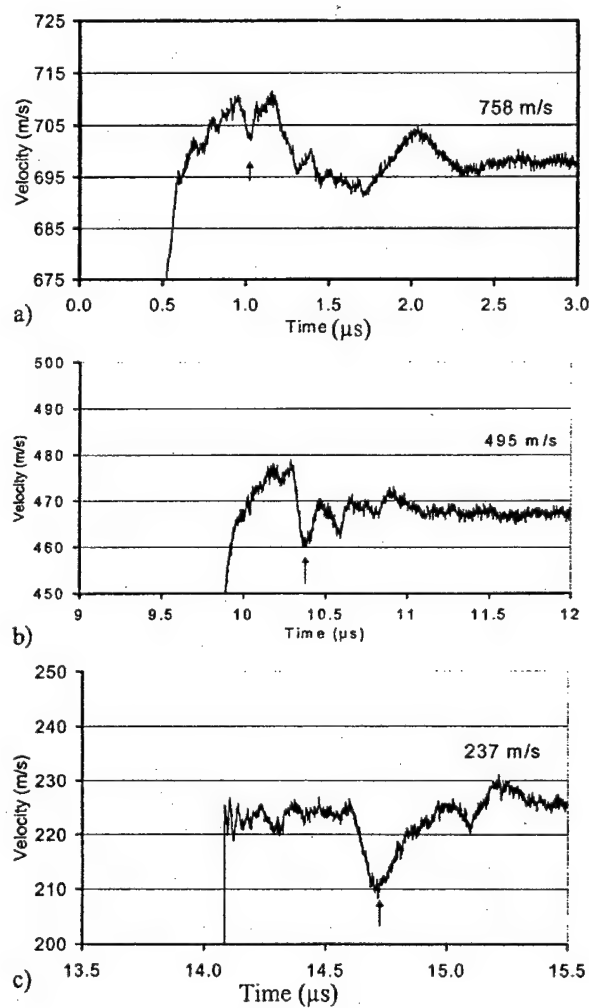


FIG. 6. Free-surface velocity traces obtained on samples of Microstructure A at 237(a), 495(b), and 758(c) m/s, using a 2.66-mm-thick AISI 4140 steel flyer plate. Arrows indicate spall signal.

TABLE IV. Loading conditions and summary of results of spall experiments.

Sample type and expt. No.	Flyer plate material	Flyer & target th. (mm)	Target density (%TMD)	Impact velocity (m/s)	Input stress (GPa)	Spall strength (GPa)
A-0005	4140 steel	2.66/16.22	98.8%	495	7.9	0.320
A-0007	4140 steel	2.66/16.20	98.8%	237	3.7	0.320
A-0008	4140 steel	2.66/7.99	98.8%	758	11.8	0.160
C-9925	SiC	4.30/7.54	99.7%	244	3.8	0.311
D-9926	SiC	4.77/7.10	99.1%	239	3.8	0.222

thick AISI 4140 steel flyer plate. The velocity traces reveal a spall signal (velocity decrease,  $\Delta U_{fs}$ ) which was used to compute the spall strength ( $\sigma_{spall} = 1/2\rho_0 C_0 \Delta U_{fs}$ ). As shown in Table IV, the spall strength for sample A is 0.320 MPa at input stresses of 3.7 and 7.9 GPa. However, with input stress increasing to 11.8 GPa, the spall strength decreases to 0.160 GPa. It can be seen that while the spall strength decreases with increasing input stress, the two-phase  $TiB_2 + Al_2O_3$  ceramic maintains non-negligible spall strength even at input stresses exceeding the Hugoniot elastic limit ( $6.2 \pm 3.4$  GPa).

Tensile spall experiments were also performed on samples of microstructures C and D, at an input stress of  $\sim 3.8$  GPa. Figure 7 shows the free velocity traces for these samples. A spall strength of 0.311 GPa for sample C and 0.222 GPa for sample D was observed. A comparison of spall test results between sample C and sample D shows that the latter sample with dispersed microstructure has a lower spall strength, while the microstructure with interconnected  $TiB_2$  has a higher spall strength, even though sample D has a smaller phase size. The measured high value of spall strength of the two-phase ceramic is similar to the published spall strength of  $TiB_2$  (0.33 GPa) but lower than that of  $Al_2O_3$  (0.45 GPa).

#### IV. DISCUSSION AND SUMMARY OF RESULTS

The two-phase  $TiB_2 + Al_2O_3$  ceramics, made either by the SHS or mechanical milling methods, reveal differences in microstructure which qualitatively show  $TiB_2$  as a continuous (interconnected) phase surrounding  $Al_2O_3$  (T@A), or  $TiB_2$  and  $Al_2O_3$  intermixed with each other (TinA). Quan-

titative microscopy analysis based on the measurement of the integral curvature showed that the samples investigated do not exhibit 100% microstructural bias. However, the overall trend of the influence of microstructural bias emerging from the results of experiments performed to date illustrates that the dynamic yield strength and the  $\sigma_{HEL}$  are more dominantly dependent on the phase size. Sample C prepared by manual mixing and having the largest phase (grain) size shows the lowest values in contrast to the other samples of similar ( $\sim 99\%$ ) density. In contrast, the tensile spall strength appears to scale with the continuity of the  $TiB_2$  phase. Sample C, which has the most interconnected  $TiB_2$  phase, has the highest value of the tensile spall strength.

The results therefore, illustrate that while the Hugoniot elastic limit and the dynamic compressive yield strength of  $Al_2O_3 + TiB_2$  are dependent on the average grain (phase) size, the tensile spall strength scales with the  $TiB_2$ -phase connectivity, and less so with the average phase size. It is possible that the interconnected phase morphology is more effective in impeding initiation and progression of fracture under tensile conditions. If so,  $TiB_2$  as an interconnected phase has the ability to suppress and relax the cracks formed in  $Al_2O_3$ . Alternatively, it is also possible that in the two-phase ceramic with the microstructure containing dispersed  $Al_2O_3$  and  $TiB_2$  phases, the mechanical energy trapping due to scattering of waves from incoherent boundaries and interfaces results in the lowering of the tensile (spall) strength. Further work is currently in progress to more clearly delineate the effects of interconnected versus dispersed  $TiB_2$  phase, and to eventually fabricate two-phase  $Al_2O_3 + TiB_2$  ceramics with the microstructural bias that yields the most optimal dynamic properties.

#### ACKNOWLEDGMENTS

Funding for this research was provided by the U.S. Army Research Office, under Grant No. DAAG55-98-1-0454 (Dr. David Stepp program monitor). The authors thank Dr. K. V. Logan for providing the samples being investigated in the present work, and also appreciate her valuable discussions and comments.

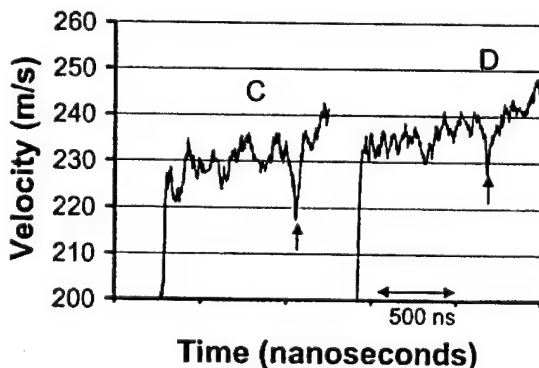


FIG. 7. Free-surface velocity traces obtained for samples C and D, at similar loading conditions.

<sup>1</sup>D. J. Viechnicki, M. L. Slavin, and M. I. Kliman, *Ceram. Bull.* **70**, 1035 (1991).

<sup>2</sup>D. A. Shockley, A. H. Marchand, S. R. Skaggs, G. E. Cort, M. W. Burkett, and R. Parker, *Int. J. Impact Eng.* **9**, 263 (1990).

<sup>3</sup>D. E. Grady, Sandia National Laboratories Report No. SAND91-0147, 1991.

<sup>4</sup>D. E. Grady and J. L. Wisc, Sandia National Laboratories Report No. SAND93-0610, 1993.

<sup>5</sup>D. P. Dandekar and D. C. Benfanti, *J. Appl. Phys.* **73**, 673 (1993).

<sup>6</sup>D. E. Grady, Sandia National Laboratories Report No. SAND94-3266, 1995.

<sup>7</sup>D. L. Orphal, R. R. Franzén, A. C. Charters, T. L. Menna, and A. J. Piekutowski, *Int. J. Impact Eng.* **19**, 15 (1997).

<sup>8</sup>R. Feng, Y. M. Gupta, and M. K. Wong, *J. Appl. Phys.* **82**, 2845 (1997).

<sup>9</sup>J. Lankford, W. W. Predebon, J. M. Stachler, G. Subhash, B. J. Pickta, and C. E. Anderson, *Mech. Mater.* **29**, 205 (1998).

<sup>10</sup>G. R. Johnson and T. J. Holmquist, *J. Appl. Phys.* **85**, 8060 (1999).

<sup>11</sup>D. P. Dandekar and P. I. Bartkowiak, in *Fundamental Issues and Applications of Shock Wave and High Strain Rate Phenomena*, edited by K. P. Staudhammer, L. E. Murr, and M. A. Meyers (Elsevier, New York, 2001), pp. 71–77.

<sup>12</sup>G. E. Hauver, P. H. Netherwood, R. F. Blenck, and L. K. Keeskes, 19th Army Science Conference, Florida, June 20–24, 1994.

<sup>13</sup>H. D. Espinosa, N. S. Brar, G. Yuan, Y. Xu, and V. Arrietta, *Int. J. Solids Struct.* **37**, 4893 (2000).

<sup>14</sup>F. I. Grace, in Ref. 11, pp. 421–428.

<sup>15</sup>J. C. LaSalvia, E. J. Horwarth, E. Rapacki, C. James Shih, and M. A. Meyers, in Ref. 11, pp. 437–446.

<sup>16</sup>P. Lundberg, R. Renstrom, and B. Lundberg, *Int. J. Impact Eng.* **24**, 259 (2000).

<sup>17</sup>H. Horii and S. Nemat-Nasser, *Philos. Trans. R. Soc. London, Ser. A* **319**, 337 (1986).

<sup>18</sup>D. E. Grady, *Mech. Mater.* **29**, 181 (1998).

<sup>19</sup>S. Sundaram and R. J. Clifton, *Mech. Mater.* **29**, 233 (1997).

<sup>20</sup>J. N. Johnson, R. S. Hixon, and G. T. Gray, *J. Appl. Phys.* **76**, 5706 (1994).

<sup>21</sup>K. V. Logan, Ph.D. dissertation, Georgia Institute of Technology, 1993.

<sup>22</sup>A. Keller, M.S. thesis, Georgia Tech., 2000.

<sup>23</sup>A. Keller, G. Kennedy, L. Ferranti, M. Zhou, and N. Thadhani, in *Proceedings of the Fourth International Symposium on Impact Engineering*, Kumamoto, Japan, July 2001 (to be published).

<sup>24</sup>G. Gilde, J. W. Adams, M. Burkins, M. Motyka, P. J. Patcl, E. Chin M. Sutaria, M. Rigali, and L. Prokurat Franks, presented at the 25th Annual Cocoa Beach Conference of the American Ceramic Society, Jan. 23–28, 2001.

<sup>25</sup>J. Zhai and M. Zhou, *Int. J. Fract.* **101**, 161 (2000).

<sup>26</sup>M. Zhou and J. Zhai, presented at the American Ceramic Society 102nd Annual Meeting & Exposition, St. Louis, MO, April 30–May 3, 2000.

<sup>27</sup>K. V. Logan, US Patent No. 5,141,900 (25 August, 1992).

<sup>28</sup>E. E. Underwood, *Quantitative Stereology* (Addison-Wesley, Reading, MA, 1970).

<sup>29</sup>G. Kennedy, J. Zhai, R. Russel, M. Zhou, and N. N. Thadhani, presented at the 24th Annual International Conference on advanced Ceramics and Composites, Cocoa Beach, FL, Jan 23–28, 2001.

Quantitative Characterization of Microstructurally Biased Two-Phase  
 $TiB_2 + Al_2O_3$  Ceramics Using Mean Integral Curvature

Louis Ferranti Jr. and Naresh N. Thadhani

School of Materials Science and Engineering, Georgia Institute of Technology,  
771 Ferst Drive, Atlanta, GA 30332-0245

**Abstract**

Microstructurally biased two-phase  $TiB_2 + Al_2O_3$  ceramic with an interconnected or dispersed  $TiB_2$  (minor) phase can be produced by variations in processing parameters. A standard method for quantitatively characterizing the different types of microstructures is necessary to comprehend mechanism(s) that control the generation of the microstructural bias during processing and consequently the resultant properties. In this work, techniques derived from stereology were used to quantitatively characterize the microstructure based on phase size, and phase morphology in terms of phase connectivity and dispersion of the minor phase ( $TiB_2$ ). Mean integral curvature based on area particle count and area tangent count methods were used to quantitatively describe the connectivity of the  $TiB_2$  phase around the  $Al_2O_3$  major phase. The results illustrate that in spite of partial and mixed bias, integral curvature measurements (particularly those based on area tangent count method) provide an accurate means for quantitative characterization of the microstructure and its correlation with measured properties.

Submitted to Metallurgical Transactions, October 2002

## 1. Introduction

Most traditional or advanced ceramics contain more than a single constituent phase. The second phase may either be intentionally added or get picked up during processing. For example, silicon carbide [1], titanium carbide [2], and boron carbide [3] have previously been added to an alumina matrix to inhibit the growth of cracks by providing a plastic “energy-absorbing” barrier and thereby enhancing material properties. The addition of a second phase can also assist in ceramic fabrication. For example, sintering aids such as  $B_4C$  assist in the pressure-less sintering of  $TiB_2$  ceramics resulting in enhanced density and grain growth suppression [4]. On the other hand, impurities such as Fe ( $\sim 0.5\text{wt\%}$ ) cause abnormal grain growth and also yield a low sintered density. Likewise, presence of an unintentionally formed glassy second phase can weaken the ceramic and deteriorate its properties.

Efforts to design ceramics with unique microstructures that provide improved material properties are receiving great interest. Multiphase ceramics are being developed to subside the inherent brittle nature of these materials and attain a combination of high strength and toughness, and wear and impact resistance. For these materials, while it may be required to have a certain desired distribution of the respective phases, the control in forming the complex microstructure is often limited. The properties of two-phase ceramics are influenced by microstructural characteristics, including type of phases present, their size, morphology, and chemical composition. Mechanical properties establish material limitations for specific engineering applications. Many of these properties are dictated not only by the intrinsic properties of the constituent phases, but also the interaction between the phases. Therefore, it is important to correlate processing conditions and constituent phase properties, with final microstructure and the bulk properties of engineered ceramics.

In recent years, several studies have been conducted to produce two-phase  $TiB_2 + Al_2O_3$  ceramics (nominally 30%  $TiB_2$  and 70%  $Al_2O_3$  by weight) for a variety of engineering applications [5-10]. These have been fabricated by manual mixing (MM) of commercially acquired  $TiB_2$  and  $Al_2O_3$  powders and also by using thermite-type self-propagating high-temperature synthesis (SHS) reactions in precursor powders of  $TiO_2$ ,  $B_2O_3$ , and Al [19,20]. Logan [5] and Carney [6] have synthesized microstructurally biased two-phase  $TiB_2 + Al_2O_3$  ceramics with an interconnected or dispersed  $TiB_2$  (minor) phase by simple variations in processing parameters. Micrographs of samples shown in figure 1(a,b) were produced by SHS formed powder after ball-milling and finally hot-pressing. Micrographs of samples shown in figure 1(c,d) were produced by manually mixing commercially-acquired  $TiB_2$  and  $Al_2O_3$  powders and subsequent hot-pressing to form the dense ceramic disks. Microstructures labeled “A” (in figure 1(a)) and “C” (in figure 1(c))

comprising of a relatively continuous interconnected  $TiB_2$  network surrounding an  $Al_2O_3$  phase were qualitatively termed “T@A”. Microstructures labeled “B” (in figure 1(b)) and “D” (in figure 1(d)), with the  $TiB_2$  phase interdispersed within a continuous network of  $Al_2O_3$ , were qualitatively termed “TinA”. Microstructure B reveals a  $TiB_2$  phase that is qualitatively more dispersed (“TinA”) in  $Al_2O_3$ , although, regions with “T@A” are also observed. Furthermore, the size of the two phases is much smaller in microstructure B than in microstructure A. It has been shown that these two-phase ceramics exhibit mechanical properties that are not necessarily based on the rule of mixtures [12], with their compressive strengths being higher than either of the constituents, both at low and high strain rates. It has also been observed that while the compressive yield strength at high strain rates, scales with the grain size (increasing with decreasing grain size), the tensile spall strength increases with increase in connectivity of the  $TiB_2$  phase [13,14]. The dissimilar influence of phase size and microstructural bias on the static and dynamic mechanical properties [11-14] of these two-phase  $TiB_2+Al_2O_3$  ceramics is further complicated by the fact that the microstructural bias revealed in a given sample is not 100%, particularly in samples made by the SHS process. It has also not been established as to which stage(s) of processing most dominantly influences the generation of microstructural bias in terms of phase connectivity or dispersion, starting from pre-mixing of constituent powders of specific morphology, SHS reaction process, ball-milling of reaction products, or hot-pressing parameters used during powder densification.

The objective of the present work was to quantitatively characterize the biased microstructure of two-phase  $TiB_2+Al_2O_3$  ceramics to better understand the evolution of microstructure and control of processing mechanism(s). The approach involved quantitative characterization of the distribution and morphology of the respective  $TiB_2$  and  $Al_2O_3$  phases, followed by the correlation of these characteristics with the various stages of processing of the two-phase ceramic. In the following section, the experimental procedure employed for processing the ceramics, microstructure analysis, and quantitative characterization will be described first, followed by the presentation of observed results and their discussion.

## 2. Experimental Procedure

### 2.1 Processing of Two-Phase $TiB_2+Al_2O_3$ Ceramics

Processing of two-phase  $TiB_2+Al_2O_3$  ceramics (30/70 nominal weight percent ratio) was performed either by manually mixing  $TiB_2$  and  $Al_2O_3$  powders (referred to as MM powders), or by using SHS reaction

(referred to as SHS powders) based on the following reaction:  $3\text{TiO}_2 + 3\text{B}_2\text{O}_3 + 10\text{Al} \rightarrow 3\text{TiB}_2 + 5\text{Al}_2\text{O}_3$ . The MM as well as SHS synthesized powders were ball-milled for various times and subsequently hot-pressed into 98% dense disks, approximately 7.62mm diameter by 1.27mm thick (3" x  $\frac{1}{2}"), and containing different types of biased microstructures, similar to those described in previous studies [5-7]. Variations in ball-milling times, and the pressure and temperature during hot-pressing were used to produce the microstructural bias generated as a result of the complex interactions between the various constituent particles during sintering under pressure.$

The hot-pressed  $\text{TiB}_2 + \text{Al}_2\text{O}_3$  ceramics exhibit a microstructural bias, which shows  $\text{TiB}_2$  either as an interconnected phase surrounding the  $\text{Al}_2\text{O}_3$  phase, or the two phases being simply dispersed, as illustrated in figure 1(a-d). Quantitative characterization using stereological methods was employed to quantitatively describe the relevant features of the microstructures. Features of interest included phase size, interface curvature, and phase connectivity. Microstructural characterization was performed on polished two-dimensional sections (surfaces perpendicular and parallel to pressing direction) of samples cut from the bulk disks of hot-pressed SHS and MM compacts made for this study. Characterization was also performed on hot-pressed samples with microstructures *A* through *D* (surfaces perpendicular to pressing direction only) prepared in previous work by Carney [6]. Micrographs from planar and cross-sectioned surfaces were obtained by imaging the samples using optical microscopy. Quantitative stereology techniques were used to determine the mean integral curvature (using both area particle and area tangent count methods) and phase size. The measurements were performed on a total of four sections, two planar top and bottom surfaces and two cross-sectional surfaces of opposite orientations, cut from the hot-pressed disk shaped samples. Measurements were made on flat sections of the material and then transformed from two-dimensional to three-dimensional approximations of the geometric relations between the different features.

## 2.2 Quantitative Stereological Characterization

An automated quantitative characterization approach was devised for the measurement of mean integral curvature using both area tangent and area particle count methods [15-18]. Both techniques measure the degree of connectivity of the  $\text{TiB}_2$  (minor) phase present in the two-phase ceramic, and are described in more detail in the Appendix. The measure of average curvature according to the particle count method is given by:

$$\bar{k} = \frac{2\pi(N_{A+} - N_{A-})}{L_A} \quad (1)$$

where  $N_{A+}$  is the number of positive loops per unit area (or TiB<sub>2</sub> surrounding Al<sub>2</sub>O<sub>3</sub>),  $N_{A-}$  is the number of negative loops per unit area (or TiB<sub>2</sub> dispersed in Al<sub>2</sub>O<sub>3</sub> matrix), and the total length of the loops per unit area,  $L_A$  is actually the perimeter of the closed loops formed by the phase boundary, which is easily related to the mean linear intercept length,  $\bar{l}$ . The average curvature according to the area tangent count method is given by:

$$\bar{k} = 2 \frac{[T_{A+} - T_{A-}]}{N_L} \quad (2)$$

where,  $T_{A+}$  and  $T_{A-}$  are tangents of convex and concave surfaces of Al<sub>2</sub>O<sub>3</sub> holes and  $N_L$  is the average number of intersections of phase boundaries with a test line per unit length.

Physical observations and quantitative characterization of the microstructures were performed on a Leica DM IRM (Bannockburn, IL) optical microscope operated in a bright field mode with a 20x objective lens. Digital images were obtained using a CoolSNAP CCD video camera (Media Cybernetics; Silver Springs, MD), capable of capturing high-resolution (1390 x 1040 pixels, 4.65 micron pixels) digital images. Images were imported into Image-Pro Plus (Media Cybernetics; Silver Springs, MD) analytical imaging software where the number of features, volume fraction, and average phase size, etc., were measured.

Calculations of mean integral curvature, phase size, and phase distributions were performed using spatially calibrated images. Direct measurements and “real” values could be taken directly from the images. Captured images were 1390 x 1040 pixels, which correspond to a 0.2325 μm/pixel resolution for a 20x objective lens with the smallest resolvable measured feature greater than or equal to 0.70 μm. Measurements were taken on five randomly selected regions for each of the planar and cross-sectional specimen sections.

Curvature and phase size calculations were accomplished by making “basic” measurements on each of the captured images. “Basic” measurements included number of features or phases, average feature size, mean liner intercept, tangent count, and phase volume fraction. Light contrast features (TiB<sub>2</sub>) were first separately counted and then dark contrast features (Al<sub>2</sub>O<sub>3</sub>) were counted for the same image.

Volume fraction and mean linear intercept [18] were automatically calculated using Materials-Pro plug-in (Media Cybernetics; Silver Springs, MD) software for Image-Pro Plus. Volume fraction was calculated according to pixel area fraction for each phase of the material. Automatic thresholding was performed for each image before any measurements were taken. Volume fraction results for respective

phases were used to check the automatic thresholding feature. Typically, automatic thresholding results were close to the nominal 30%  $\text{TiB}_2$  and 70%  $\text{Al}_2\text{O}_3$  phase distribution. Mean linear intercept values were measured using 127 horizontal test lines. The software reported the total line length and number of phase intercept counts.

The area tangent count, used for calculating curvature, was measured using The Image Processing Tool Kit 3.0 software developed by J. C. Russ (Reindeer Games, Inc.; Asheville, NC). The software measures the number of positive and negative tangents formed with the phase boundary and reports the two values separately.

### 3. Results of Quantitative Microstructural Characterization

The ability to quantitatively describe two-phase ceramics requires the consideration of geometrical and topological features such as number, size, and shape of phases and the continuity or connectivity of the constituent phases. Topological properties are unchanged when the structure is stretched or distorted, which has to do with the connectivity of a structure [15]. A multi-phase structure becomes more interconnected as the numbers of separate features (from one phase) decrease, and impinge upon each other forming a system of closed continuous loops. The total connectivity of a structure can be shown to equal the number of features it contains and the value of the net angle subtended by the closed curve forming around the feature (equal to  $2\pi$  radians regardless of shape). Thus, as described in more detail in Appendix -A, the net subtended angle is a “topological invariant” for a closed curve and is related to the measure of integral curvature [15].

Microstructures *A* through *D* fabricated from previous work [6] and shown earlier in figure 1(a)-(d), were examined first. Microstructures *A* and *C* qualitatively show the most connective  $\text{TiB}_2$  phase for the SHS and MM samples respectively as shown in figure 1(a,c). Microstructure *D* has qualitatively the most dispersed  $\text{TiB}_2$  phase, while Microstructure *B* has a combination of features from microstructures *A* and *D*. Sample *A* has several very small  $\text{TiB}_2$  particles ( $<1\mu\text{m}$ ) and also areas where the  $\text{TiB}_2$  phase is very connective. Quantitative measurements of mean integral curvature indicated the same trend. Figure 2(a) shows the values obtained using both curvature calculation methods (area particle count and area tangent count), calculated according to equations (1) and (2), respectively. The structure becomes more connective as the curvature value approaches zero. Typically, area particle count and area tangent count revealed the same basic trend with differences in magnitude ranging from approximately 10 to 20% between the two

methods (for measurements performed on five metallographic locations for each sample). The area tangent count values were however, typically slightly greater than the area particle count values as depicted in figure 2(a). Microstructure *C* has the most connective phase, indicated by area tangent count curvature approaching zero ( $\bar{k} = -0.12\mu\text{m}^{-1}$ ) while microstructure *D* has the most dispersed  $\text{TiB}_2$  phase ( $\bar{k} = -0.46\mu\text{m}^{-1}$ ). Although SHS formed microstructures exhibit both connective and dispersed  $\text{TiB}_2$  regions, microstructure *A* revealed a more connective  $\text{TiB}_2$  phase ( $\bar{k} = -0.40\mu\text{m}^{-1}$ ) in contrast to microstructure *B* ( $\bar{k} = -0.64\mu\text{m}^{-1}$ ).

Compacts were also made in the present work to duplicate the microstructures of samples *A*, *B*, *C*, and *D*, produced in prior work. Samples *A* and *B* were reproduced by ball-milling SHS formed material for 4 and 30 hours, respectively, while samples *C* and *D* were reproduced by using MM technique with no ball-milling and 2 hour ball-milling times, respectively. Figure 2(b) shows a plot of the curvature values (based on area tangent count only) measured for samples *A* through *D* made in prior work and representative samples made from the present work. Good agreement of the overall trends among the curvature values was observed between the two groups of samples.

Additional measurements were performed on SHS formed samples that were subjected to various ball-milling periods (from 1 to 30 hours) before hot-pressing. Optical micrographs in figure 3(a-g) show differences in the microstructural bias following ball-milling for 1, 2, 4, 8, 15, 23, and 30 hours. Each micrograph exhibits regions that have both interconnected and dispersed  $\text{TiB}_2$  phases. It can be seen that the microstructures of samples ball-milled for 1, 2, and 4 hours (figure 3(a-c)) appear to reveal a qualitatively greater degree of  $\text{TiB}_2$  phase connectivity surrounding  $\text{Al}_2\text{O}_3$ . However, as the ball-milling time increases (8 to 30 hours), the bias of  $\text{TiB}_2$  around  $\text{Al}_2\text{O}_3$  gradually shifts to a more dispersed microstructure as shown in figure 3(d-g). Mean integral curvature measured for all SHS prepared samples ball-milled for 1 to 30 hours is shown in figure 4. Samples ball-milled for less than 4 hours, have the most connective  $\text{TiB}_2$  phase around  $\text{Al}_2\text{O}_3$ , while the 30 hour milled samples had a curvature value corresponding to the least interconnected or uniformly dispersed  $\text{TiB}_2$  in  $\text{Al}_2\text{O}_3$  phase.

The effect of ball-milling on MM prepared samples was also determined. Figure 5(a,b) shows micrographs of MM prepared hot-pressed samples with zero and 2 hours of ball-milling. The zero hour ball-milled sample shows the "T@A" microstructure, with continuously interconnected bright-contrast  $\text{TiB}_2$  surrounding the large  $\text{Al}_2\text{O}_3$  phase, while the 2-hour ball-milled sample shows the "TinA" microstructure with  $\text{TiB}_2$  interdispersed in  $\text{Al}_2\text{O}_3$ . Hence, ball-milling not only decreases the size of the constituent phases, but also drastically influences the resulting microstructural bias, more so in MM samples than in SHS samples. Quantitative analysis also measured a 2 hour milled SHS sample having a mean integral curvature

of  $-0.24\mu\text{m}^{-1}$  and a MM sample, following the same ball-milling time, showed a curvature of  $-0.32\mu\text{m}^{-1}$ . Microstructures of corresponding SHS and MM samples on which the curvature and phase size values were measured are shown in figures 6(a) and (b), respectively.

The phase size (calculated using the mean linear intercept method described in Appendix A) for samples: *A*, *B*, *C*, and *D* from prior work (figure 7) and all of the SHS hot-pressed samples made in the present study shown in figure 8. Typically, the  $\text{TiB}_2$  phase for all samples was smaller than that of the  $\text{Al}_2\text{O}_3$  phase. As illustrated in figure 7, the average size of respective phases in SHS samples *A* and *B* is not very different although, the  $\text{Al}_2\text{O}_3$  size distribution in sample *A* is greater than in sample *B*. In contrast, for the MM sample, the size and size distribution of both phases ( $\text{TiB}_2$  and  $\text{Al}_2\text{O}_3$ ) in sample *C* is greater than in sample *D*. The influence of powder ball-milling time on the final phase size of the hot-pressed samples shows that the size of both  $\text{TiB}_2$  and  $\text{Al}_2\text{O}_3$  phases decreases as the powder is milled for longer periods of time as illustrated in figure 8. The 1 hour milled sample has a  $\text{TiB}_2$  and  $\text{Al}_2\text{O}_3$  phase size of 6.3 and  $12.7\mu\text{m}$ , respectively, while the 30 hour milled sample shows a  $\text{TiB}_2$  phase size of  $4.5\mu\text{m}$  and  $9.3\mu\text{m}$  for  $\text{Al}_2\text{O}_3$ . Also, typically a narrower phase size distribution is achieved with increasing ball-milling time. Sampling different orientations did not appear to have a significant effect on the measured phase size values. As an example, the values of average phase sizes for  $\text{TiB}_2$  and  $\text{Al}_2\text{O}_3$  from each sample section of an SHS sample range between  $5.6\mu\text{m}$  and  $6.3\mu\text{m}$  for  $\text{TiB}_2$  and  $11.6\mu\text{m}$  and  $12.5\mu\text{m}$  for  $\text{Al}_2\text{O}_3$ .

To determine the effects of hot-pressing variables, including applied pressure, temperature, and soak time at temperature, each was separately evaluated by measuring phase size and mean integral curvature for the SHS samples. Typically, the density of each sample regardless of the hot-pressing method resulted in a variation less than 1%.

The phase size measurements were examined for samples to see the effect of soak time during hot pressing. Sample SHS-025 and SHS-021 was soaked for 150 and 240 minutes, respectively, during hot-pressing at a temperature of  $1620^\circ\text{C}$ . Correspondingly, the  $\text{TiB}_2$  and  $\text{Al}_2\text{O}_3$  phase sizes were  $5.8$  and  $9.3\mu\text{m}$  for SHS-025 and  $4.8$  and  $10.1\mu\text{m}$  for SHS-021, illustrating a minor effect of soak time on phase size. Pressure application did not appear to affect the final phase size for each constituent phase. Samples SHS-033 and SHS-040 were virtually identical for constant application of pressure versus applying the pressure when the powder compact reaches sintering temperature. Sample SHS-033 (34.5MPa constant application) and SHS-040 (34.5MPa applied once reaching  $1620^\circ\text{C}$ ) had a phase size of  $5.1$  and  $5.5\mu\text{m}$  for the  $\text{TiB}_2$  phase respectively. Similarly, the  $\text{Al}_2\text{O}_3$  phase had sizes of  $10.4$  and  $10.6\mu\text{m}$  for the two samples. Changing the sintering temperature also did not show any effect on the overall phase size. Samples SHS-028 and

SHS-023 were sintered at 1620° and 1700°C, respectively, and differences between the two samples measured phase sizes were 5.0% for TiB<sub>2</sub> and 7.7% for Al<sub>2</sub>O<sub>3</sub>.

In addition to evaluating hot-pressing conditions affecting the constituent phase sizes, the final microstructure morphologies (bias) were also considered. Sample SHS-025 was ball-milled for 30 hours and had an average powder particle size of 6.0  $\mu\text{m}$ . This sample was held at temperature for 150 minutes during hot-pressing. Sample SHS-021 was also ball-milled for 30 hours and had a similar average powder particle size of 5.8  $\mu\text{m}$ , and was held at temperature for a longer time period of 240 minutes. Mean integral curvature for SHS-021 and SHS-025 samples were -0.50 and  $-0.38\mu\text{m}^{-1}$  respectively. The sample held at temperature for a longer time period (SHS-021) had a more dispersed TiB<sub>2</sub> phase based on mean integral curvature values. All other parameters for processing the two samples were similar.

Additionally, no detectable differences were noticed between the samples that were formed using alternate pressure applications and sintering temperatures during processing. Samples SHS-033 (constant pressure of 34.5 MPa) and SHS-040 (pressure of 34.5 MPa once temperature is reached) had mean integral curvature values of -0.40 and  $-0.38\mu\text{m}^{-1}$  respectively and the pressure application method did not appear to affect the curvature value. Similarly, SHS-037 and SHS-023 were sintered at 1620° and 1700°C and mean integral curvature values ranged from -0.44 and  $-0.47\mu\text{m}^{-1}$  respectively. Thus, the variation of hot-pressing parameters measured by curvature appears to vary more with the starting powder particle size as a function of ball-milling time than the effects of sintering temperature and pressure application.

#### 4. Discussion of Results

The main objectives of this research were to quantitatively characterize the biased microstructure of two-phase TiB<sub>2</sub> + Al<sub>2</sub>O<sub>3</sub> ceramics and understand the effects of processing variable that control the phase development and microstructural bias. Quantitative characterization of phase connectivity in each microstructure was achieved by measuring the mean integral using both area particle count and area tangent count methods. The measure of mean integral curvature simply involves counting positive and negative loops when the microstructure is composed of isolated, convex features as seen in microstructure *D* (figure 1(d)). However, it becomes more challenging to measure a microstructure similar to microstructure *A* (figure 1(a)), which comprises of complex interactions between the two phases. Phases intersecting the edge of the micrograph are not counted and provoke measurement errors. However, the area tangent count method does not suffer from this edge effect problem because a test line is swept across the entire field of

view and all features are counted in the measurement. Also, this method looks at phase intersection points that are either within or outside the micrograph boundary, hence, it is a more accurate method. In general, area particle counting can be used for structures that have isolated features of interest within a matrix material, while area tangent count is used for more complicated microstructures where neither phase is fully isolated, similar to those produced by the SHS method.

The phase size for each microstructure is also expected to influence the mean integral curvature values since curvature is essentially the inverse of the radius of particles within the structure. This can be illustrated by looking at the average phase size for the  $\text{TiB}_2$  phase. Essentially, if the phase size is thought of as a particle size, then the average curvature can be calculated by taking the inverse of the particles radius. From this notion and using the  $\text{TiB}_2$  phase size values plotted in figure 7, the most connective phase should be sample C, which is similar to that revealed by the mean integral curvature values indicated using the area tangent count method. Thus, the phase size is influencing the curvature, which is not unexpected. In terms of the effects of processing variables, ball-milling of the powders prior to hot-pressing was observed to have the greatest influence on phase size and the microstructural bias. Hot-pressing temperature and pressure did not appear to affect the microstructural bias or phase size significantly. However, the increased hot-pressing soak time did increase the  $\text{TiB}_2$  phase connectivity while only slightly changing the grain (phase) size.

## 5. Conclusion

Microstructurally biased two-phase  $\text{TiB}_2 + \text{Al}_2\text{O}_3$  ceramics were produced by hot-pressing powders prepared using SHS and MM processing techniques. Stereological measurements were used to quantitatively distinguish the connectivity and dispersion of  $\text{TiB}_2$  in the  $\text{TiB}_2 + \text{Al}_2\text{O}_3$  ceramics. Measurements of a number of features and the mean liner intercept were used to quantify the mean integral curvature as a measure of  $\text{TiB}_2$  phase connectivity. The area tangent count method was found to be more accurate, particularly because the complicated microstructure of the SHS synthesized samples in which neither phase is fully isolated. Amongst the various processing variables, ball-milling time prior to hot-pressing of the powders was observed to have the greatest influence on phase size and breakdown of the microstructural bias.

## **Acknowledgement**

Funding for this research was provided by U.S. Army Research Office, under Grant No. DAAG55-98-1-0454 (Dr. David Stepp, program monitor). The authors would like to express their appreciation to Dr. K.V. Logan for providing samples and motivation for this work. Drs. A. M. Gokhale and M. Zhou by providing valuable discussions and comments towards this work for which they are sincerely acknowledged. Thanks are also extended to Greg Kennedy, Celeste Davis, and Joshua Clarke for their contributions to the present investigation.

## References

1. G.H. Campell *et al.*, "Whisker Toughening: A Comparison Between Aluminum Oxide and Silicon Nitride Toughened with Silicon Carbide," Journal of the American Ceramic Society, 73 (3) (1990), 521-530.
2. R.P. Wahi and B. Ilschner, "Fracture Behavior of Composites Based on  $\text{Al}_2\text{O}_3$ -TiC," Journal of Materials Science, 15 (1980), 875-885.
3. J. Liu and P.D. Ownby, "Boron Containing Ceramic Particulate and Whisker Enhancement of the Fracture Toughness of Ceramic Matrix" (Paper presented at the Proceedings of the 10<sup>th</sup> International Symposium on Boron, Borides, and Related Compounds, Albuquerque, NM, 27-30 August 1990).
4. E.S. Kang *et al.*, "Effect of Iron and Boron Carbide on the Densification and Mechanical Properties of Titanium Diboride Ceramics," Journal of the American Ceramic Society, 72 (10) (1989), 1868-1872.
5. K.V. Logan, "Elastic-Plastic Behavior of Hot-Pressed Composite Titanium Diboride/Alumina Powders Produced Using Self-Propagating High Temperature Synthesis" (Ph.D. Thesis, Georgia Institute of Technology, 1992), 53-73.
6. A.F. Carney, "The Effect of Microstructure on the Mechanical Properties of a 30% Titanium Diboride/70% Alumina Composite" (Master's Thesis, Georgia Institute of Technology, 1997), 24-28, 36-60.
7. L. Ferranti Jr., "Processing and Characterization of Microstructurally Biased Two-Phase Titanium Diboride/Alumina Ceramic ( $\text{TiB}_2 + \text{Al}_2\text{O}_3$ )" (Master's Thesis, Georgia Institute of Technology, 2001), 40-71.
8. N. Stadlbauer, W. Kladnig, and G. Gritzner, " $\text{Al}_2\text{O}_3$ - $\text{TiB}_2$  Composite Ceramics," Journal of Materials Science Letters, 8 (1989), 1217-1220.
9. I. Kimur *et al.*, "Sintering and Characterization of  $\text{Al}_2\text{O}_3$ - $\text{TiB}_2$  Composites," Journal of the European Ceramic Society, 5 (1989), 23-27.
10. J. Liu and P.D. Ownby, "Enhanced Mechanical Properties of Alumina by Dispersed Titanium Diboride Particulate Inclusions," Journal of the American Ceramic Society, 74 (1) (1991), 241-243.
11. G. Gilde, *et al.*, "Processing Aluminum Oxide/Titanium Diboride Composites for Penetration Resistance" (Paper presented at the 25<sup>th</sup> Annual International Conference on Advanced Ceramics & Composites: Conference of the American Ceramic Society, Cocoa Beach, Florida, 23-28 January, 2001).
12. A.R. Keller, "An Experimental Analysis of the Dynamic Failure Resistance of  $\text{TiB}_2/\text{Al}_2\text{O}_3$  Composites" (Master's Thesis, Georgia Institute of Technology, October 2000) 53-103.
13. G. Kennedy, *et al.*, "Influence of Microstructural Bias on the Hugoniot Elastic Limit and Spall Strength of Two-Phase  $\text{TiB}_2 + \text{Al}_2\text{O}_3$  Ceramics," Proceedings of the Conference of the American Physical Society Topical Group on Shock Compression of Condensed Matter, Melville, NY: AIP Conference Proceedings 620, (2001), 755-758.

14. G. Kennedy, *et al.*, "Dynamic Mechanical Properties of Microstructurally-Biased Two-Phase  $TiB_2 + Al_2O_3$  Ceramics" Proceedings of the 2000 International Conference on Fundamental Issues and Applications of Shock Wave and High-Strain-Rate Phenomena, New York, NY: Elsevier, (2001), 63-70.
15. R.T. DeHoff and F.N. Rhines, Quantitative Microscopy, New York, NY: McGraw Hill, (1968), 1-8, 291-325.
16. J.W. Cahn, "The Significance of Average Mean Curvature and its Determination by Quantitative Metallography," Transactions of the Metallurgical Society of AIME, 239 (1967), 610-616.
17. R.T. DeHoff, "The Quantitative Estimation of Mean Surface Curvature," Transactions of the Metallurgical Society of AIME, 239 (1967) 617-621.
18. E.E. Underwood, Quantitative Stereology, Menlo Park, California: Addison-Wesley Publishing Company, (1970), 23-47.
19. A. Varma, "Form From Fire," Scientific America (August 2000), 58-61.
20. A.G. Merzhanov, "Self-Propagating High-Temperature Synthesis: Twenty Years of Search and Findings," Combustion and Plasma Synthesis of High-Temperature Materials Conference, New York, NY: VCH Publishers, Inc., (1990), 1-47.

## APPENDIX

### A.1 Stereology of Mean Integral Curvature

Curvature has been found to be particularly useful in quantifying phase connectivity in two-phase materials. It can be shown that the connectivity of a two-dimensional area is related to the curvature of its boundary [15]. The curvature, which illustrates how sharply a curve bends in 2D or 3D space, can be obtained for any point along a curve and has a local value for a unique point on that curve. Mathematically, curvature is defined as the angle,  $d\theta$  that is subtended on a finite arc segment divided by the length of the arc  $d\lambda$ , as illustrated in figure A1(a) for any two-phase material. The angle  $d\theta$  expresses how much the curve has changed direction for the segment  $d\lambda$ . So, the average rate of change is given by

$$k \equiv \frac{d\theta}{d\lambda}. \quad (1)$$

The local curvature value is comparable to the reciprocal of the radius of a unique circle that exhibits the shape of the curve at a distinctive point. For complex shapes, such as phases comprised of  $\text{TiB}_2$  in an  $\text{Al}_2\text{O}_3$  matrix, a mean curvature can be calculated for all points along the curves formed from their phase boundaries. The average curvature is then given by

$$\bar{k} = \frac{\int k(\lambda) d\lambda}{\int d\lambda}. \quad (2)$$

The mean integral curvature can be found by simply taking the local mean curvature and integrating it over the entire surface of the curve. Substituting equation (1) into (2) and evaluating the integral, results in

$$\bar{k} = \frac{\Delta\theta}{\Delta\lambda}, \quad (3)$$

where,  $\Delta\theta$  is net change of the angle subtended by all the arc segments of the curve. If the particle sections are simply connected, the integral mean curvature can be estimated from the area particle count method

described by DeHoff and Rhines [15]. For a closed curve that encloses the reference matrix phase (TiB<sub>2</sub> surrounding Al<sub>2</sub>O<sub>3</sub>),  $\Delta\theta = +2\pi$ . If the reference phase encloses the second phase (TiB<sub>2</sub> dispersed in Al<sub>2</sub>O<sub>3</sub>) then,  $\Delta\theta = -2\pi$ . The measure of average curvature is then given by

$$\bar{k} = \frac{2\pi(N_{A+} - N_{A-})}{L_A}. \quad (4)$$

In the above equation,  $N_{A+}$  is the number of positive loops per unit area (or TiB<sub>2</sub> surrounding Al<sub>2</sub>O<sub>3</sub> within the TiB<sub>2</sub> phase) and  $N_{A-}$  is the number of negative loops per unit area (or TiB<sub>2</sub> dispersed in Al<sub>2</sub>O<sub>3</sub> matrix). This can be simplified further by recognizing that the total length of the loops per unit area,  $L_A$  is actually the perimeter of the closed loops formed by the phase boundary, which is easily related to the mean linear intercept length,  $\bar{l}$ .

$$L_A = \frac{\pi}{2} N_L = \frac{\pi}{2\bar{l}} \quad (5)$$

In equation (5),  $N_L$  is the average number of intersections of phase boundaries with a test line per unit length. Substituting for  $L_A$  in equation (4) results in the average curvature of isolated TiB<sub>2</sub> phase areas or "particles" and is given by

$$\bar{k} = 4N_{A(\text{net})}\bar{l}. \quad (6)$$

For surfaces that enclose a second phase, the quantity is related to the number of positive and negative loops divided by the total perimeter of both. By convention, the net angle subtended by the reference phase, in this case, Al<sub>2</sub>O<sub>3</sub> has a positive value if enclosed by the minor phase (TiB<sub>2</sub>) and has a negative value if the inverse is true. For this reason, any time a TiB<sub>2</sub> "particle" is counted, it is considered a negative loop. The same is true for counting dispersed Al<sub>2</sub>O<sub>3</sub>, which can be thought of as "holes" in the TiB<sub>2</sub> phase. Determination of curvature then becomes nothing more than an exercise in counting the numbers of TiB<sub>2</sub> "particles" and Al<sub>2</sub>O<sub>3</sub> "holes" and the number of intersections that test lines make with the phase boundaries of the two materials. The mean integral curvature based on loop count is, thus, determined by

equation (6). There is no restriction on the shape of connectedness of the "particles" and those of the boundaries between the reference "particles" and the matrix area [16].

DeHoff [15,17] suggests another way of calculating mean integral curvature using a technique devised by Rhines [15] for very complex microstructures. The definition of mean integral curvature is the same as in equation (1) but the evaluation of the angle subtended by the curves  $\Delta\theta$  is modified. The sampling procedure involves sweeping a test line across a two-dimensional section of the specimen and counting where test lines form tangents with the reference phase. This is illustrated in figure A1(b) for a two-phase ceramic. The total number of tangents divided by the total area evaluated is designated  $T_A$ . The total area that is sampled by all the test lines is equal to  $NL^2$ , where  $N$  is the number of test lines and  $L$  is the length of each test line. The fraction of test lines that form a tangent with the phase boundary arc of length  $dl$  is equal to  $d\theta/\pi$ . Then the number of tangents formed with the arc length  $dl$  per unit area of the sample is simply  $d\theta/\pi A$ . For a curve of finite length, the total number of tangents formed is

$$T_A = \int \frac{d\theta}{\pi A} = \frac{\theta_A}{\pi}, \quad (7)$$

where  $\theta_A$  is the total angle subtended per unit area.

As described earlier for area particle count, it is necessary to choose a convention for defining the reference phase. Following the same sign convention as before, the  $\text{Al}_2\text{O}_3$  phase is again chosen as the reference phase and a positive sign denotes a convex arc segment while a concave arc segment is denoted with a negative sign. A convex arc segment has a normal vector pointing into the reference phase ( $\text{Al}_2\text{O}_3$ ) while the concave arc segments normal vector is pointing away from the reference phase. What follows then is that for all convex arcs,

$$T_{A+} = \frac{\theta_{A+}}{\pi} \quad (8)$$

and for all concave arcs,

$$T_{A-} = \frac{\theta_{A-}}{\pi}. \quad (9)$$

Combining equations (8) and (9) and substituting into equation (3) where,  $\Delta\lambda = L_A = \frac{\pi}{2\bar{l}}$ , gives the expression for mean integral curvature using area tangent count,

$$\bar{k} = 2T_{A(\text{net})}\bar{l}. \quad (10)$$

## A.2 Stereology of Phase Size

Phase size was measured for each of the microstructures discussed in this work using mean intercept length. The geometrical features were approximated and related to an equivalent diameter. To understand how this approximation works, imagine an irregularly shaped convex particle with an array of test lines passing through it. The length of each line within the convex body is measured and varies from zero to some maximum value. The mean value of the intercept lengths will fall between these two extremes. Relating the geometry of a sphere to mean intercept length, which is equal to two-thirds the diameter, one can approximate the geometrical features in terms of an equivalent average diameter.

The mean intercept length for a single particle is defined as

$$\bar{l} = \frac{1}{N} \sum_i^N l_i. \quad (11)$$

where  $l_i$  are the intercept lengths from  $N$  intersections of test lines with phase boundaries. For a given test line length  $L$ ,

$$\bar{l} = \frac{L_L}{N_L}, \quad (12)$$

where  $L_L$  is the fractional length of a test line through a phase and  $N_L$  is the number of intercepts per unit length of a test line. From basic stereological relations [15,18] and considering a multiphase material gives the expression

$$\bar{l} = 4 \frac{(V_V)_\alpha}{(S_V)_\alpha}. \quad (13)$$

where  $V_V$  is the volume fraction and  $S_V$  is the total particle interface area per unit volume. Considering now a single spherical particle again, and substituting the volume of a sphere for  $V_V$  and the area of a sphere for  $S_V$  from equation (13), gives

$$\bar{l} = \frac{4}{3}R = \frac{2}{3}D, \quad (14)$$

where  $R$  is the particle radius and  $D$  is the particle diameter. For a two-phase material,  $D$  is actually the phase size of the  $\alpha$ -phase (reference phase). Substituting equation (14) into equation (13) gives

$$\bar{D} = 3(V_V)_\alpha \bar{l}, \quad (15)$$

which is used to calculate the average phase size of a two-phase material. This gives approximate phase sizes for a complex two-phase material that is otherwise difficult to characterize because of irregular shaped features.

## TABLE OF FIGURES

Figure 1: Two-phase  $\text{TiB}_2 + \text{Al}_2\text{O}_3$  ceramics from Carney [6] showing interconnected  $\text{TiB}_2$  (T@A) microstructures *A* and *C* (a,c), and dispersed  $\text{TiB}_2$  (TinA) microstructures *B* and *D* (b,d).

Figure 2: a) Mean integral curvature measured for microstructures *A*, *B*, *C*, and *D* using area particle count and area tangent count methods. b) Comparison of mean integral curvature measurements using area tangent count method for samples fabricated by Carney [6] (prior work) and Ferranti [7] (present work).

Figure 3: Optical micrographs of hot-pressed sample cross-sections fabricated from SHS powders ball-milled a) 1, b) 2, c) 4, d) 8, e) 15, f) 23, and g) 30 hours.

Figure 4: Effect of ball-milling on measured mean integral curvature values for SHS formed ceramics.

Figure 5: Micrographs of manually mixed samples with a) no ball-milling (MM-017) and b) ball-milling for 2 hours (MM-042).

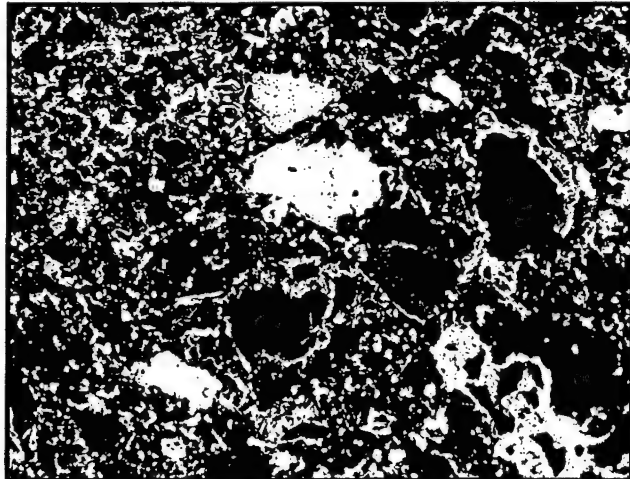
Figure 6: Micrographs of a) SHS-039 and b) MM-042 samples both ball-milled for 2 hours.

Figure 7: Effect of ball-milling time on the average measured phase size for individual  $\text{TiB}_2$  and  $\text{Al}_2\text{O}_3$  phases of SHS formed  $\text{TiB}_2 + \text{Al}_2\text{O}_3$  ceramics.

Figure 8: Average measured phase sizes of  $\text{TiB}_2$  and  $\text{Al}_2\text{O}_3$  for microstructures *A*, *B*, *C*, and *D* made from previous work [6].

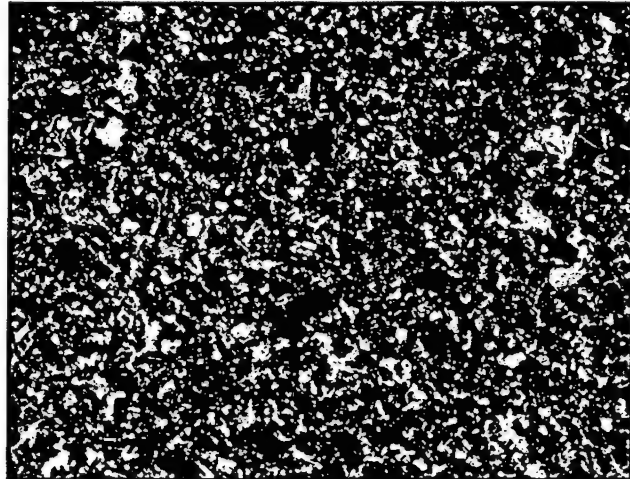
Figure A1: Cross-section of a two-phase material. (a) Arc segments located at the phase boundary subtend some angle  $d\theta$ , which is used in calculating mean integral curvature. (b) A horizontal test line “sweeping” across a two-dimension cross-section forms positive and negative tangent points illustrating area tangent count method for measuring mean integral curvature.

Microstructure *A*, SHS, T@A



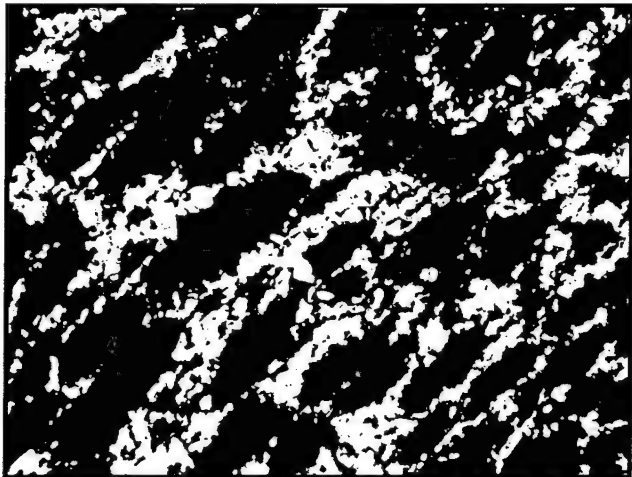
(a)

Microstructure *B*, SHS, TinA



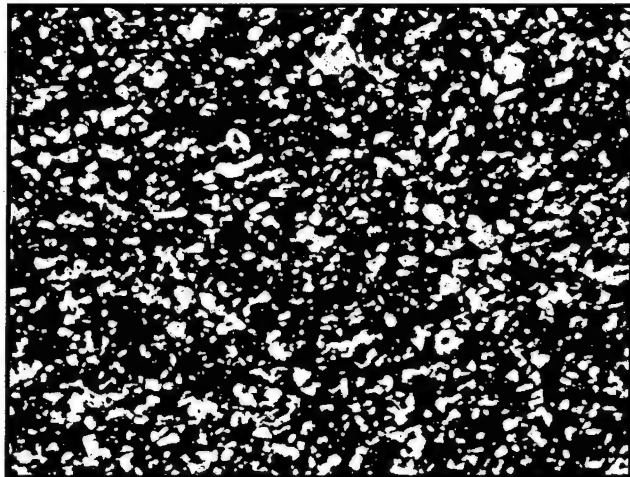
(b)

Microstructure *C*, MM, T@A



(c)

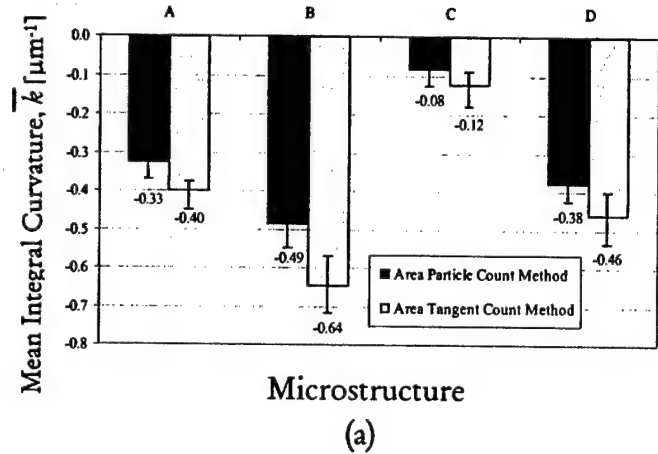
Microstructure *D*, MM, TinA



(d)

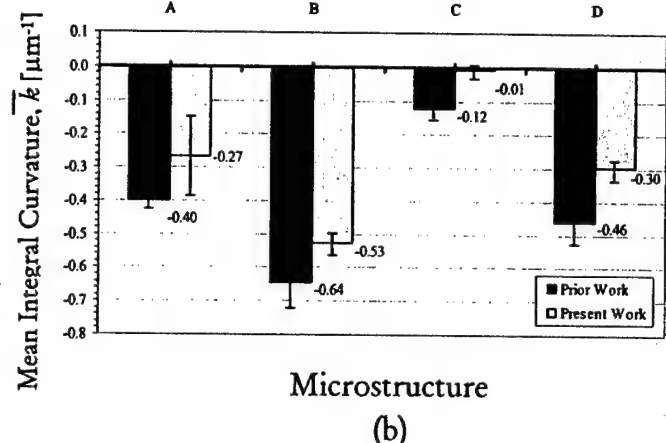
100 $\mu$ m

**Figure 1:** Two-phase TiB<sub>2</sub>+Al<sub>2</sub>O<sub>3</sub> ceramics from Carney [6] showing interconnected TiB<sub>2</sub> (T@A) microstructures *A* and *C* (a,c), and dispersed TiB<sub>2</sub> (TinA) microstructures *B* and *D* (b,d).



Microstructure

(a)



Microstructure

(b)

Figure 2: a) Mean integral curvature measured for microstructures *A*, *B*, *C*, and *D* using area particle count and area tangent count methods. b) Comparison of mean integral curvature measurements using area tangent count method for samples fabricated by Carney [6] (prior work) and Ferranti [7] (present work).

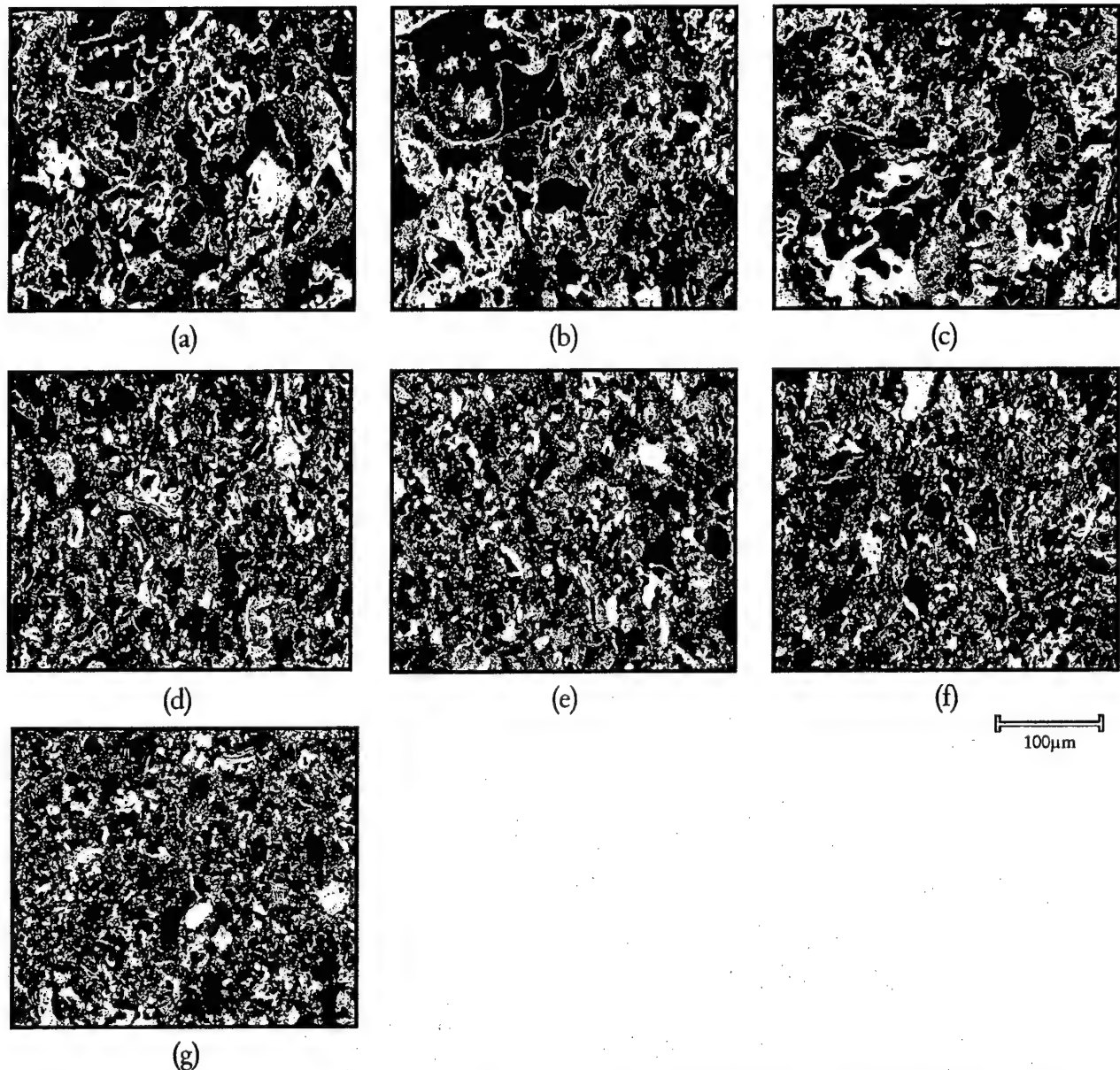


**Figure 3:** Optical micrographs of hot-pressed sample cross-sections fabricated from SHS powders ball-milled a) 1, b) 2, c) 4, d) 8, e) 15, f) 23, and g) 30 hours.

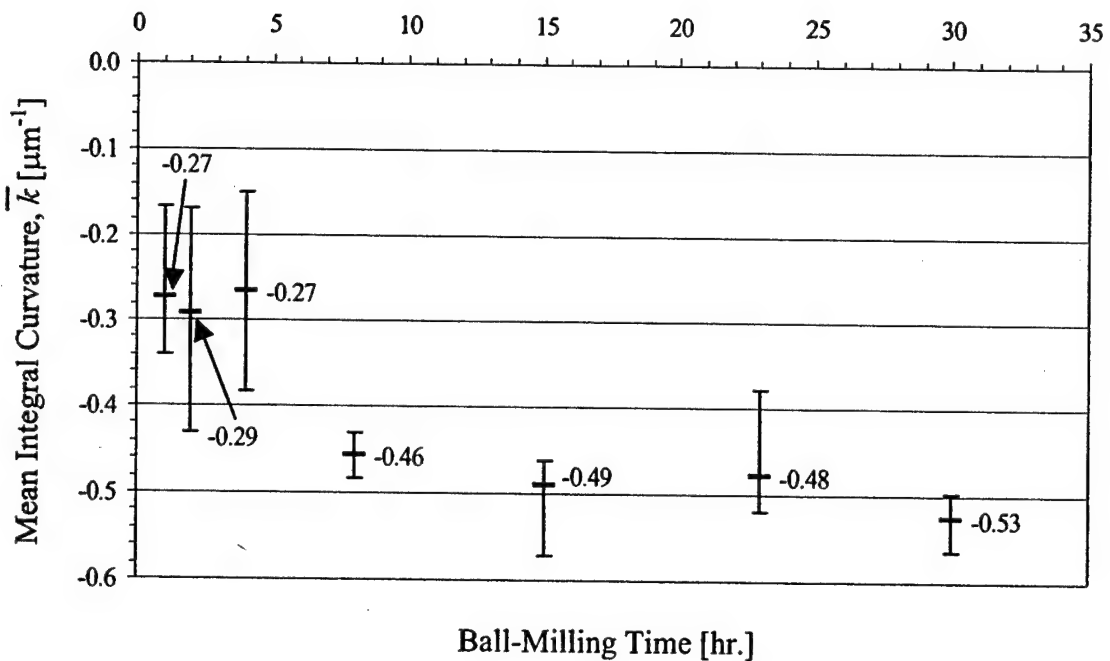


**Figure 4:** Effect of ball-milling on measured mean integral curvature values for SHS formed ceramics.

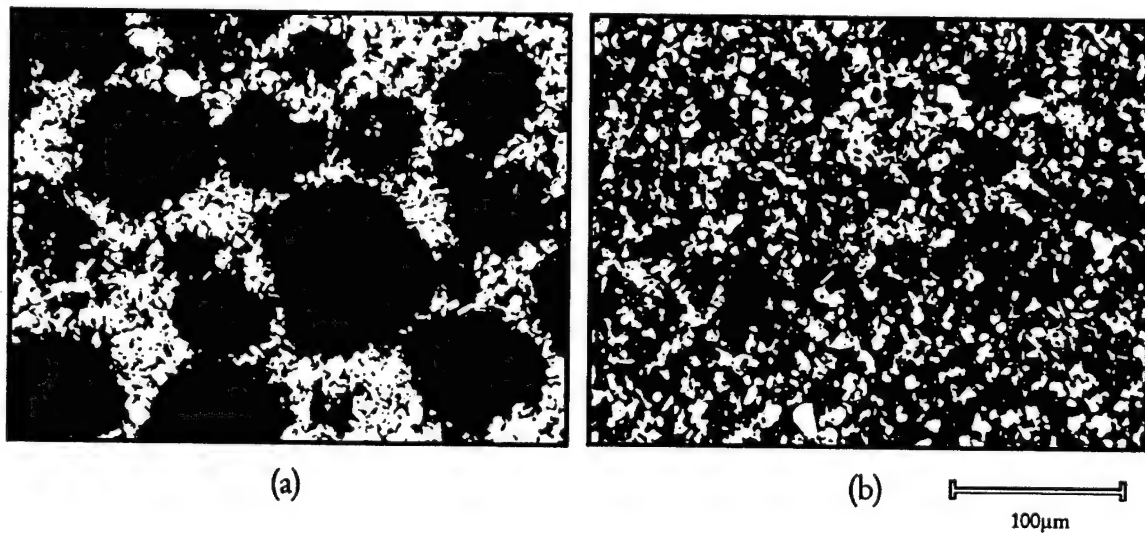


**Figure 5:** Micrographs of manually mixed samples with a) no ball-milling (MM-017) and b) ball-milling for 2 hours (MM-042).

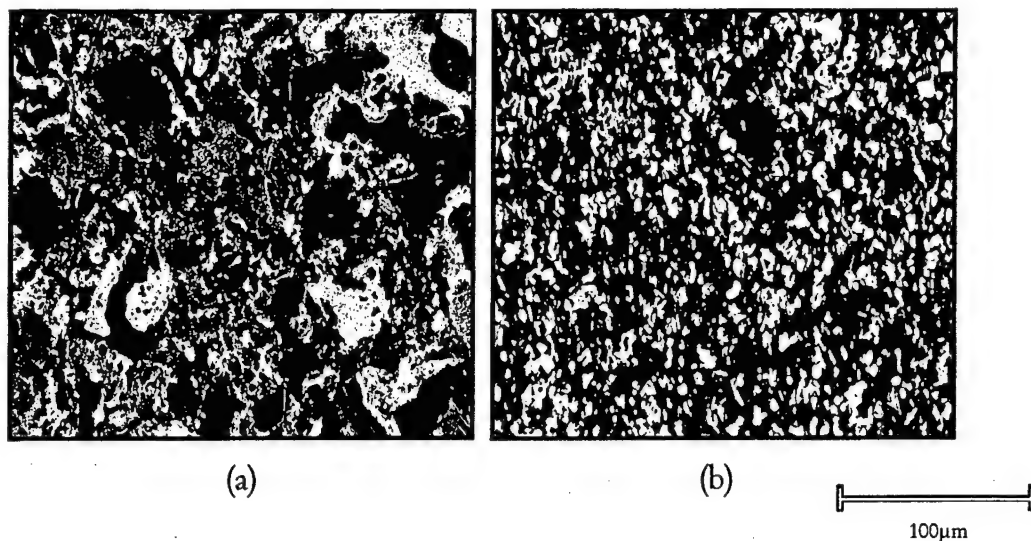


Figure 6: Micrographs of a) SHS-039 and b) MM-042 samples both ball-milled for 2 hours.

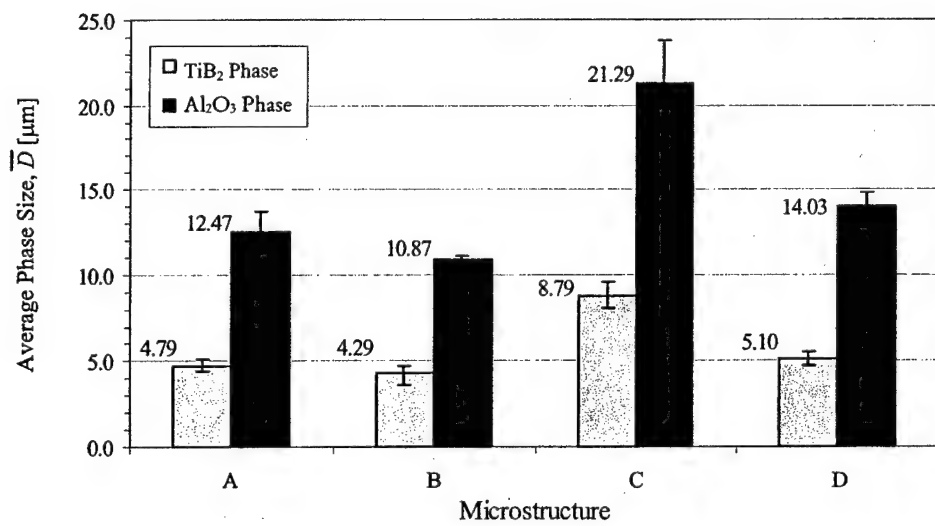
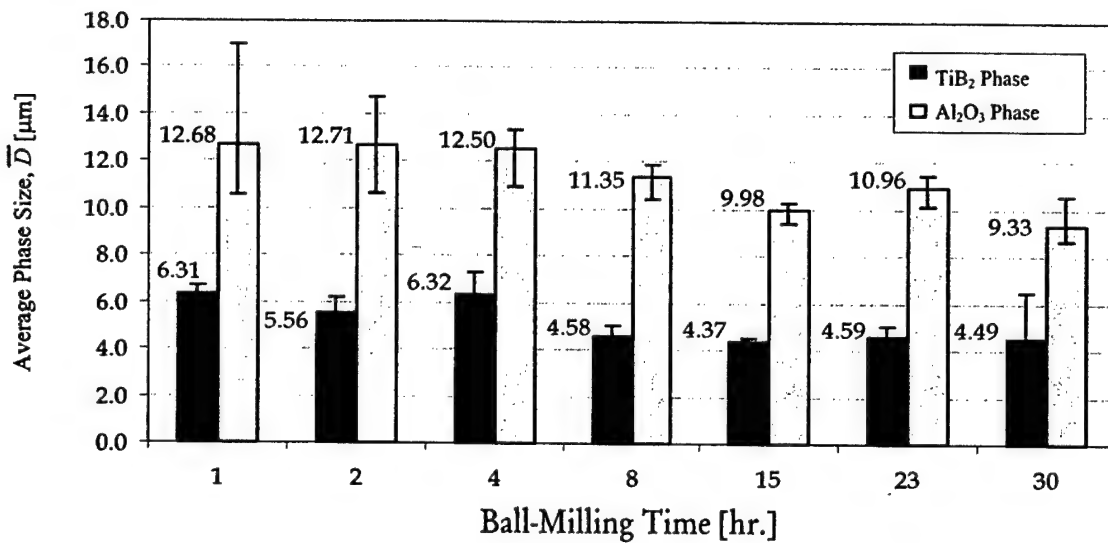
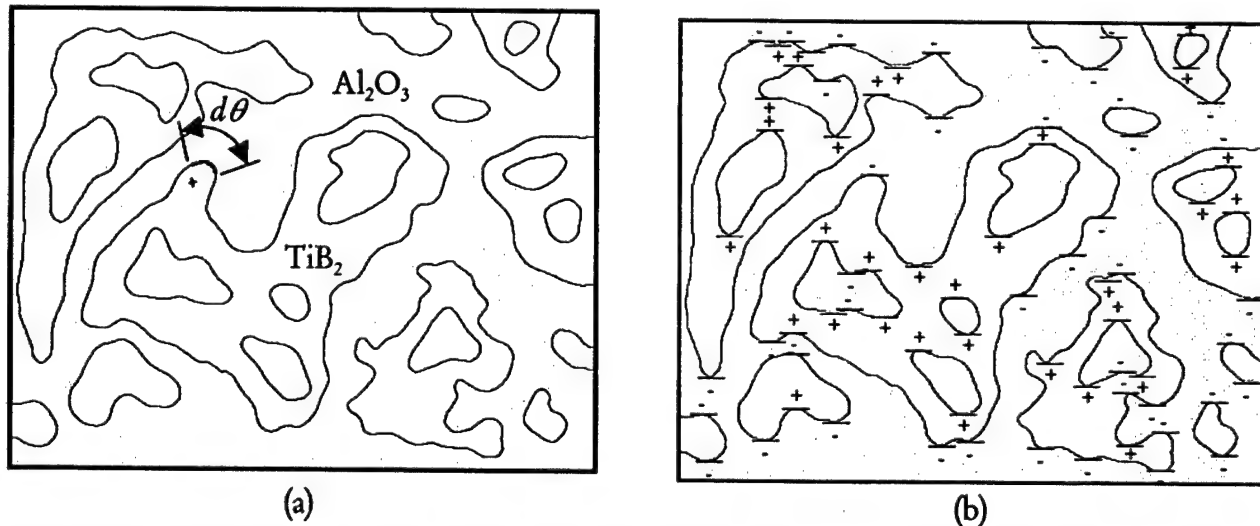


Figure 7: Average measured phase sizes of TiB<sub>2</sub> and Al<sub>2</sub>O<sub>3</sub> for microstructures A, B, C, and D made from previous work [6].



**Figure 8:** Effect of ball-milling time on the average measured phase size for individual TiB<sub>2</sub> and Al<sub>2</sub>O<sub>3</sub> phases of SHS formed TiB<sub>2</sub>+Al<sub>2</sub>O<sub>3</sub> ceramics.



**Figure A1:** Cross-section of a two-phase material. (a) Arc segments located at the phase boundary subtend some angle  $d\theta$ , which is used in calculating mean integral curvature. (b) A horizontal test line “sweeping” across a two-dimension cross-section forms positive and negative tangent points illustrating area tangent count method for measuring mean integral curvature.

## Finite element analysis of micromechanical failure modes in a heterogeneous ceramic material system

J. ZHAI and M. ZHOU\*

The George W. Woodruff School of Mechanical Engineering, Georgia Institute of Technology,  
Atlanta, GA 30332-0405

Received 17 July 1998; accepted in revised form 28 April 1999

**Abstract.** A micromechanical model that provides explicit accounts for arbitrary microstructures and arbitrary fracture patterns is developed and used. The approach uses both a constitutive law for the bulk solid constituents and a constitutive law for fracture surfaces. The model is based on a cohesive surface formulation of Xu and Needleman and represents a phenomenological characterization for atomic forces on potential crack/microcrack surfaces. This framework of analysis does not require the use of continuum fracture criteria which assume, for example, the existence of  $K$ -fields. Numerical analyses carried out concern failure in the forms of crack propagation and microcrack formation. Actual microstructures of brittle alumina/titanium diboride ( $\text{Al}_2\text{O}_3/\text{TiB}_2$ ) composites are used. The results demonstrate the effects of microstructure and material inhomogeneities on the selection of failure modes in this material system. For example, the strength of interfaces between the phases is found to significantly influence the failure characteristics. When weak interfacial strength exists, interfacial debonding and microcrack initiation and growth are the principal mode of failure. When strong interfacial strength is derived from material processing, advancement of a dominant crack and crack branching are observed.

**Key words:** Micromechanical modeling, cohesive force, fracture, heterogeneous materials, elasticity, fracture modes, failure modes, numerical simulation, crack propagation, ceramic composites.

### 1. Introduction

Microscopically inhomogeneous materials derive significantly higher strength and toughness from microscopic reinforcements such as fibers and particles. Composite materials with failure resistance superior to those of their individual constituents have been developed. The enhancement is due to the higher toughness and strength of the additional phases and deformation mechanisms that do not come into play for monolithic materials. In addition to different length scales associated with material inhomogeneities, different time scales are also introduced by composite microstructures under transient loading due to different stress wave speeds or the inertia effect. These spatial and temporal effects provide opportunities for material property enhancement. Material heterogeneities also give rise to multiple failure mechanisms. For example, fracture can occur in different phases and along phase boundaries in heterogeneous materials.

Ceramic composites with microstructural reinforcements over a range of size scales are emerging materials with increasing applications in heat engines, gas turbine blade coatings, cutting tools, drill bits, wear parts, sensors, magnetic recording media, structural components, electronic components, and biomedical devices (e.g. prosthetic articulate joints, orthopedic load-bearing hip implants, spinal surgery implants, dental crowns and bridges). These appli-

\* To whom all correspondence should be addressed, *min.zhou@me.gatech.edu*, 404-894-3294.

cations take advantage of outstanding mechanical and thermomechanical properties at high temperatures (Lange, 1979; Zeng et al., 1992; Matsui et al., 1994), good wear resistance, high elastic moduli and excellent chemical stability (Jones, 1996) of the materials. For instance, ceramic nanocomposites make high performance cutting tools for high-speed machining (Komanduri, 1989). Ceramic composites are also excellent biomaterials since they are biocompatible (fully oxidized and chemically stable) and do not cause adverse effects within a physiological environment. Conversely, their reliability and performance are unaffected by the biological environment in a body. An important issue for ceramic materials in these applications, industrial or biomedical, is their failure resistance, including strength and fracture toughness (Komanduri, 1989; Messer, 1995). The fracture toughness of these materials is at least an order of magnitude lower than those of metals and polymers. Low failure resistance is the most important impediment to their applications, e.g. Willmann (1996a, b). Progress has been made in developing advanced ceramic materials using the fact that the materials derive significantly higher toughness from microscopic or nanosized reinforcements, (Niihara et al., 1990, 1991; Lehman, 1989; Zhao et al., 1993). For example, Niihara et al. (1993) reported that a 5 percent population of SiC nanoparticles increases the tensile strength of  $\text{Si}_3\text{N}_4$  from 350 MPa to 1 GPa and improves its fracture toughness from  $3.25 \text{ MPa}\sqrt{\text{m}}$  to  $4.7 \text{ MPa}\sqrt{\text{m}}$ . Recently, alumina/titanium diboride ( $\text{Al}_2\text{O}_3/\text{TiB}_2$ ) composites with a wide range of microstructural morphologies demonstrate a range of failure resistance and a strong dependence of fracture toughness on microstructure in experiments, (Logan, 1996). These materials are composed of titanium diboride ( $\text{TiB}_2$ ) reinforcements embedded in a matrix of alumina ( $\text{Al}_2\text{O}_3$ ). The principal mode of failure observed in experiments is transgranular fracture of  $\text{Al}_2\text{O}_3$  when strong interfacial strength between the phases is obtained through processing. In contrast, the principal mode of failure is interfacial fracture through microcrack formation when a weak interfacial bonding between the constituents is found. Clearly, interfacial strength significantly influences the overall behavior of the composites. Although microstructure-induced, size-dependent toughening mechanisms at the micro and nano levels are demonstrated approaches for property enhancement, the physics for such effects has not been well quantified. In order to develop more advanced materials, it is necessary to characterize the influences of phase morphology, phase length scale, and interfacial behavior on failure behavior and fracture toughness of these materials.

The dynamic failure of brittle materials has been extensively analyzed by, e.g. Shockley et al. (1974), Grady and Kipp (1979), Lankford (1989), Shockley et al. (1985), Brockenbrough et al. (1988), Longy and Cagnoux (1989), Kishi et al. (1990), Curtin (1991), Shockley et al. (1990), Suresh et al. (1990), Yang et al. (1990), Evans (1991), Kishi (1991), Kobayashi (1991), Espinosa et al. (1992), Ahrens and Rubin (1983), Vekinis et al. (1993), Lankford (1994), Woodward et al. (1994), and Zhou and Curtin (1995). Most available models for the failure are, for the most part, continuum damage theories in which the net effect of fracture is idealized as a degradation of the elasticity modulus, see e.g. Seaman et al. (1985), Curran et al. (1987, 1993), Rajendran (1994), Johnson and Holmquist (1992), Walter (1992), Espinosa et al. (1992, 1995), Ravichandran et al. (1995), and Gao et al. (1997). While capturing the macroscopic or effective response, these models do not explicitly consider the discrete nature of fracture through crack growth and coalescence. Thus, the models lack the ability to account for the interaction between cracks and resolve specific failure modes and failure patterns. In addition, the effects of microstructural inhomogeneities of different size scales such as inclusions, fibers and grains on crack path and fracture toughness cannot be explicitly analyzed.

The complex morphologies of material microstructures preclude the application of analytical methods. Explicit micromechanical modeling and simulation represent a unique and attractive means for analyzing micro and meso failure mechanisms and for elucidating scaling laws. Through the consideration of representative samples of actual microstructures, the effects of various fracture mechanisms can be delineated. The required features of this framework should include

- (1) explicit account of real, arbitrary material microstructures,
- (2) explicit resolution of fracture in a non-constrained (arbitrary crack paths or microcrack patterns) manner, and
- (3) freedom from limitations of fracture criteria applicable only over certain length scales (e.g. continuum criteria which assume the existence of  $K$ -fields).

Combined use of the cohesive surface approach of Xu and Needleman (1994, 1997) and bulk constitutive laws is a good candidate for providing such a framework. A similar technique has also been used by Camacho and Ortiz (1996) and Ortiz (1996) in the analysis of dynamic failure of materials.

A cohesive finite element method (CFEM) for explicit micromechanical fracture analysis is developed and used here. This approach involves the combined use of a cohesive surface characterization for crack surfaces and bulk constitutive laws for solid constituents. In addition to traditional finite elements, all boundaries between the finite elements are cohesive surfaces serving as potential crack paths. Like in Xu and Needleman (1994), the crack surfaces are regarded as cohesive surfaces exhibiting traction forces which are functions of interfacial separations. The concept of cohesive crack faces can be traced back to the pioneering work of Dugdale (1960) and Barrenblatt (1962). The additional interfacial discretization in the CFEM allows the cohesive surfaces to permeate the whole microstructure as an *intrinsic* part of the material characterization. Consequently, fracture is an *inherent* attribute of the discrete model. Explicit account is taken of arbitrary crack and microcrack patterns as well as of arbitrary microstructures. Intergranular and transgranular fractures evolve as natural outcomes of the cohesive responses within each constituent, the cohesion between the phases, and the bulk constitutive behavior of the phases. The cohesive relations represent phenomenological characterizations of atomistic attraction and repulsion forces which vary with inter-atomic displacements. It is surmised that characterizations of the inter-atomic interactions are possible on the nano, micro, meso and continuum levels. When combined with bulk constitutive laws appropriate at the corresponding length scales, these cohesive models can provide a unified framework for explicit account and simulation of fracture processes over multiple length scales. This novel approach does not require any *a priori* crack initiation or propagation criteria required by traditional fracture mechanics approaches, such as the attainment of critical values of stress intensity factors or maintenance of constant energy release rate. The difference is significant because the concept or validity of singular crack tip fields ceases to exist when one approaches the grain, subgrain, or atomic scales. Since the CFEM model has the inherent properties of deformation and fracture upon loading, it possesses a predictive power similar to that of discrete molecular dynamics models concerning fracture initiation, fracture path, crack speed and microcrack patterning.

Analyses in this paper focus on the  $\text{TiB}_2/\text{Al}_2\text{O}_3$  material system developed by Logan (1996) because of its application potential and because of the fact that processing has been demonstrated to be an effective means to alter the mechanical properties of the materials through microstructural modification. This selection is also motivated by the opportunity for

a joint program combining micromechanical modeling, mechanical testing and materials synthesis aimed at improving the fracture resistance of a class of ceramic composites. While a specific material system is considered here, the approach for explicit fracture modeling can be directly applied to other material systems. Understanding of microstructure-induced toughening mechanisms is also directly relevant for other composite materials.

## 2. Problem formulation

To account for finite strain involved in crack tip regions, a Lagrangian finite deformation formulation is used. The independent variables are the position of a material point in the reference configuration  $\mathbf{x}$ , and time  $t$ . Relative to a fixed Cartesian frame  $\{\xi^i\}$ , a material point initially at  $\mathbf{x}$  occupies position  $\bar{\mathbf{x}}$  in the current configuration. The displacement vector and the deformation gradient are defined as  $\mathbf{u} = \bar{\mathbf{x}} - \mathbf{x}$  and  $\mathbf{F} = \partial \bar{\mathbf{x}} / \partial \mathbf{x}$ , respectively. The principle of virtual work includes a contribution from the cohesive surfaces and is written as

$$\int_V \mathbf{s} : \delta \mathbf{F} dV - \int_{S_{\text{int}}} \mathbf{T} \cdot \delta \Delta dS = \int_{S_{\text{ext}}} \mathbf{T} \cdot \delta \mathbf{u} dS - \int_V \rho \frac{\partial^2 \mathbf{u}}{\partial t^2} \cdot \delta \mathbf{u} dV, \quad (1)$$

where  $\mathbf{s} : \delta \mathbf{F} = s^{ij} \delta F_{ji}$ ,  $\mathbf{s}$  is the nonsymmetric first Piola-Kirchhoff stress;  $\Delta$  is the displacement jump across a pair of cohesive surfaces;  $V$ ,  $S_{\text{ext}}$  and  $S_{\text{int}}$  are the volume, external surface area and internal cohesive surface area, respectively, of the body in the reference configuration. The density of the material in the reference configuration is  $\rho$ . Also,  $\delta \mathbf{F}$ ,  $\delta \Delta$ , and  $\delta \mathbf{u}$  denote admissible variations in  $\mathbf{F}$ ,  $\Delta$  and  $\mathbf{u}$  respectively. The traction vector  $\mathbf{T}$  and the surface normal in the reference configuration  $\mathbf{n}$  are related through  $\mathbf{T} = \mathbf{n} \cdot \mathbf{s}$ . The volumetric constitutive law is hyperelastic so that

$$\mathbf{S} = \frac{\partial W}{\partial \mathbf{E}}, \quad (2)$$

where  $\mathbf{S} = \mathbf{s} \cdot \mathbf{F}^{-T}$  is the second Piola-Kirchhoff stress. The strain energy density  $W$  is taken to be

$$W = \frac{1}{2} \mathbf{E} : \mathbf{L} : \mathbf{E} \quad (3)$$

with

$$\mathbf{L} = \frac{E}{1+\nu} \left( \mathbf{II} + \frac{\nu}{1-2\nu} \mathbf{I} \otimes \mathbf{I} \right) \quad (4)$$

being the tensor of isotropic elastic moduli.  $E$  and  $\nu$  are the Young's modulus and Poisson's ratio, respectively.  $\mathbf{E}$  is the Lagrangian strain given by

$$\mathbf{E} = \frac{1}{2} (\mathbf{F}^T \cdot \mathbf{F} - \mathbf{I}). \quad (5)$$

Also in the above formulas,  $\mathbf{II}$  is the fourth order identity tensor,  $\mathbf{I}$  is the second order identity tensor,  $\mathbf{I} \otimes \mathbf{I}$  denotes the tensor product of two second order tensors, and  $(\cdot)^T$  and  $(\cdot)^{-T}$  denote inverse and inverse transpose, respectively. The resulting stress-strain relation specifies a linear relation between  $\mathbf{S}$  and  $\mathbf{E}$ , i.e.,

$$\mathbf{S} = \frac{E}{1+\nu} \mathbf{E} + \frac{E\nu}{(1+\nu)(1-2\nu)} (\text{tr } \mathbf{E}) \mathbf{I}. \quad (6)$$

Under the conditions of infinitesimal strains, this relation approximates the isotropic, linear elastic behavior. A discussion of linear stress-strain relations for finite deformations is given by Batra (1999).

The constitutive law for cohesive surfaces relates the traction and displacement jumps across crack surfaces and is also taken to be hyperelastic so that any dissipation associated with separation is neglected. Assuming the surface potential energy is  $\phi$ , the traction on the cohesive surfaces can be derived through

$$\mathbf{T} = -\frac{\partial \phi}{\partial \Delta} \quad (7)$$

In two dimensions, the specific form of  $\phi$  is given by Xu and Needleman (1994) as

$$\phi(\Delta) = \phi_0 - \phi_0 \left( 1 + \frac{\Delta_n}{\delta_n} \right) \exp \left( -\frac{\Delta_n}{\delta_n} \right) \exp \left( -\frac{\Delta_t^2}{\delta_t^2} \right), \quad (8)$$

where  $\Delta_n = \mathbf{n} \cdot \Delta$  and  $\Delta_t = \mathbf{t} \cdot \Delta$  are the normal and tangential displacement jumps, with  $\mathbf{n}$  and  $\mathbf{t}$  denoting unit vectors along the surface normal and tangent in the reference configuration, respectively. Potential  $\phi$  is written such that  $\phi(\Delta)|_{|\Delta|=0} = 0$  and therefore  $\phi_0 = \phi(\Delta)|_{|\Delta| \rightarrow \infty}$  is the work of separation. Two special paths of decohesion are considered to illustrate the variations of the cohesive traction components. The first path is pure normal separation with tangential traction component  $T_t = \mathbf{t} \cdot \mathbf{T} = 0$  and tangential separation  $\Delta_t = 0$ . The second path is pure tangential separation with normal traction component  $T_n = \mathbf{t} \cdot \mathbf{T} = 0$  and normal separation  $\Delta_n = 0$ . The works of normal and tangential separations along these two paths are equal to each other and are taken to be  $\phi_0 = e\sigma_{\max}\delta_n = \sqrt{\frac{e}{2}}\tau_{\max}\delta_t$ , with  $e = \exp(1) = 2.718281829$ .  $\delta_n$  and  $\delta_t/\sqrt{2}$  are normal and shear displacement jump values at which maximum normal stress  $\sigma_{\max}$  and maximum shear stress  $\tau_{\max}$  occur, respectively.

The cohesive surface traction components obtained from (7) and (8) are

$$T_n(\Delta) = -\frac{\phi_0 \Delta_n}{\delta_n^2} \exp \left( -\frac{\Delta_n}{\delta_n} \right) \exp \left( -\frac{\Delta_t^2}{\delta_t^2} \right), \quad (9)$$

and

$$T_t(\Delta) = -\frac{2\phi_0 \Delta_t}{\delta_t^2} \left( 1 + \frac{\Delta_n}{\delta_n} \right) \exp \left( -\frac{\Delta_n}{\delta_n} \right) \exp \left( -\frac{\Delta_t^2}{\delta_t^2} \right). \quad (10)$$

These relations are illustrated in Figure 1. Clearly, there are cross dependencies of normal traction ( $T_n$ ) on shear displacement jump ( $\Delta_t$ ) and shear traction ( $T_t$ ) on normal displacement jump ( $\Delta_n$ ). In general, the traction components first increase with the displacement jumps and decrease with further increase in separations after displacement jumps exceed certain values. Both traction components approach zero as  $|\Delta| \rightarrow \infty$ . Figure 1(a) shows the dependence of normal traction  $T_n$  on normal separation  $\Delta_n$  and shear separation  $\Delta_t$ . When normal separation is attempted while  $\Delta_t$  is held to be zero ( $\Delta_n > 0$  and  $\Delta_t = 0$ ),  $T_n$  first increases with  $\Delta_n$  for  $0 < \Delta_n < \delta_n$ ; it reaches maximum stress  $\sigma_{\max}$  at  $\Delta_n = \delta_n$ , decreases with  $\Delta_n$  thereafter and approaches zero as  $\Delta_n$  goes to  $\infty$ . A nonzero shear separation  $\Delta_t$  always reduces the value of  $T_n$  required for causing the same amount of normal separation  $\Delta_n$ . The normal traction component increases rapidly with negative normal separations ( $\Delta_n < 0$ , representing

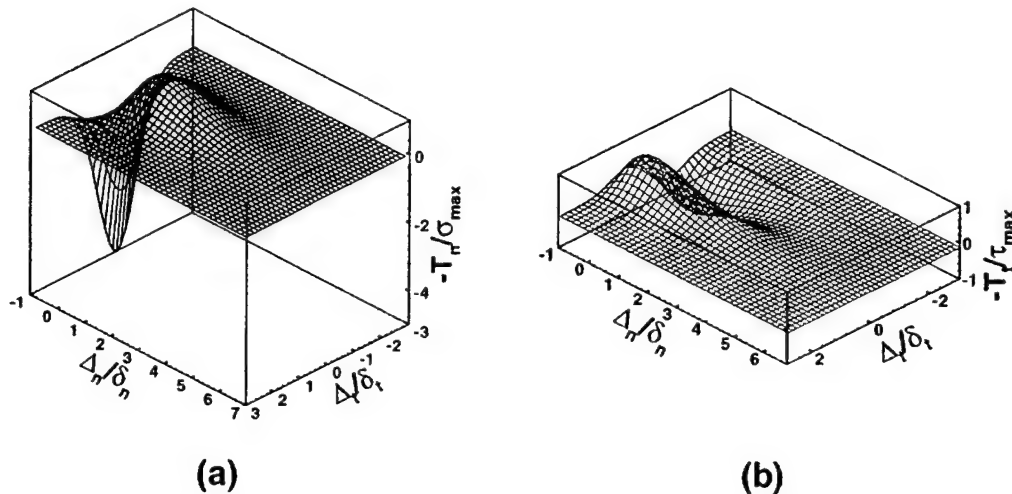


Figure 1. An illustration of the constitutive behavior of cohesive surfaces. (a) normal traction. (b) shear traction.

interpenetration of the crack surfaces). This part of the relation simulates the strong atomistic repulsion during compression. Figure 1(b) shows the variation of  $T_t$  with  $\Delta_t$  and  $\Delta_n$ . When shear separation is attempted while  $\Delta_n$  is held to be zero ( $\Delta_t \neq 0$  and  $\Delta_n = 0$ ),  $T_t$  first increases with  $|\Delta_t|$  for  $0 < |\Delta_t| < \delta_t/\sqrt{2}$ ; it reaches maximum stress  $\tau_{\max}$  at  $|\Delta_t| = \delta_t/\sqrt{2}$ , decreases with  $|\Delta_t|$  thereafter and approaches zero as  $|\Delta_t|$  goes to  $\infty$ . A nonzero normal separation  $\Delta_n$  always reduces the value of  $T_t$  required for causing the same amount of shear separation  $\Delta_t$ .

The balance of energy requires that the total external work  $\mathcal{P}$  done to a body to be equal to the sum of the strain energy  $\mathcal{W}$  stored in the bulk material, the kinetic energy  $\mathcal{K}$  in the body and the cohesive surface energy  $\Phi$  in crack surfaces, i.e.

$$\mathcal{P} = \int_0^t \int_{S_{\text{ext}}} \mathbf{T} \cdot \frac{\partial \mathbf{u}}{\partial t} dS dt = \mathcal{K} + \mathcal{W} + \Phi, \quad (11)$$

where

$$\left. \begin{aligned} \mathcal{K} &= \int_V \frac{1}{2} \rho \frac{\partial \mathbf{u}}{\partial t} \cdot \frac{\partial \mathbf{u}}{\partial t} dV, \\ \mathcal{W} &= \int_V W dV, \\ \Phi &= \int_{S_{\text{int}}} \phi dS. \end{aligned} \right\} \quad (12)$$

Cohesive energy  $\Phi$  is the amount of energy spent on generating new crack surfaces, therefore represents a measure of the energy consumption on fracture. Under the same loading conditions, the higher the  $\Phi$  required for generating the same amount of crack surfaces, the higher the fracture resistance of the material. In the analyses carried out there, this energy is used to compare the fracture resistance of specimens with different microstructures under the same overall remote loading.

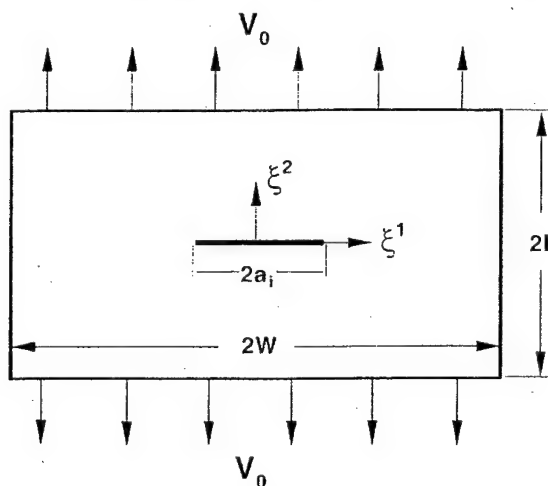


Figure 2. Problem analyzed: a centered-cracked specimen under tensile loading.

### 3. Problem analyzed

Computations are carried out for a center-cracked specimen, as illustrated in Figure 2. The specimen has an initial height of  $2H = 1.6$  mm and an initial width of  $2L = 1.6$  mm. An initial crack of length  $2a_i = 0.4$  mm exists along the  $\xi^1$  axis. Only one half of the specimen ( $\xi^1 > 0$ ) is discretized and modeled in the simulations because of the symmetry with respect to the  $\xi^2$  axis. Conditions of plain strain are assumed to prevail. The small region in front of the crack tip contains microstructures digitized from micrographs of actual composite materials, see Figure 3. Inside this region, the material inhomogeneities and material distribution are explicitly modeled. Digitized microstructures of actual  $\text{Al}_2\text{O}_3/\text{TiB}_2$  composites are used in the analyses. The particular microstructural morphologies analyzed are shown in Figure 4. The microstructure in Figure 4(a) has a  $\text{TiB}_2$  grain volume fraction of approximately 32 percent. The average grain size is  $10 \mu\text{m}$ . This microstructure is referred to as the base microstructure throughout this paper. In addition to the base microstructure, two variations are also considered. The first variation, shown in Figure 4(b), is obtained from the base microstructure by reducing the volume fraction of the  $\text{TiB}_2$  grains from 32 to 15 percent. This reduction is achieved by successively removing layers of  $\text{TiB}_2$  from the grains and converting them into the matrix material,  $\text{Al}_2\text{O}_3$ . The second variation is shown in Figure 4(c) and is obtained from the base microstructure by shrinking uniformly the constituents in the microstructure. The ratio of reduction is 50 percent in each direction therefore the average grain size in Figure 4(c) is one half of that in Figure 4(a). The volume fractions of the phases, nevertheless, remain the same as those in the base microstructure. Each of the phases behaves hyperelastically according to (2) and (3). Depending on material properties, boundary conditions and loading, fracture is possible inside each of the phases and along the interfaces between the phases. The bulk properties of each finite element are those for either the grains or those for the matrix. The properties of each segment of potential fracture surface are specified according to its location as those belonging to the  $\text{Al}_2\text{O}_3$  matrix, the  $\text{TiB}_2$  grains or the matrix/grain interfaces.

Materials outside the crack-tip region are assumed to be homogeneous and are assigned a set of effective parameters representative of those for the  $\text{Al}_2\text{O}_3/\text{TiB}_2$  ceramic composite. Both regions are discretized in the same manner, using both the bulk and the cohesive surface

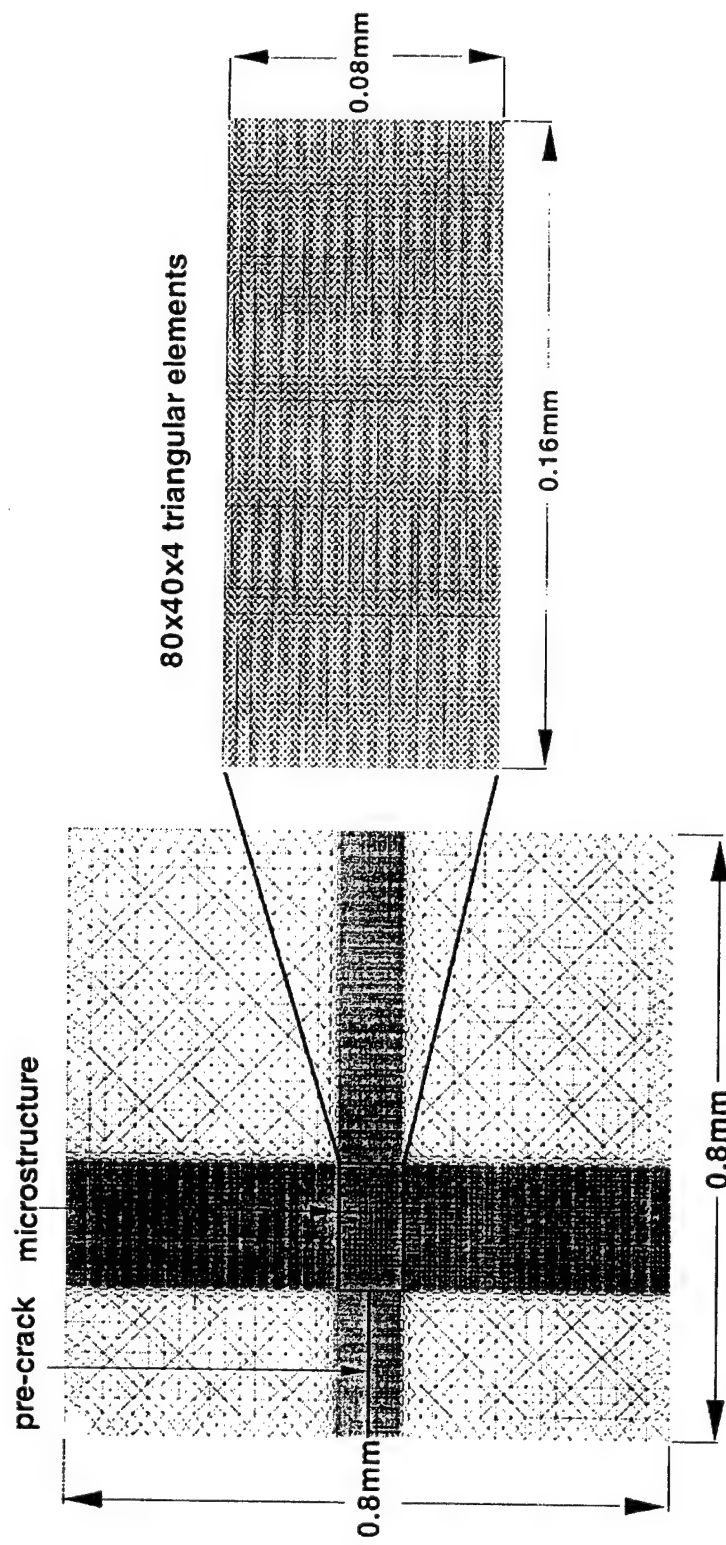
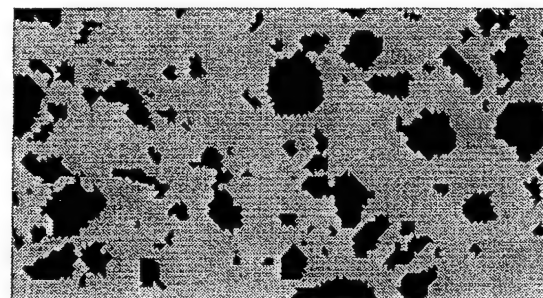
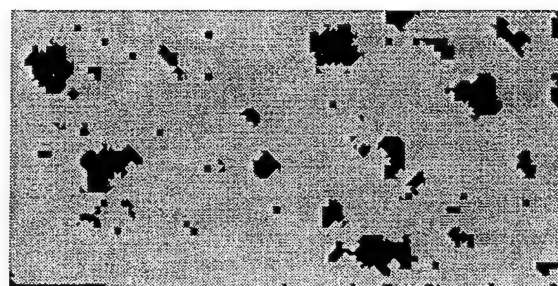


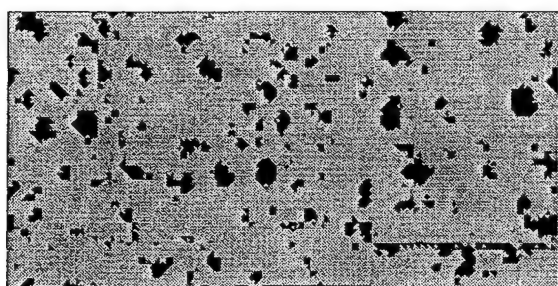
Figure 3. Finite element model and mesh for the specimen.



(a)



(b)



(c)

Figure 4. Microstructural morphologies analyzed: (a) base microstructure, (b) lower volume fraction, (c) smaller grain size.

constitutive descriptions. The specimen is stress-free and at rest initially. Tensile loading is applied by imposing symmetric velocity boundary conditions along the upper and lower edges of the specimen. For the results discussed here, the imposed boundary velocity is  $V_0 = 50$  m/s for each edge with a linear ramp from zero to this maximum velocity in the first  $0.01 \mu\text{s}$  of

Table 1. Bulk material properties

Compound	Density (kg/m <sup>3</sup> )	$K_{IC}$ (MPa $\sqrt{m}$ )	$E$ (GPa)	$\nu$	$c_L$ (m/s)	$c_S$ (m/s)	$c_R$ (m/s)
Al <sub>2</sub> O <sub>3</sub>	3990	4.0	340	0.23	9939	5885	5379
TiB <sub>2</sub>	4520	7.2	500	0.12	10694	7027	6267
Composite	4120	3.6	415	0.15	10300	6609	5936

Table 2. Constitutive parameters for cohesive surfaces

Cohesive surface pair	$\sigma_{max}$ (GPa)	$\tau_{max}$ (GPa)	$\delta_n, \delta_t$ ( $\mu$ m)	$\phi_0$ (J/m <sup>2</sup> )
Al <sub>2</sub> O <sub>3</sub>	34	78.2	0.0005	46.2
TiB <sub>2</sub>	50	11.5	0.001	135.9
Composite	41.5	95.5	0.0003	33.8
Al <sub>2</sub> O <sub>3</sub> /TiB <sub>2</sub> (Strong Interface)	34	78.2	0.001	92.4
Al <sub>2</sub> O <sub>3</sub> /TiB <sub>2</sub> (Weak Interface)	1.7	3.91	0.001	4.6

loading. All other specimen surfaces have traction-free boundary conditions. Specifically, the loading conditions are

$$\dot{u}^2(\xi^1, \pm H, t) = \begin{cases} \pm \frac{t}{0.01} V_0, & t < 0.01 \mu s, \\ \pm V_0, & t > 0.01 \mu s. \end{cases} \quad -L < \xi^1 < L; \quad (13)$$

$$T^1(\xi^1, \pm H, t) = 0, \quad -L < \xi^1 < L; \quad (14)$$

$$T^1(\pm L, \xi^2, t) = T^2(\pm L, \xi^2, t) = 0, \quad -H < \xi^2 < H. \quad (15)$$

The material and model parameters are listed in Table 1 (bulk properties) and Table 2 (cohesive surface constitutive properties). For comparison and analysis purposes, the speeds for the longitudinal stress waves ( $c_L$ ), the shear stress waves ( $c_S$ ) and the Rayleigh surface waves ( $c_R$ ) are also listed in Table 1. The choice of the cohesive law parameters assumes that  $\sigma_{max} = E/10$ , with  $E$  being the Young's modulus, and  $\phi_0 = \frac{(1-\nu^2)K_{IC}^2}{E}$ , with  $K_{IC}$  being the mode-I fracture toughness of the materials in question.

#### 4. Finite element method

Finite element discretization is based on linear-displacement triangular elements arranged in a 'crossed-triangle' quadrilateral pattern. Neighboring elements are connected through cohesive

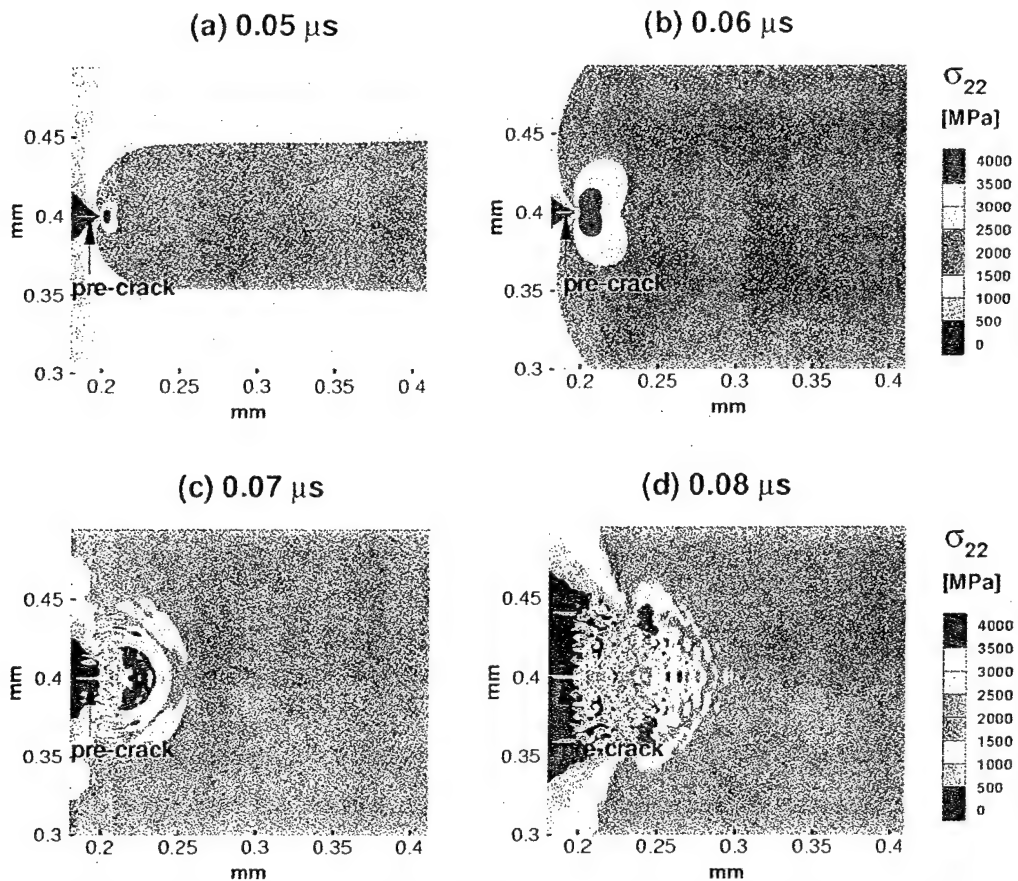


Figure 5. Distributions of  $\sigma_{22}$  at four different times for a specimen of pure  $\text{Al}_2\text{O}_3$ .  $V_0 = 50 \text{ m/s}$ .

surfaces. Hence, for the uniform mesh region in front of the crack tip in Figure 3, the cohesive surfaces are initially oriented along four directions, horizontal ( $0^\circ$ ), vertical ( $90^\circ$ ), positive and negative 45 degrees ( $\pm 45^\circ$ ). Since a very fine mesh is used (the element size is  $2 \mu\text{m}$ ), arbitrary fracture paths or patterns can be resolved. When the finite element discretization of the displacement field is substituted into the principle of virtual work (1), the discretized equations of motion take the form

$$\mathbf{M} \frac{\partial^2 \mathbf{U}}{\partial t^2} = \mathbf{R}, \quad (16)$$

where  $\mathbf{U}$  is the vector of nodal displacements,  $\mathbf{M}$  is the nodal mass matrix and  $\mathbf{R}$  is the nodal force vector consisting of contributions from the bulk elements and the cohesive surfaces. A lumped mass matrix is used in (16) instead of the consistent mass matrix for reasons of efficiency and accuracy during explicit time-integration. Krieg and Key (1973). The explicit time-integration scheme based on the Newmark  $\beta$ -method with  $\beta = 0$  and  $\gamma = 0.5$  (Belytschko et al., 1976) is employed to integrate (16).

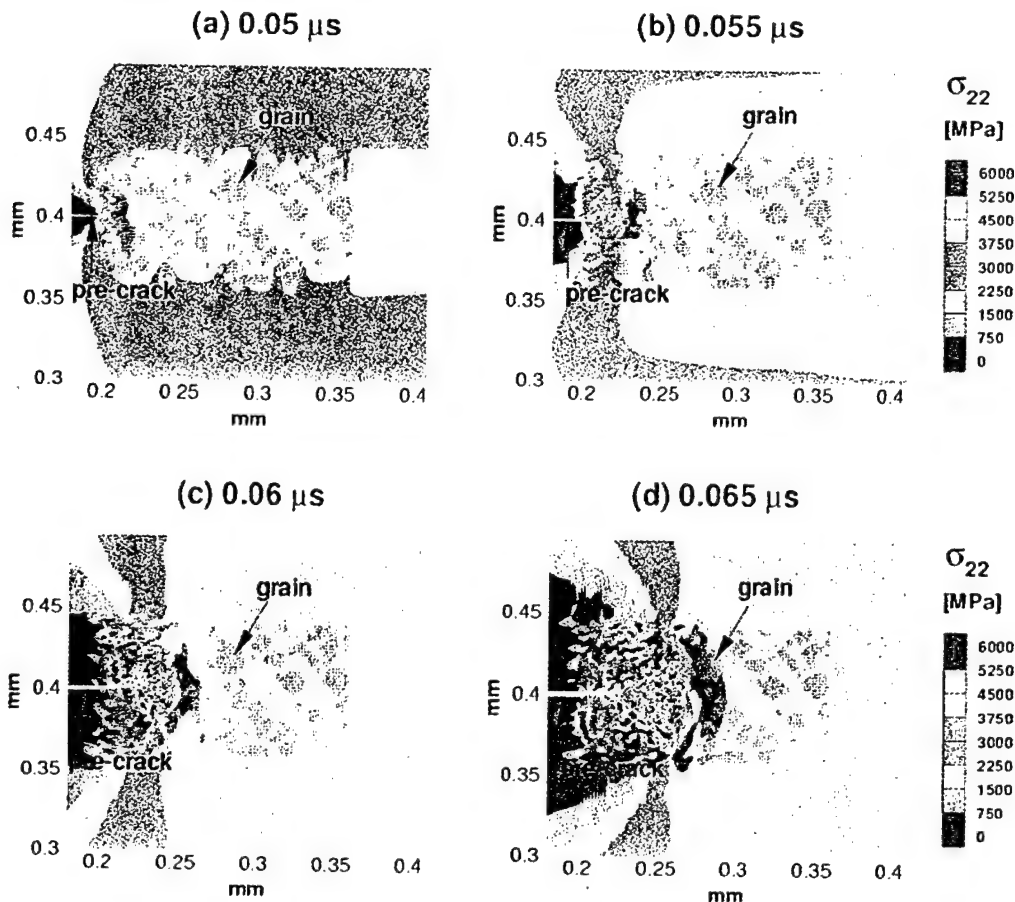


Figure 6. Distributions of  $\sigma_{22}$  at four different times for a specimen with microstructure in Figure 4(a) and a strong interfacial bonding between the grains and the matrix.  $V_0 = 50$  m/s.

## 5. Results

For comparison purposes, a calculation is first carried out for a specimen made of pure  $\text{Al}_2\text{O}_3$  matrix without reinforcement. The material for the whole specimen has the bulk and cohesive surface properties for  $\text{Al}_2\text{O}_3$  listed in Tables 1 and 2. This calculation has an applied boundary velocity of  $V_0 = 50$  m/s. The distributions of the vertical component of the Cauchy stress  $\sigma_{22}$  at four different times are shown in Figure 5. The location of the tip of the initial crack is at 0.2 mm in the horizontal direction. Crack propagation initiates at approximately  $0.065 \mu\text{s}$  after the beginning of loading. The crack first propagates horizontally briefly and then divides into two propagating branches which are oriented at approximately  $\pm 45^\circ$  from the initial direction of propagation. This behavior has been described by Xu and Needleman (1994). The average crack speed in this case is 3200 m/s for the period shown. Note that the Rayleigh wave speed in this material is 5379 m/s.

The results of two calculations using the base microstructure in Figure 4(a) are shown in Figures 6 and 7. These two sets of results are obtained for the same loading condition of  $V_0 = 50$  m/s, the same that as in Figure 5. In Figure 6, the interfaces between the grains and the matrix are assumed to have a strong bonding, as characterized by a maximum normal stress of  $\sigma_{\max} = 34$  GPa and a maximum shear stress of  $\tau_{\max} = 78.2$  GPa. These values correspond to a

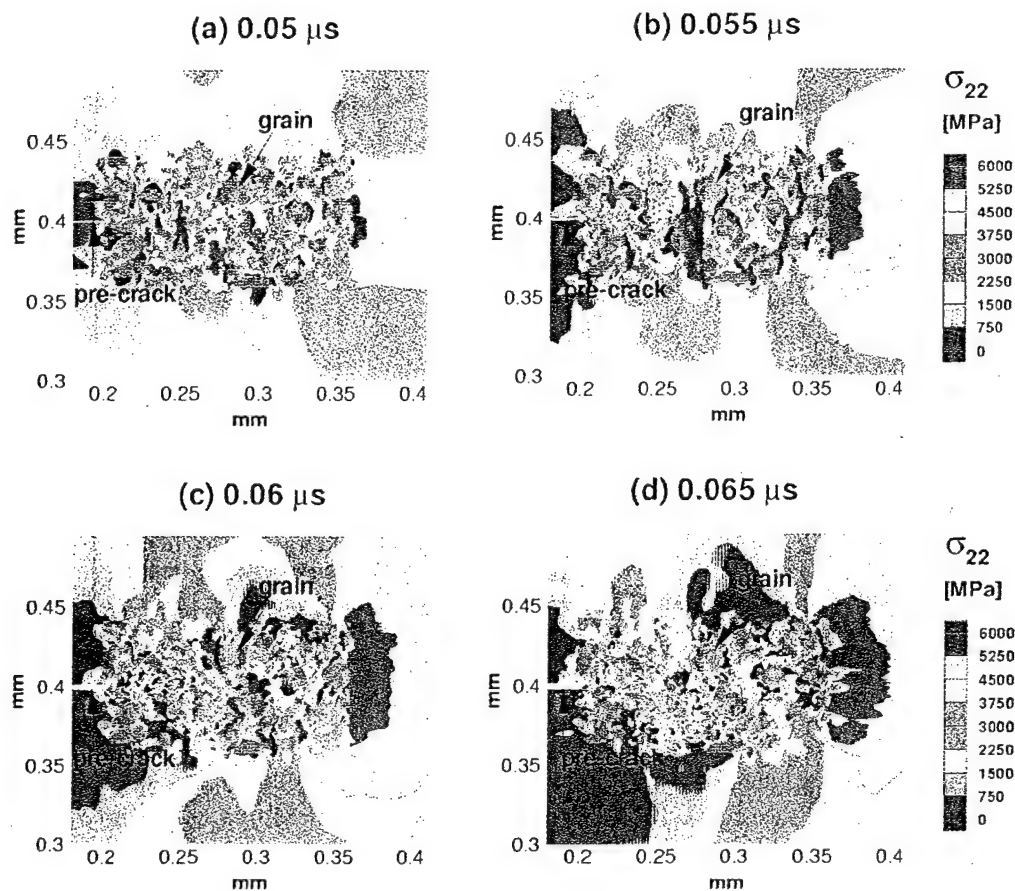


Figure 7. Distributions of  $\sigma_{22}$  at four different times for a specimen with microstructure in Figure 4(a) and a weak interfacial bonding between the grains and the matrix.  $V_0 = 50$  m/s.

work of separation of  $\phi_0 = 92.4$  J/m<sup>2</sup>. In Figure 7, the interfaces between the two constituent phases are assumed to have a weak bonding with  $\sigma_{\max} = 1.7$  GPa,  $\tau_{\max} = 3.91$  GPa and  $\phi_0 = 4.6$  J/m<sup>2</sup>.

Figure 6 shows that when strong interfacial strength is assumed fracture occurs through the extension of the pre-existing crack. The crack propagation exhibits a zigzag pattern because of the material inhomogeneities. The crack eventually splits into two branches, in a way similar to what is seen in Figure 5 for fracture in uniform Al<sub>2</sub>O<sub>3</sub>. However, the crack extension before branching is longer than that in Figure 5. The crack propagation occurs mainly in the matrix and along grain-matrix interfaces, with occasional fracture of grains. In Figure 7, the mode of failure is initiation, growth and coalescence of microcracks. Clearly, the relatively weak interfacial bonding allows microcracks to initiate at multiple interfacial sites upon tensile loading. This process can occur independently of the main pre-crack. Coalesced microcracks eventually link up with the main crack, resulting in the failure of the material.

The evolutions of the crack lengths for the three cases discussed so far are compared in Figure 8. The curves represent the histories of the cumulative length of cracks/microcracks in each constituent or along the phase boundaries, regardless of the number of segments involved. The history of combined total crack length in all fracture sites is also shown. The cumulative

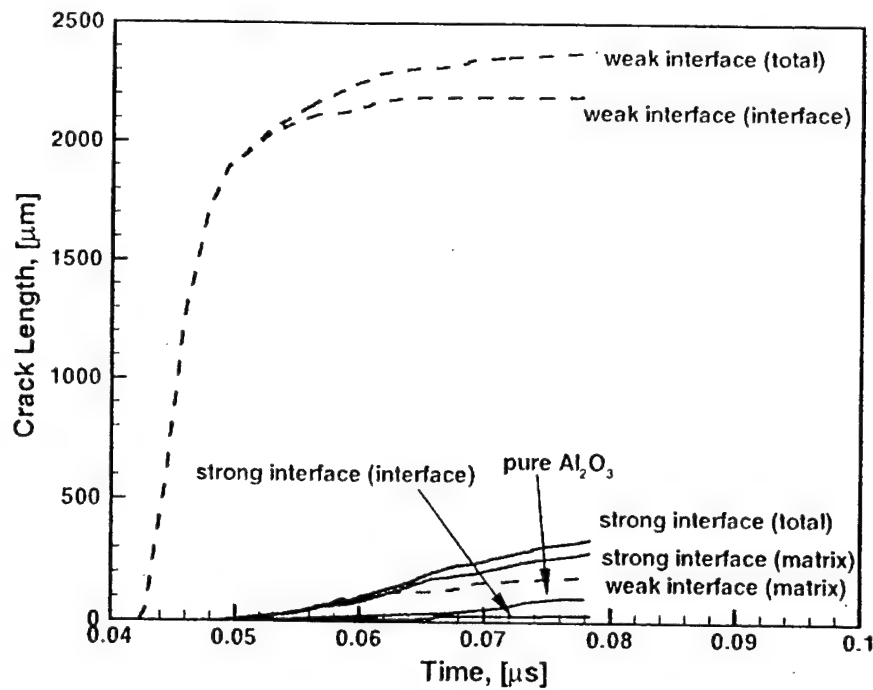


Figure 8. A comparison of crack length histories for the cases in Figures 5-7.

crack length in the grains is quite small and is, therefore, not plotted. The specimen made of pure  $\text{Al}_2\text{O}_3$  shows the smallest crack length at all stages of deformation. Clearly, material inhomogeneities allowed significantly more crack surfaces to be generated under the same remote deformation. The total amount of crack surface area generated in Figure 6 with the strong interfacial bonding is approximately three times ( $\sim 300 \mu\text{m}$  at  $0.08 \mu\text{s}$ ) that in Figure 5 ( $\sim 100 \mu\text{m}$  at  $0.08 \mu\text{s}$ ). The total crack surface area for the weak interface in Figure 7 is 24 times ( $\sim 2400 \mu\text{m}$  at  $0.08 \mu\text{s}$ ) that in Figure 5. There is a difference in the distributions of fracture sites in the two cases as well. In Figure 6, the strong interfaces cause cracks to propagate predominantly in the matrix. While in Figure 7, the weak interphase bonding allows microcracks to form mainly through grain-matrix interfacial debonding. The results here are consistent with experimental observations that materials with strong interphase bonding show transgranular fracture and materials with weak interphase bonding show intergranular fracture. Logan (1996).

The work of separation for the weak interface is only 1/20 that for the strong interface (see Table 2), corresponding to significantly less energy consumption per unit crack surface area generated. However, the higher amount of crack surface seen in Figure 8 more than compensates for this lower energy value per unit area. Figure 9 shows the evolutions of the strain energy stored in the specimen materials, the kinetic energy in the specimen and the cohesive energy or surface energy along cracks generated. It can be seen that the rate of energy dissipation through crack surface generation is actually higher initially for weak interfaces. This is due to the simultaneous occurrence of microcracks in multiple locations. Consequently, more energy is delivered into the crack surfaces during this time period than in the case of strong interfaces. As crack growth continues, the cohesive energy ( $\Phi$ ) for the strong interface material eventually exceeds that for the weak interface case. The mode of failure through microcracks also corresponds to less strain energy ( $W$ ) in the specimen and a higher

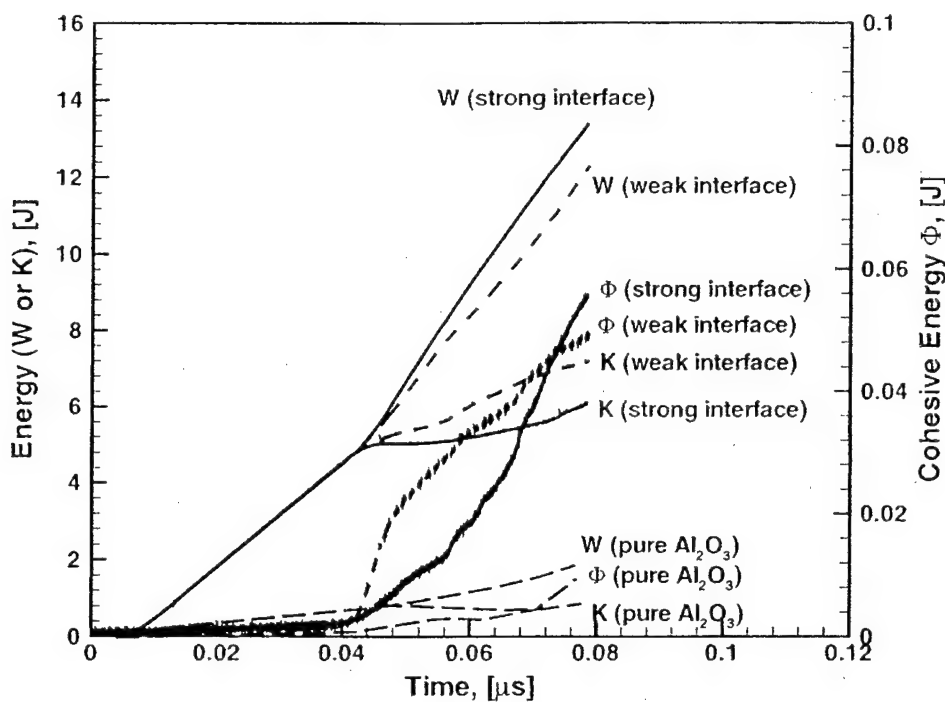


Figure 9. A comparison of energy evolutions for the cases in Figures 5-7.

amount of kinetic energy ( $\mathcal{K}$ ) in the bulk material. The effect of  $\text{TiB}_2$  reinforcements on the energies is clearly significant regardless of the interfacial strength. Without the reinforcements or grains, all energies are only small fractions of the values for the cases with reinforcements. For example, the cohesive surface energy ( $\Phi$ ) for the pure matrix material is only  $\frac{1}{5}$  of those for the composites, see Figure 9.

The distributions of  $\sigma_{22}$  at four different times for two calculations using the microstructures in Figure 4(b, c) are shown in Figures 10 and 11, respectively. Here, the same strong interphase bonding strength as that in Figure 6 is assumed. It can be seen that reducing the grain volume fraction and reducing the grain size while keeping the grain volume fraction constant have similar effects of facilitating the propagation of the pre-crack and expediting its subsequent branching into multiple cracks. The smaller number of grains and the smaller size of grains pose less impediment to the propagation of cracks. Indeed, the results in these figures look closer to the results in Figure 5 than to the results in Figure 7.

The crack length histories for Figures 6, 10 and 11 are shown in Figure 12. These curves allow the effects of the different microstructures in Figure 4 to be compared quantitatively. Consistent with what is seen in Figures 10 and 11, the lower grain volume fraction for microstructure *B* and smaller grain size for microstructure *C* both cause the crack length in the matrix to increase. The result is higher overall crack lengths for microstructures *B* and *C*. These variations in microstructure do not seem to show a clear influence on the amount of interfacial crack or microcrack growth under the conditions analyzed. The corresponding energy evolutions for the three cases are shown in Figure 13. As a result of the increases in the matrix crack lengths, microstructures *B* and *C* have slightly higher cohesive energy levels than microstructure *A*. These results suggest that the variation of cohesive energy with grain

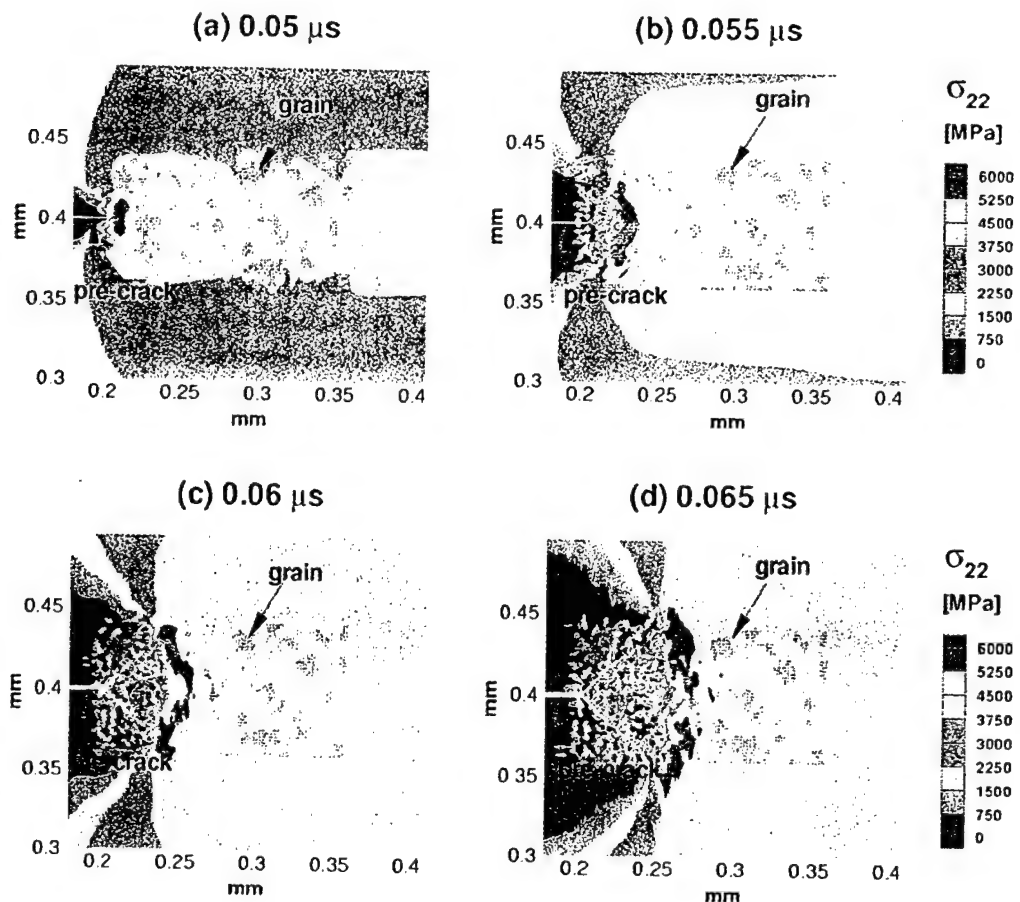


Figure 10. Distributions of  $\sigma_{22}$  at four different times for a specimen with microstructure in Figure 4(b) and a strong interfacial bonding between the grains and the matrix.  $V_0 = 50$  m/s.

size or grain volume fraction may not be monotonic. Rather, phase distributions and phase morphologies may have an impact. This effect has been analyzed in Zhai and Zhou (1998).

## 6. Discussion and conclusions

A micromechanical framework of analysis has been developed and used to provide explicit incorporation of arbitrary material microstructures and to resolve arbitrary, unconstrained fracture patterns in heterogeneous, brittle solids. The approach combines descriptions of bulk constituent response and fracture surface cohesion, as originally used by Xu and Needleman (1994). This approach is especially appropriate for analyzing microscopic failure and fracture over a range of length scales because material separation is a natural outcome of constitutive behavior, microstructure and loading in this model. The formulation is free from failure criteria valid over only certain length scales, e.g., continuum criteria based on the existence of  $K$ -fields.

The dynamic failure behavior in a class of  $\text{Al}_2\text{O}_3/\text{TiB}_2$  composites is simulated under the context of a centered-cracked specimen and the conditions of plane strain. In this analysis, both the bulk and interfacial constitutive laws are hyperelastic. The results demonstrated the effects of microstructure on dynamic failure in the materials. The bonding strength between

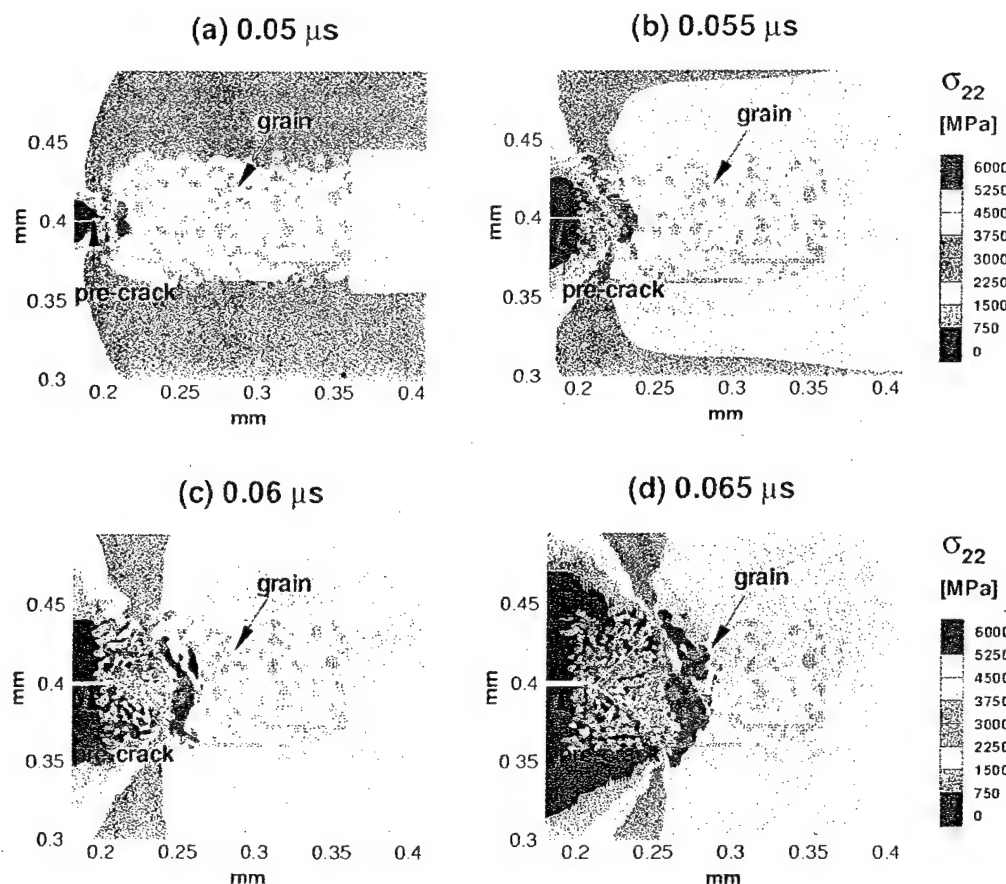


Figure 11. Distributions of  $\sigma_{22}$  at four different times for a specimen with microstructure in Figure 4(c) and a strong interfacial bonding between the grains and the matrix.  $V_0 = 50$  m/s.

the alumina matrix and the titanium diboride reinforcements, which is a function of conditions during hot-pressing of the composites, is found to significantly influence the failure modes in the composites. When strong bonding exists, the mode of failure is the extension of cracks and crack branching. When weak bonding exists, the mode of failure is microcrack growth and coalescence. The framework of analysis also allows the evolution of crack lengths and the evolution of energies to be tracked. Calculations have shown that under the same overall remote deformation microscopic  $\text{TiB}_2$  reinforcements significantly increase the total cohesive energy consumed in the generation of crack and microcrack surfaces.

### Acknowledgement

Support from the U.S. Army Research Office through grant DAAG55-98-1-0454 is gratefully acknowledged. Calculations reported are carried out on the Cray Computers at the San Diego Supercomputer Center, Jet Propulsion Laboratory and the Goddard Space Center. M.Z. would like to thank Prof. A. Needleman and Dr. X.-P. Xu for helpful discussions. Thanks are extended to Dr. K.V. Logan for providing micrographs of  $\text{Al}_2\text{O}_3/\text{TiB}_2$  composites used in this research.

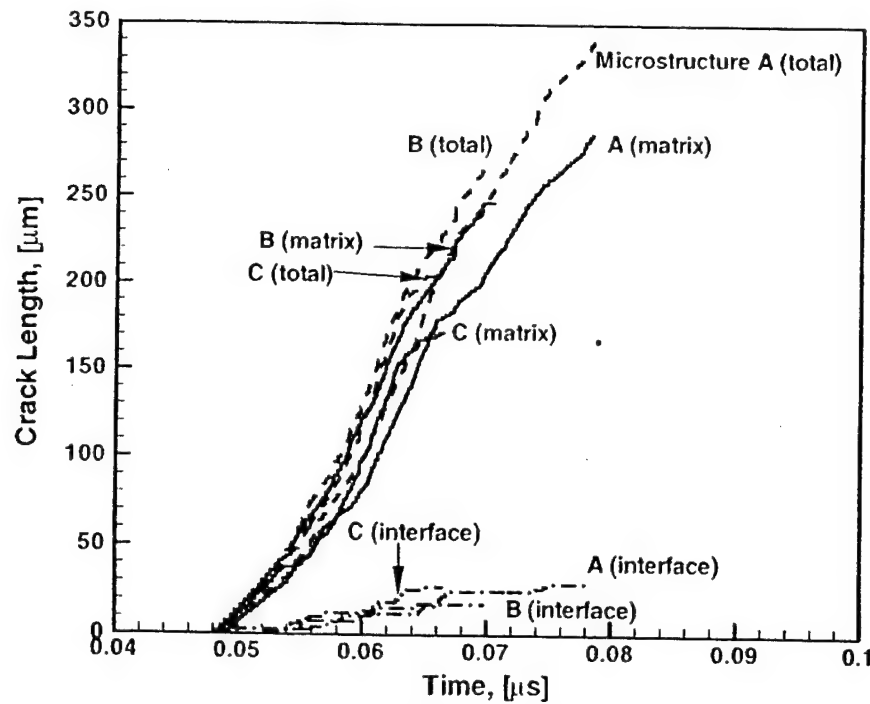


Figure 12. A comparison of crack length histories for the three different microstructures in Figure 4.

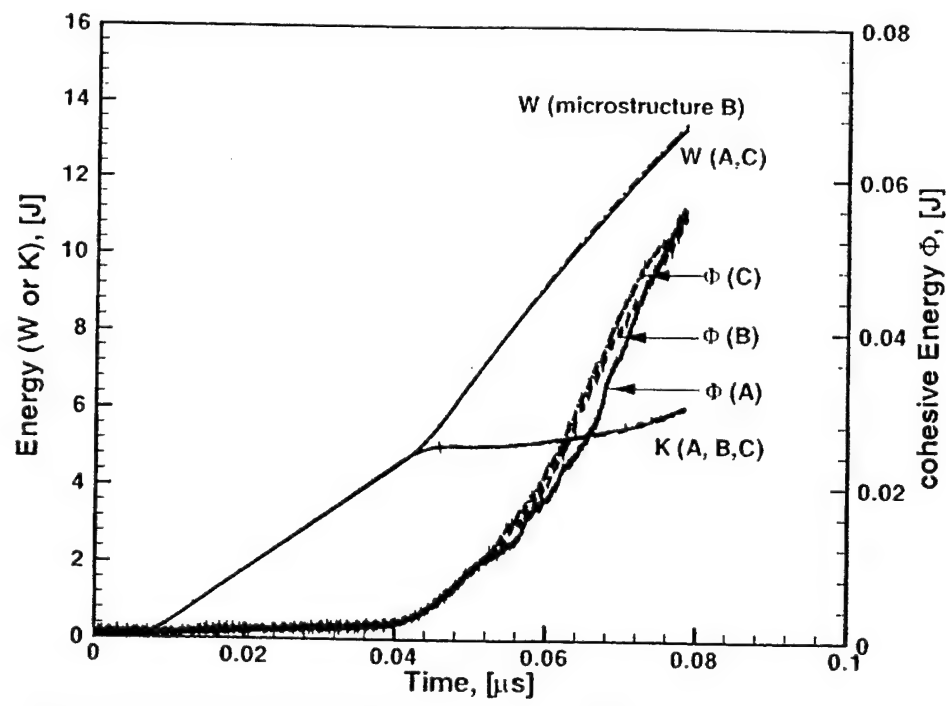


Figure 13. A comparison of energy evolutions for the three different microstructures in Figure 4.

## References

Ahrens, T.J. and Rubin, A.M. (1983). Impact-induced tensional failure in rock. *Journal of Geophysics Research* **98**, 1185-1203.

Barrenblatt, G.I. (1962). The mathematical theory of equilibrium of cracks in brittle fracture. *Advanced Applied Mechanics* **7**, 55-192.

Batra, R.C. (1998). Linear constitutive relations in isotropic finite elasticity. *Journal of Elasticity* **52**(1), 75-90.

Belytschko, T., Chiapetta, R.L. and Bartel, H.D. (1976). Efficient large scale non-linear transient analysis by finite elements. *International Journal of Numerical Methods in Engineering* **10**, 579-596.

Brockenbrough, J.R., Suresh, S. and Duffy, J. (1988). An analysis of dynamic fracture in microcracking solids. *Philosophical Magazine A* **58**, 619-634.

Camacho, G.T. and Ortiz, M. (1996). Computational modeling of impact damage in brittle materials. *International Journal of Solids and Structures* **33**(20-22), 2899-2983.

Curran, D.R., Seaman, L., Cooper, T. and Shockley, D.A. (1993). Micromechanical model for continuum and granular flow of brittle materials under high strain rate application to penetration of ceramic targets. *International Journal of Impact Engineering* **13**, 53-58.

Curran, D.R., Seaman, L. and Shockley, D.A. (1987). Dynamic failure of solids. *Physics Reports* **147**, 253-388.

Curtin, W. (1991). Theory of mechanical properties of ceramic-matrix composites. *Journal of the American Ceramic Society* **74**, 2837-2845.

Dugdale, D.S. (1960). Yielding of steel sheets containing slits. *Journal of Mechanics and Physics of Solids* **8**, 100-104.

Espinosa, H.D., Raiser, G., Clifton, R.J. and Ortiz, M. (1992). Experimental observation and numerical modeling of inelasticity in dynamic loaded ceramics. *Journal of Hard Materials* **3**, 285-313.

Espinosa, H.D. and Brar, N.S. (1995). Dynamic failure mechanisms of ceramic bars: Experiments and numerical simulations. *Journal of Mechanics and Physics of Solids* **43**, 1615-1638.

Evans, A.G. (1991). The mechanical properties of reinforced ceramic, metal and intermetallic matrix composites. *Materials Science and Engineering A* **143**, 63-76.

Gao, H.J. and Klein, P. (1997). Numerical simulation of crack growth in an isotropic solid with randomized cohesive bonds. *Journal of Mechanics and Physics of Solids* (to appear).

Grady, D.E. and Kipp, M.E. (1979). The micromechanics of impact fracture of rock. *International Journal of Rock Mechanics* **16**, 293-302.

Johnson, G.R. and Holmquist, T.J. (1992). A computational constitutive model for brittle materials subjected to large strains, high rates, and high pressure. *Shock Wave and High Strain Rate Phenomena in Materials* (Edited by Meyers, M.A., Murr, L.E. and Staudhammer, K.P.), 1075-1081.

Jones, D.W. (1996). Ceramic biomaterials. *Key Engineering Materials* **122-124**, 345-384.

Kishi, T., Takeda, N. and Kim, B.N. (1990). Dynamic fracture toughness and microstructural fracture mechanisms in ceramics. *Ceramic Engineering of Science Process* **11**(7-8), 650-664.

Kishi, T. (1991). Dynamic fracture toughness in ceramic and ceramics matrix composites. *Engineering Fracture Mechanics* **40**, 785-790.

Kobayashi, A.S. (1991). Dynamic fracture of ceramics and ceramic composites. *Materials Science and Engineering A* **143**, 111-117.

Komanduri, R. (1989). Advanced ceramic tool materials for machining. *International Journal of Refraction Hardening Metals* **8**, 125-132.

Krieg, R.D. and Key, S.W. (1973). Transient shell response by numerical time integration. *International Journal of Numerical Methods in Engineering* **7**, 273-286.

Lange, F.F. (1979). Fracture toughness of  $\text{Si}_3\text{N}_4$  as function of initial  $\alpha$ -phase content. *Journal of the American Ceramic Society* **62**, 428.

Lankford, J. (1989). Dynamic compressive fracture in fiber-reinforced ceramic matrix composites. *Material Science and Engineering A: Structural Materials: Properties, Microstructure and Processing A* **107**, 261-268.

Lankford, J. (1994). Effect of hydrostatic pressure and loading rate on compressive failure of fiber-reinforced ceramic-matrix composites. *Composite Science Technology* **51**, 537-543.

Lehman, R.L. (1989). Ceramic matrix fiber composites. *Treatise Material Science Technology* **29**, 229-191.

Logan, K.V. (1996). *Composite Ceramics, Final Technical Report*. USSTACOM DAAE07-95-C-R040.

Longy, F. and Cagnoux, J. (1989). Plasticity and microcracking in shock-loaded alumina. *Journal of the American Ceramic Society* **72**, 971-979.

Matsui, M. and Masuda, M. (1994). Fracture behavior of silicon nitride at elevated temperatures. *Tailoring of Mechanical Properties of Si<sub>3</sub>N<sub>4</sub> Ceramic* (Edited by M.J. Hoffmann and G. Petzow). Kluwer Academic Publishers, Dordrecht, Netherlands. 403-414.

Messer, P.F. (1991). The strength of dental ceramics. *Journal of Density* **18**, 227-235.

Niihara, K. and Nakahira, A. (1990). Particulate strengthened oxide nanocomposites. *Advanced Structural Inorganic Composites* (Edited by P. Vincenzini). Elsevier publishers. 637-664.

Niihara, K. (1991). New design concepts of structural ceramics-ceramic nanocomposites. the centennial issue of the ceramic society of Japan. *Journal of Ceramic Society of Japan* **99**(10), 974-982.

Niihara, K., Nakahira, A. and Sekino, T. (1993). New nanocomposite structural ceramics. *Material Reserves Society of Symplectic Procedures* **286**, 405-412.

Ortiz, M. (1996). Computational micromechanics. *Computational Mechanics* **18**, 321-338.

Rajendran, A.M. (1994). Modeling the impact behavior of AD85, ceramic under multiaxial loading. *International Journal of Impact Engineering* **15**, 749-768.

Ravichandran, G. and Subhash, G. (1995). A micromechanical model for high strain rate behavior of ceramics. *International Journal of Solids and Structures* **32**, 2627-2646.

Seaman, L., Curran, D.R. and Murri, W.J. (1985). A continuum model for dynamic tensile microstructure and fragmentation. *Journal of Applied Mechanics*, **52**, 593-600.

Shockley, D.A., Curran, D.R., Seaman, L., Rosenberg, J.T. and Peterson, S.F. (1974). Fragmentation of rock under dynamic loads. *International Journal of Rock Mechanics* **11**, 303-317.

Shockley, D.A., Machand, A.H., Skaggs, S.R., Cort, G.E., Burkett, M.W. and Parker, R. (1990). Failure phenomenology of confined ceramic targets and impact rods. *International Journal of Impact Engineering* **9**, 263-275.

Shockley, D.A., Seaman, L. and Curran, D.R. (1985). The micro-statistical fracture mechanics approach to dynamic fracture problems. *International Journal of Fracture* **27**, 145-157.

Suresh, S., Nakamura, T., Yeshurun, Y., Yang, K. H. and Duffy, J. (1990). Tensile fracture toughness of ceramic materials: Effects of dynamic loading and elevated temperatures. *Journal of the American Ceramic Society* **73**, 2457-2466.

Vekinis, G., Ashby, M.F., Shercliff, H. and Beaumont, P.W. (1993). The micromechanisms of fracture of alumina and ceramic-based fiber composite: Modelling the failure processes. *Composites Science and Technology* **48**, 325-330.

Walter, J. (1992). *Material Modeling for Terminal Ballistic Simulation*. Tech. Report. US Army Research Lab., Maryland.

Willmann, G. (1996a). Development in medical-grade alumina during the past two decades. *Journal of Material Processing Technology* **56**, 168-176.

Willmann, G. (1996b). Clinical failure of alumina. *Journal of Arthroplasty* **10**, 855-859.

Woodward, R.L., Gooch, W.A., O'Donnell, R.G., Oerciballi, W.J., Baxter, B.J. and Oattie, S.D. (1994). A study of fragmentation in the ballistic impact of ceramics. *International Journal of Impact Engineering* **15**, 605-618.

Xu, X.-P. and Needleman, A. (1994). Numerical simulations of fast crack growth in brittle solids. *Journal of Mechanics and Physics of Solids* **42**, 1397-1434.

Xu, X.-P., Needleman, A. and Abraham, F.F. (1997). Effect of inhomogeneities on dynamic crack growth in an elastic solid. *Modeling and Simulation Material's Science and Engineering* **5**, 489-516.

Yang, Kwan-Ho, Kobayashi, A.S. (1990). Dynamic fracture response of alumina and two ceramic composites. *Journal of the American Ceramic Society* **73**(8), 2309-2315.

Zeng, J., Tanaka, I., Miyamoto, Y., Yamada, O. and Niihara, K. (1992). Sintering behaviors of Si<sub>3</sub>N<sub>4</sub>-silica ceramics during hot isostatic pressing. *Journal of the American Ceramic Society* **75**(1), 148-152.

Zhai, J. and Zhou, M. (1998). Micromechanical modeling of dynamic crack growth in ceramic composites. *Mixed Mode Crack Behavior* (Edited by K. Miller and D.L. McDowell). ASTM STP 1359, 174-202.

Zhao, J., Stearns, L.C., Harmer, M.P., Chan, H.M. and Miller, G.A. (1993). Mechanical behavior of alumina-silicon carbide nanocomposites. *Journal of the American Ceramic Society* **76**(2), 503-510.

Zhou, S.J. and Curtin, W.A. (1995). Failure of fiber composites: A lattice green function model. *Acta Metallurgica et Materialia* **43**, 3093-3104.

## EXPERIMENTAL CHARACTERIZATION OF THE DYNAMIC FAILURE RESISTANCE OF $\text{TiB}_2/\text{Al}_2\text{O}_3$ COMPOSITES

A. R. Keller and M. Zhou<sup>†</sup>

*The George Woodruff School of Mechanical Engineering  
Georgia Institute of Technology, Atlanta, GA 30332-0405*

**Abstract:** The dynamic compressive strength and microscopic failure behavior of  $\text{TiB}_2/\text{Al}_2\text{O}_3$  ceramic composites with a range of microstructural morphologies and size scales are analyzed. A split Hopkinson pressure bar is used to achieve loading rates of the order of  $400 \text{ s}^{-1}$ . The dynamic compressive strength of the materials is found to be between 4.3 and 5.3 GPa, indicating a strong dependence of strength on microstructure. Microstructures with finer phases as measured by linear intercept length (LIL) have higher strength levels. The dynamic strength levels are approximately 27% higher than the values of 3-4 GPa measured at quasi-static loading rates for these materials. These strength levels are also higher than the strength levels of monolithic  $\text{TiB}_2$  and  $\text{Al}_2\text{O}_3$  under similar dynamic conditions. Scanning electron microscopy (SEM) and energy dispersive spectrometry indicate that failure associated with the  $\text{Al}_2\text{O}_3$  phase is transgranular cleavage in all microstructures and failure associated with the  $\text{TiB}_2$  phase is a combination of transgranular cleavage and intergranular debonding and varies with the microstructures. The measured compressive strength of the materials directly correlates with the fraction of  $\text{TiB}_2$ -rich areas on fracture surfaces.

### INTRODUCTION

One method to reduce brittleness and enhance failure resistance of ceramics is the development of ceramic composites (Niihara et al., 1991). Significant influence of microstructural effects on properties has been reported. For example, Niihara et al. (1991) reported that a 5% population of  $\text{SiC}$  nanoparticles increases the tensile strength of  $\text{Si}_3\text{N}_4$  from 350 MPa to 1 GPa and improves its fracture toughness from  $3.25 \text{ MPa}\sqrt{\text{m}}$  to  $4.7 \text{ MPa}\sqrt{\text{m}}$ . Although microstructure-induced, size-dependent toughening mechanisms at the micro and nano levels are demonstrated approaches for property enhancement, so far such effects have not been well quantified. In order to develop more advanced materials, it is necessary to characterize the influences of phase morphology, phase length scale, and interfacial behavior on fracture toughness. Recently, two-phase ceramics of titanium diboride/alumina ( $\text{TiB}_2/\text{Al}_2\text{O}_3$ ) with a range of phase sizes and phase morphologies

have been developed (Logan, 1992a,b). These materials have shown a wide range of fracture toughness values and some of the values are higher than those of both constituents produced separately in bulk. These materials provide an opportunity to study the correlation between microstructure and mechanical behavior.

In many applications, intensive dynamic loading occurs under normal operating conditions. Examples include particle impact on ceramic turbine blades (Bilek & Helesic, 1990), contact of a high speed cutting tools with workpiece (Komanduri, 1989), and impact of ballistic projectiles with ceramic armor (Anderson & Morris, 1991). The dynamic behavior of materials can be dramatically influenced by microstructural characteristics, including phase size, phase morphology, composition and texture (Viechnicki et al., 1991). Thus, it is crucial to develop intrinsic relationships between fabrication,

<sup>†</sup> To whom all correspondence should be addressed, 404-894-3294, min.zhou@me.gatech.edu.

resulting microstructure, and dynamic properties in order to tailor ceramic systems to the needs of applications (Bilek & Helesic, 1990). In order to establish the relationships, varying processing approaches have been used to produce two-phase  $\text{TiB}_2/\text{Al}_2\text{O}_3$  ceramics with four different biased microstructures. These microstructures are analyzed in this research.

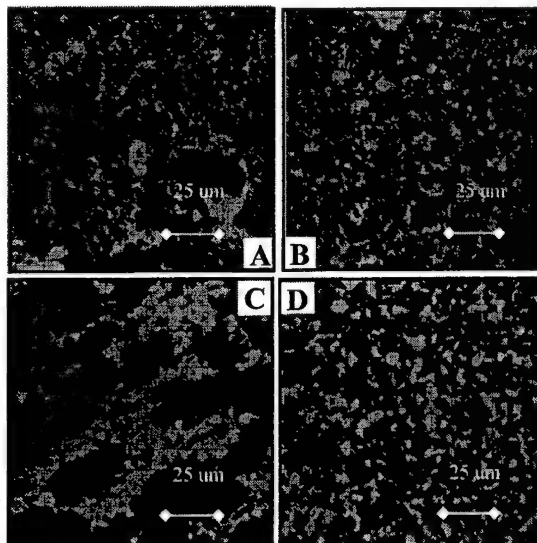


Fig. 1 Microstructures of Materials Analyzed ( $\text{TiB}_2$  white,  $\text{Al}_2\text{O}_3$  dark)

#### MATERIALS

The materials are produced through self-propagating high temperature synthesis and mechanical mixing of powders followed by hot pressing (Logan 1992b; Carney 1997). Each material has a nominal composition of 70%  $\text{Al}_2\text{O}_3$  and 30%  $\text{TiB}_2$  by weight. Figure 1 shows the microstructures of the four  $\text{Al}_2\text{O}_3/\text{TiB}_2$  composites analyzed. The light areas consist of  $\text{TiB}_2$  and the dark areas are  $\text{Al}_2\text{O}_3$ . The microstructures vary in phase distribution and length scales. This microstructure shows intertwining of alumina and titanium diboride. The microstructure is unique in that its complicated morphology precludes the identification of simple crack paths through each phase or along phase interfaces. The microstructure in Fig. 1(b) consists of particles of  $\text{TiB}_2$  embedded in an  $\text{Al}_2\text{O}_3$  matrix. The microstructure in Fig. 1(c) consists of isolated  $\text{Al}_2\text{O}_3$

matrix islands surrounded by a network of  $\text{TiB}_2$  reinforcement. The isolated matrix areas are approximately  $20 \times 100 \mu\text{m}$  in size. A dispersion of small  $\text{Al}_2\text{O}_3$  particles nanometers in size are scattered in the  $\text{TiB}_2$  phase. Clearly, two length scales are operative in this microstructure, influencing its strength and fracture toughness. The microstructure in Fig. 1(d) is similar to that in Fig. 1(b) except for significantly larger  $\text{TiB}_2$  particle sizes. The average  $\text{TiB}_2$  particle size is  $5-10 \mu\text{m}$  in Fig. 1(d) and at least one or two orders of magnitude smaller in Fig. 1(b). The smallest particles in Fig. 1(b) are of submicron or nanometer sizes. To quantify the different phase morphologies and sizes, the linear intercept length (LIL) for the two phases are measured on digital images of the microstructures. In the analysis here, the average LIL is used as a measure of phase size.

#### EXPERIMENTS

In order to characterize the response of the materials to dynamic compressive loading, a split Hopkinson pressure bar apparatus is used. Soft recovery of specimens is achieved through the use of a momentum trapping technique developed by Nemat-Nasser et al. (1991). This mechanism allows specimens to be recovered after loading under a single stress pulse, eliminating any unintended reloading. The specimen fragments were collected for postmortem characterization of microscopic failure.

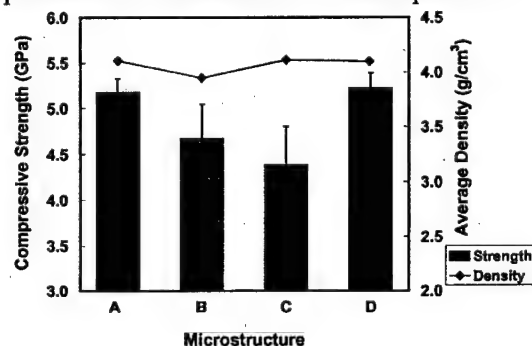


Fig. 2 Compressive Strength and Density

#### COMPRESSIVE STRENGTH

The measured strengths of the materials and their densities are summarized in Fig. 2. The correlation between the strength and the linear intercept length is shown in Fig. 3. Microstructures A and D show significantly higher strengths than microstructures B

and C. Since material B has a much higher level of porosity than the other materials, attention is given only to materials A, C, and D. Higher strengths coincide with smaller LIL. This can be phenomenologically explained. Microstructures with smaller LIL values present a more heterogeneous media for propagating cracks, inducing more tortuous cracks paths and, therefore, increasing energy dissipation for crack growth. The micromechanical quantification of the fracture resistance of the four microstructures accounts for the actual phase distributions and arbitrary fracture patterns.

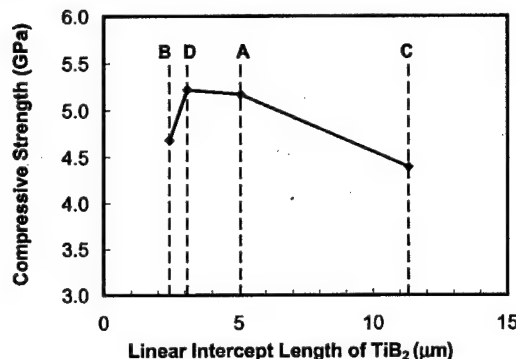


Fig. 3 Correlation between Strength and Linear Intercept Length

#### FRACTOGRAPHY

Coinciding energy dispersive spectrometry maps showing the distributions of  $\text{Al}_2\text{O}_3$ -rich and  $\text{TiB}_2$ -rich areas on fracture surfaces are taken and shown in Fig. 4. The use of these phase maps and fractographs greatly facilitates the identification of phases on fracture surfaces and the intergranular or intragranular nature of the fracture process. The failure process in Microstructure A shows large regions of  $\text{Al}_2\text{O}_3$  surrounded by a continuous network of  $\text{TiB}_2$ . The  $\text{Al}_2\text{O}_3$  areas are smooth, indicating transgranular cleavage inside  $\text{Al}_2\text{O}_3$  grains. Failure involving the  $\text{TiB}_2$  phase appears to be primarily intergranular pullout. The overall failure is a combination of transgranular cleavage inside  $\text{Al}_2\text{O}_3$  and intergranular separation along  $\text{Al}_2\text{O}_3/\text{TiB}_2$  boundaries. Approximately 74% of the fracture surfaces is cleavage planes within the  $\text{Al}_2\text{O}_3$  and 26% are associated with the  $\text{TiB}_2$ . Note that the volume fraction of  $\text{Al}_2\text{O}_3$  in this material is 72.6%. The fracture surfaces for microstructure B are dominated by small regions of transgranular cleavage of the

$\text{Al}_2\text{O}_3$  phase. Failure involving the  $\text{TiB}_2$  phase occurred primarily by intergranular pullout.  $\text{TiB}_2$  particles are relatively evenly distributed on the fracture surfaces, suggest a fracture process which is not significantly affected by the presence of the particles. Also, numerous pores were observed in the  $\text{Al}_2\text{O}_3$  phase, consistent with the measured low density (95% of theoretical value) of this material. Clearly, excessive porosity is detrimental to the resistance to crack propagation in this material. Approximately 84% of the fracture surfaces is  $\text{Al}_2\text{O}_3$ -rich, significantly higher than the 72.6% volume fraction of  $\text{Al}_2\text{O}_3$  in this material. Thus, the occurrence of fracture is predominantly in the  $\text{Al}_2\text{O}_3$  phase. Since  $\text{Al}_2\text{O}_3$  has a lower strength and lower fracture energy compared with  $\text{TiB}_2$ , this higher ratio of fracture surfaces in  $\text{Al}_2\text{O}_3$  appears to be the primary reason for the observed low strength reported earlier. A primarily transgranular mode of fracture inside  $\text{Al}_2\text{O}_3$  is also observed for microstructure C. Fracture surfaces are dominated by large areas of cleavage within the  $\text{Al}_2\text{O}_3$  phase. However, failure involving the  $\text{TiB}_2$  phase occurred through a combination of transgranular cleavage and intergranular pullout. Most parts of the fracture surfaces associated with the  $\text{TiB}_2$  show transgranular cleavage. The fracture surface characteristics reflect the morphology of this microstructure—large areas of cleavage in  $\text{Al}_2\text{O}_3$  surrounded by a continuous network of  $\text{TiB}_2$ . The fact that cleavage in  $\text{Al}_2\text{O}_3$  occurs over multiple grains contributes to its lower failure resistance, due to the fact that the effectiveness of the  $\text{TiB}_2$  as a reinforcing phase is decreased. Approximately 77% of the fracture surfaces is  $\text{Al}_2\text{O}_3$ -rich, higher than the 72.6% volume fraction of  $\text{Al}_2\text{O}_3$  in the material. Thus, there appears to be a slight preference for failure to occur in the  $\text{Al}_2\text{O}_3$  phase. The failure in microstructure D is unique in that transgranular cleavage is the primary fracture mechanism for both  $\text{Al}_2\text{O}_3$  and  $\text{TiB}_2$ . Although failure involving the  $\text{TiB}_2$  phase occurred through a combination of transgranular cleavage and intergranular pullout, the dominant mechanism is cleavage. This is in sharp contrast to what is observed for the other microstructures. Evenly distributed  $\text{TiB}_2$  particles across the fracture surfaces echo the microstructural morphology of fine particles embedded in an  $\text{Al}_2\text{O}_3$  matrix. It also appears that the homogeneous distribution of  $\text{TiB}_2$  reinforcement inhibits intergranular separation, thus forcing cracks

to go through the stronger  $TiB_2$  phase and enhancing failure resistance. The rough and ragged nature of the surface is in contrast to the relatively smooth appearance of the surfaces for microstructures A, B, and, most prominently, C. Approximately 71% of the fracture surfaces is  $Al_2O_3$ -rich, lower than the 72.6% volume fraction of  $Al_2O_3$  in this material. Note that this is the only microstructure that shows a  $TiB_2$ -rich fracture surface fraction higher than its corresponding volume fraction in the material. This bias toward the  $TiB_2$  points to an unusual shift of failure into the stronger phase and can be associated with significantly higher strength.

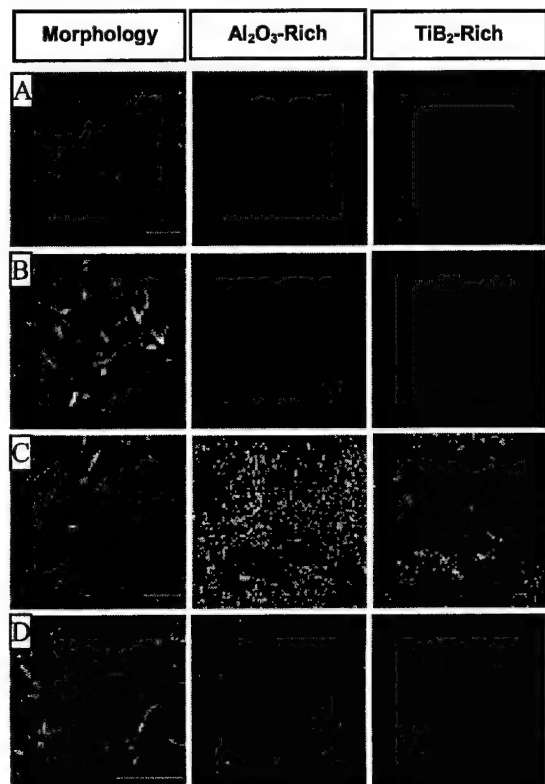


Fig. 4 Fracture Surfaces

### DISCUSSION

The analysis has yielded dynamic compressive strength between 4.3 and 5.3 GPa, indicating a strong dependence of strength on microstructure. Microstructures with finer phases as indicated by smaller linear intercept length values have higher strength levels. The dynamic strength levels are

approximately 27% higher than the values of 3-4 GPa measured at quasi-static loading rates. Scanning electron microscopy and energy dispersive spectrometry indicate that failure associated with the  $Al_2O_3$  phase is transgranular cleavage in all microstructures. Failure associated with the  $TiB_2$  phase is a combination of transgranular cleavage and intergranular debonding and varies with the microstructures. The fraction of  $TiB_2$ -rich fracture surface areas directly correlates with the measured compressive strength of the materials. The addition of titanium diboride reinforcement clearly improves the failure resistance of the materials.

### ACKNOWLEDGEMENT

Support from the ARO and NSF is gratefully acknowledged. We are grateful to Dr. K. V. Logan for providing the materials and helpful discussions.

### REFERENCES

1. Anderson, C.E., Morris, B.L., (1992), "The Ballistic Performance of Confined  $Al_2O_3$  Ceramic Tiles", *International Journal of Impact Engineering*, 12(2), 167-187;
2. Bilek, Z., Helesic, J., (1990), "Mechanical Properties of Aluminum Oxide at High Loading Rates", *Proceedings of the First European East-West Symposium on Materials and Processes*, 381-394;
3. Carney, A.F., (1997), "The Effect of Microstructure on the Mechanical Properties of a Titanium Diboride/Alumina Composite", Masters Thesis, Georgia Institute of Technology, Atlanta, GA;
4. Komanduri, R., (1989), "Advanced Ceramic Tool Materials for Machining", *Int. J. Refract. Hard. Met.*, 8, 125-132;
5. Logan, K.V., (1992a), "Shapes Refractory Products and Method of Making the Same", U.S. Patent # 5141900;
6. Logan, K.V., (1992b), Elastic-Plastic Behavior of  $TiB_2/Al_2O_3$  Produced by SHS, Ph.D. Dissertation, Georgia Institute of Technology;
7. Nemat-Nasser, S., (1991), New frontiers in Dynamic Recovery Testing of Advanced Composites: Tailoring Microstructures for Optimal Performance, *JSME International Journal*, series I, 34(2), 111;
8. Niihara, K., Nakahira, A., Sekino, T., (1991), New Nanocomposite Structural Ceramics, *Mat. Research Society Symposium Proceedings*, 286, 405-412;
9. Nordgen, A., Melander, A., (1988), "Influence of Porosity on Strength of WC-10%Co Cemented Carbide", *Powder Metallurgy*, 31(3), 189-200;
10. Viechnicki, D.J., Slavin, M.L., Kliman, M.I., (1991), *Ceramics Bulletin*, 70, 1035.

# MICROMECHANICAL MODELING OF MIXED-MODE CRACK GROWTH IN CERAMIC COMPOSITES

J. Zhai and M. Zhou

Authorized Reprint from Standard Technical Publication 1359 © Copyright 1999  
American Society for Testing and Materials, 100 Barr Harbor Drive, West Conshohocken, PA 19428-2959

## Micromechanical Modeling of Mixed-Mode Crack Growth in Ceramic Composites

**REFERENCE:** Zhai, J. and Zhou, M., "Micromechanical Modeling of Mixed-Mode Crack Growth in Ceramic Composites," *Mixed-Mode Crack Behavior: ASTM STP 1359*, K. J. Miller and D. L. McDowell, Eds., American Society for Testing and Materials, West Conshohocken, PA, 1999, pp. 174-200.

**ABSTRACT:** Dynamic crack propagation in ceramic composites is analyzed numerically. The simulations concern the effects of microstructural morphologies on fracture. The analysis considers arbitrary phase distributions in the actual microstructures of alumina/titanium diboride ( $\text{Al}_2\text{O}_3/\text{TiB}_2$ ) composites. The microstructures analyzed have different phase morphologies and different phase sizes over an order of magnitude in length (from 1-2 to 10-20  $\mu\text{m}$ ). A micromechanical model that provides explicit account for arbitrary microstructures and arbitrary fracture patterns is developed and used. The approach uses both a constitutive law for the bulk solid constituents and a constitutive law for fracture surfaces. The model is based on the cohesive surface formulation of Xu and Needleman and represents a phenomenological characterization for atomic forces on potential crack/microcrack surfaces. This framework of analysis does not require the use of any fracture criteria. Instead, fracture evolves as an outcome of bulk material response, interfacial behavior, and applied loading. This approach provides a unified and self-consistent treatment of mixed mode fracture. The evolutions of crack lengths in different phases and along interphase interfaces are calculated to track crack growth. The overall local crack speed, defined as the time rate of change of arc length along zigzagging crack paths, is found to reach the intersonic range, i.e., greater than the shear wave speeds and smaller than the longitudinal wave speeds in the constituent phases. The model also allows the energy release rate to be evaluated easily. For the same amount of crack surfaces generated, the average energy release rates for fracture patterns in four microstructures analyzed differ by up to 25%. The results demonstrate that larger  $\text{TiB}_2$  reinforcements significantly impede crack propagation and increase the fracture resistance of the composites, as indicated by higher average energy release rate values.

**KEYWORDS:** micromechanical modeling, cohesive force, fracture, inhomogeneous materials, elasticity, mixed-mode fracture, fracture mode, numerical simulation, crack propagation, ceramic composites

### Nomenclature

$C_L$	Longitudinal wave velocity
$C_s$	Shear wave velocity
$C_R$	Rayleigh wave velocity
$\tau_{\max}$	Maximum shear stress for a cohesive surface pair
$\sigma_{\max}$	Maximum tensile stress for a cohesive surface pair
$\delta_n$	Characteristic length for normal separation
$\delta_t$	Characteristic length for tangential separation

<sup>1</sup> The George W. Woodruff School of Mechanical Engineering, Georgia Institute of Technology, Atlanta, GA 30332-0405. (M. Zhou is author to whom correspondence should be addressed.)

$\phi_0$	Surface energy per unit area
$\phi_{\text{crack}}$	Fracture energy associated with crack growth
$\partial\phi_{\text{crack}}/\partial a$	Energy release rate per apparent crack growth
$\partial\phi_{\text{crack}}/\partial l$	Energy release rate per local crack growth

Microscopically inhomogeneous materials derive significantly higher strength and toughness from microscopic reinforcements such as fibers and particles. The enhancement is due to the higher toughness and strength of the additional phases and deformation mechanisms that do not come into play for monolithic materials. In addition to different length scales associated with material inhomogeneities, different time scales are also introduced by composite microstructures under transient loading due to different stress wave speeds or the inertia effect. These spatial and temporal effects provide opportunities for material property enhancement through multiple deformation and failure mechanisms. For example, material inhomogeneities and reinforcements force cracks to follow tortuous paths therefore increasing dissipation and fracture resistance. Micromechanical modeling and simulation represents a unique and attractive means for delineating the effects of micro and meso failure mechanisms. The dynamic failure of brittle materials has been extensively analyzed, for example, [1-20]. Most available models for the failure are, for the most part, continuum damage theories in which the net effect of fracture is idealized as a degradation of the elasticity modulus, for example, see Refs 21-29. While capturing the macroscopic or effective response, these models do not explicitly consider the discrete nature of fracture through crack growth and coalescence. Thus, the models lack the ability to account for the interaction between cracks and resolve specific failure modes and failure patterns. In addition, the effects of microstructural inhomogeneities of different size scales such as inclusions, fibers, and grains on crack path and fracture toughness cannot be explicitly analyzed.

The complex morphologies of material microstructures precludes the application of analytical methods. Explicit micromechanical modeling and simulation represent a unique means for analyzing micro and meso failure and for elucidating scaling laws. Through the consideration of representative samples of actual microstructures, the effects of various fracture mechanisms can be delineated. The required features of this framework should: (1) allow explicit account of real, arbitrary material microstructures, (2) permit explicit modeling of fracture in a nonconstrained (arbitrary crack paths or microcrack patterns) manner, and (3) be free of limitations of fracture criteria applicable only over certain length scales (such as continuum criteria that assume the existence of  $K$ -fields). Combined use of the cohesive surface approach of Xu and Needleman [30,31] and bulk constitutive laws is a good candidate for providing such a framework. Explicit simulation of fracture and fragmentation have also been carried out by Camacho and Ortiz [32] and Ortiz [33] using a cohesive model in the analysis of dynamic failure of materials.

Alumina/titanium diboride ( $\text{Al}_2\text{O}_3/\text{TiB}_2$ ) composites with a wide range of microstructural morphologies demonstrate a range of failure resistance and a strong dependence of fracture toughness on microstructure in experiments, see Logan [34]. These materials are composed of titanium diboride ( $\text{TiB}_2$ ) reinforcements embedded in a matrix of alumina ( $\text{Al}_2\text{O}_3$ ). The principal modes of failure observed in experiments are transgranular and intergranular fracture of  $\text{Al}_2\text{O}_3$  matrix, reflecting the effects of different phase distributions, different size scales, and different interfacial bonding strengths that result from various processing conditions. For example, the principal mode of failure is interfacial fracture through microcrack formation when a weak interfacial bonding between the constituents is found. Clearly, interfacial strength significantly influences the overall behavior of the composites. A numerical analysis on the effect of interfacial strength on failure modes has been conducted in Zhai

and Zhou [35]. The analyses here concern the effects of microstructure on the fracture resistance of  $\text{Al}_2\text{O}_3/\text{TiB}_2$  composites. The focus is crack path, crack speed, and energy release rate. Explicit account is taken of arbitrary crack and microcrack fracture patterns as well as of arbitrary microstructures. As in Xu et al. [30], the crack surfaces are regarded as cohesive surfaces exhibiting traction forces that are functions of interfacial separations. These relations represent phenomenological characterizations of the atomistic attraction and repulsion forces that vary with inter-atomic displacements. All finite element boundaries between elements are cohesive surfaces serving as potential crack paths. Arbitrary crack and microcrack patterns can be resolved through the use of fine meshes. This approach does not require any crack initiation and propagation criterion. Instead, the cohesive surface constitutive law allows fracture to evolve as a natural outcome of the combined effects of bulk constituent response, interfacial behavior, and applied loading.

### Problem Formulation

To account for the finite strains involved in crack tip regions, a Lagrangian finite deformation formulation is used. The independent variables are the position of a material point in the reference configuration  $\mathbf{x}$ , and time  $t$ . Relative to a fixed Cartesian frame  $\{\xi^i\}$ , a material point initially at  $\mathbf{x}$  occupies position  $\bar{\mathbf{x}}$  in the current configuration. The displacement vector and the deformation gradient are defined as  $\mathbf{u} = \bar{\mathbf{x}} - \mathbf{x}$  and  $\mathbf{F} = \partial\bar{\mathbf{x}}/\partial\mathbf{x}$ , respectively. The principle of virtual work includes a contribution from the cohesive surfaces and is written as

$$\int_V \mathbf{s} : \delta \mathbf{F} dV - \int_{S_{\text{int}}} \mathbf{T} \cdot \delta \Delta dS = \int_{S_{\text{ext}}} \mathbf{T} \cdot \delta \mathbf{u} dS - \int_V \rho \frac{\partial^2 \mathbf{u}}{\partial t^2} \cdot \delta \mathbf{u} dV \quad (1)$$

where  $\mathbf{s} : \delta \mathbf{F} = s^i \delta F_{ji}$ ,  $\mathbf{s}$  is the nonsymmetric first Piola-Kirchhoff stress;  $\Delta$  is the displacement jump across a pair of cohesive surfaces;  $V$ ,  $S_{\text{ext}}$  and  $S_{\text{int}}$  are the volume, external surface area, and internal cohesive surface area, respectively, of the body in the reference configuration. The density of the material in the reference configuration is  $\rho$ . Also,  $\delta \mathbf{F}$ ,  $\delta \Delta$  and  $\delta \mathbf{u}$  denote admissible variations  $\mathbf{F}$ ,  $\Delta$  and  $\mathbf{u}$  respectively. The traction vector  $\mathbf{T}$  and the surface normal in the reference configuration  $\mathbf{n}$  are related through  $\mathbf{T} = \mathbf{n} \cdot \mathbf{s}$ . The volumetric constitutive law is hyperelastic so that

$$\mathbf{S} = \frac{\partial W}{\partial \mathbf{E}} \quad (2)$$

where  $\mathbf{S} = \mathbf{s} \cdot \mathbf{F}^{-T}$  is the second Piola-Kirchhoff stress. The strain energy density  $W$  is taken to be

$$W = \frac{1}{2} \mathbf{E} : \mathbf{L} : \mathbf{E} \quad (3)$$

with

$$\mathbf{L} = \frac{E}{1+v} \left( \mathbf{H} + \frac{v}{1-2v} \mathbf{I} \otimes \mathbf{I} \right) \quad (4)$$

being the tensor of isotropic elastic moduli.  $E$  and  $v$  are the Young's modulus and Poisson's ratio, respectively.  $E$  is the Lagrangian strain given by

$$E = \frac{1}{2} (\mathbf{F}^T \cdot \mathbf{F} - \mathbf{I}) \quad (5)$$

Also in the above formulas,  $\mathbf{II}$  is the fourth order identity tensor,  $\mathbf{I}$  is the second order identity tensor,  $\mathbf{I} \otimes \mathbf{I}$  denotes the tensor product of two second order tensors, and  $(\cdot)^T$  and  $(\cdot)^{-T}$  denote inverse and inverse transpose, respectively.

The constitutive law for cohesive surfaces relates the traction and displacement jumps across crack surfaces and is also taken to be hyperelastic so that any dissipation associated with separation is neglected. Assuming the surface potential energy is  $\phi$ , the traction on the cohesive surfaces can be derived through

$$\mathbf{T} = \frac{\partial \phi}{\partial \Delta} \quad (6)$$

In two dimensions, the specific form of  $\phi$  used here is

$$\phi(\Delta) = \phi_0 - \phi_0 \left( 1 + \frac{\Delta_n}{\delta_n} \right) \exp \left( -\frac{\Delta_n}{\delta_n} \right) \exp \left( -\frac{\Delta_t^2}{\delta_t^2} \right) \quad (7)$$

where  $\Delta_n = \mathbf{n} \cdot \Delta$  and  $\Delta_t = \mathbf{t} \cdot \Delta$  are the normal and tangential displacement jumps, with  $\mathbf{n}$  and  $\mathbf{t}$  denoting unit vectors along the surface normal and tangent in the reference configuration, respectively. Potential  $\phi$  is written such that  $\phi(\Delta)|_{|\Delta|=0} = 0$  and therefore  $\phi_0 = \phi(\Delta)|_{|\Delta| \rightarrow \infty}$  is the work of separation. Two special paths of decohesion are considered to illustrate the variations of the cohesive traction components. The first path is pure normal separation with tangential traction component  $T_t = \mathbf{t} \cdot \mathbf{T} = 0$  and tangential separation  $\Delta_t = 0$ . The second path is pure tangential separation with normal traction component  $T_n = \mathbf{n} \cdot \mathbf{T} = 0$  and normal separation  $\Delta_n = 0$ . The works of normal and tangential separations along these two paths are equal to each other and are taken to be  $\phi_0 = e\sigma_{\max} \delta_n = \sqrt{e/2}\tau_{\max} \delta_t$ , with  $e = \exp(1) = 2.718281829$ .  $\delta_n$  and  $\delta_t/\sqrt{2}$  are normal and shear displacement jump values at which maximum normal stress  $\sigma_{\max}$  and maximum shear stress  $\tau_{\max}$  occur, respectively.

The cohesive surface traction components obtained from Eqs 6 and 7 are

$$T_n(\Delta) = \frac{\phi_0 \Delta_n}{\delta_n^2} \exp \left( -\frac{\Delta_n}{\delta_n} \right) \exp \left( -\frac{\Delta_t^2}{\delta_t^2} \right) \quad (8)$$

and

$$T_t(\Delta) = -\frac{2\phi_0 \Delta_t}{\delta_t^2} \left( 1 + \frac{\Delta_n}{\delta_n} \right) \exp \left( -\frac{\Delta_n}{\delta_n} \right) \exp \left( -\frac{\Delta_t^2}{\delta_t^2} \right) \quad (9)$$

These relations are illustrated in Fig. 1. Clearly, there are cross dependencies of normal traction on shear displacement jumps and shear traction on normal displacement jumps. When displacement jumps exceed certain values, both traction components decrease with further increase in separations and approach zero as  $|\Delta| \rightarrow \infty$ . Under negative normal sepa-

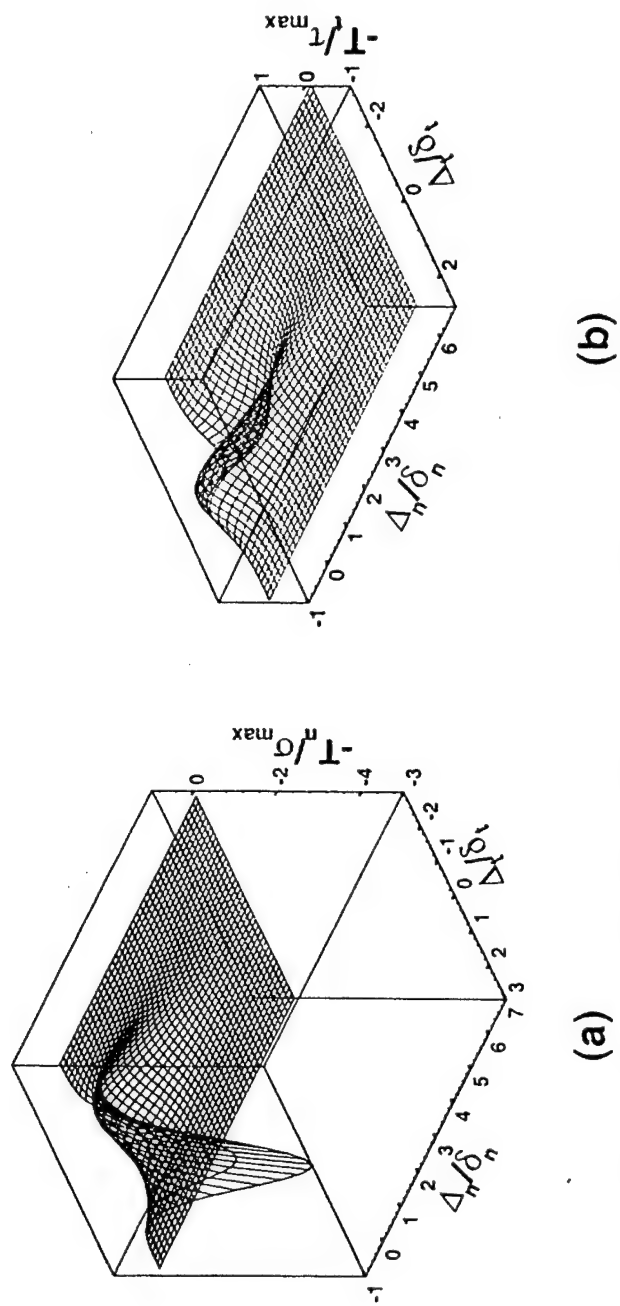


FIG. 1—An illustration of the constitutive behavior of cohesive surfaces, (a) normal traction, (b) shear traction.

rations (interpenetration), the normal traction component increases rapidly, simulating the strong atomistic repulsion during compression.

The balance of energy requires that the total external work  $\mathfrak{W}$  done to a body to be equal to the sum of the strain energy  $\mathfrak{W}$  stored in the bulk material, the kinetic energy  $\mathfrak{K}$  in the body and the cohesive surface energy  $\Phi$ , meaning

$$\mathfrak{W} = \int_{S_{\text{ext}}} \mathbf{T} \cdot \mathbf{u} dS = \mathfrak{K} + \mathfrak{W} + \Phi \quad (10)$$

where

$$\left. \begin{aligned} \mathfrak{K} &= \int_V \frac{1}{2} \rho \frac{\partial \mathbf{u}}{\partial t} \cdot \frac{\partial \mathbf{u}}{\partial t} dV \\ \mathfrak{W} &= \int_V W dV \\ \Phi &= \int_{S_{\text{int}}} \phi dS \end{aligned} \right\} \quad (11)$$

and

The cohesive energy  $\Phi$  is the amount of energy spent on generating new crack surfaces, therefore represents a measure of the energy consumption on fracture. Under the same loading conditions, the higher the  $\Phi$  required for generating the same amount of crack surfaces, the higher the fracture resistance of the material. In the analyses carried out there, this energy is used to compare the fracture resistance of specimens with different microstructures under the same overall remote loading.

### Problem Analyzed

Computations are carried out for a center-cracked specimen, as illustrated in Fig. 2. The specimen has an initial height of  $2H = 1.6$  mm and an initial width of  $2L = 1.6$  mm. An initial crack of length  $2a_0 = 0.4$  mm exists along the  $\xi^1$  axis. Only one half of the specimen ( $\xi^1 > 0$ ) is discretized and modeled in the simulations because of symmetry with respect to the  $\xi^2$  axis. Conditions of plain strain are assumed to prevail. The small region in front of the crack tip contains microstructures digitized from micrographs of actual composite materials, see Fig. 3. Inside this region, the material inhomogeneities and material phase distribution are explicitly modeled. The dimensions for this region are limited by the memory sizes of the Cray T90 and J90 computers used in this work. As seen below, the particular dimensions chosen here (100 by 200  $\mu\text{m}$ ) are much larger than most size scales in the microstructures analyzed. Digitized microstructures of actual  $\text{Al}_2\text{O}_3/\text{TiB}_2$  composites shown in Fig. 4 are used in the analyses. In these micrographs, the  $\text{Al}_2\text{O}_3$  matrix appears lighter and the harder  $\text{TiB}_2$  reinforcements appear darker. These microstructures have  $\text{TiB}_2$  volume fractions between 15 to 25%. In microstructures (a-c), the  $\text{TiB}_2$  particles are embedded in the alumina matrix. The average grain size is approximately 10–20  $\mu\text{m}$  for (a), 8–10  $\mu\text{m}$  for (b), and 1–2  $\mu\text{m}$  for (c). The composite microstructure in Fig. 4(d) consists of a population of isolated  $\text{Al}_2\text{O}_3$  matrix islands surrounded by a network of  $\text{TiB}_2$  reinforcements. The isolated matrix areas are approximately 20 by 100  $\mu\text{m}$  in size. A dispersion of small  $\text{Al}_2\text{O}_3$  particles several microns in size are scattered in the  $\text{TiB}_2$  phase. Clearly, two length scales

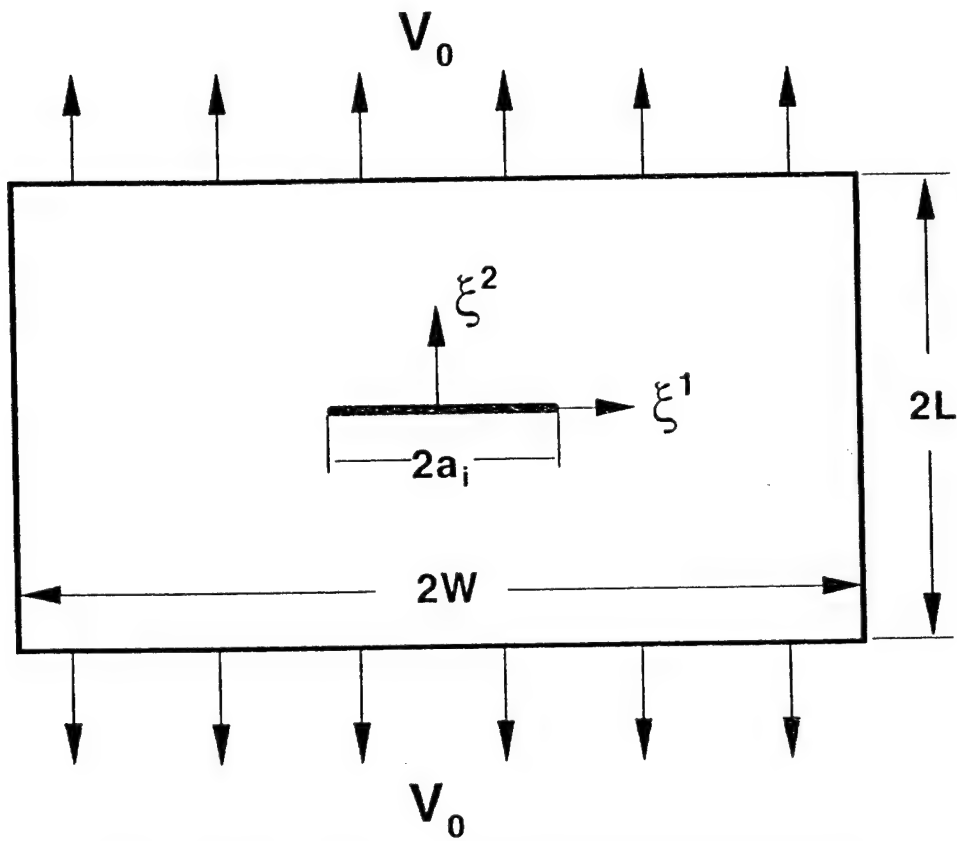


FIG. 2—Problem analyzed: a centered-cracked specimen under tensile loading.

are operative in this microstructure, influencing its deformation and failure, and consequently determining its strength and fracture toughness. The different microstructural phase morphologies are the result of different conditions during hot pressing, see Logan [34]. Partly because of the differences in their microstructures, these materials have shown a range of fracture toughness and failure resistance. The current analyses focus on the effects of these different phase morphologies on the fracture behavior of the specimen shown in Fig. 2. The effects of different interfacial bonding strengths that may also result from the different processing conditions are not specifically analyzed here. Some results concerning the influence of interphase bonding strength on failure modes in these materials are given in Zhai et al. [35]. In the current analyses, each of the phases behaves hyperelastically. Depending on material properties, boundary conditions, and loading, fracture is possible inside each of the phases and along the interfaces between the phases. The bulk properties of each finite element are those for either the grains or those for the matrix. The properties of each segment of potential fracture surface are specified according to location as those belonging to the matrix, the reinforcements or the matrix/reinforcement interfaces. The material and model parameters are listed in Table 1 (bulk properties) and Table 2 (cohesive surface constitutive properties). For comparison and analysis purposes, the speeds for the longitudinal stress waves ( $c_L$ ), the shear stress waves ( $c_s$ ) and the Rayleigh surface waves ( $c_R$ ) are also listed in Table

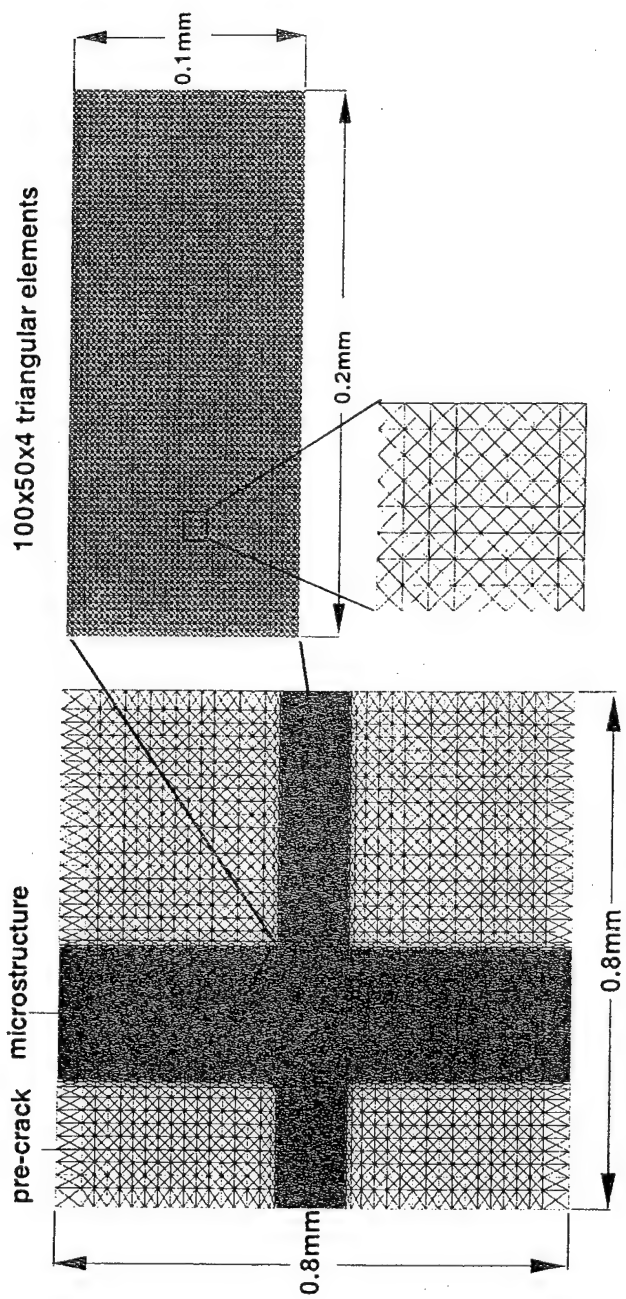


FIG. 3—Finite element model and mesh for the specimen.

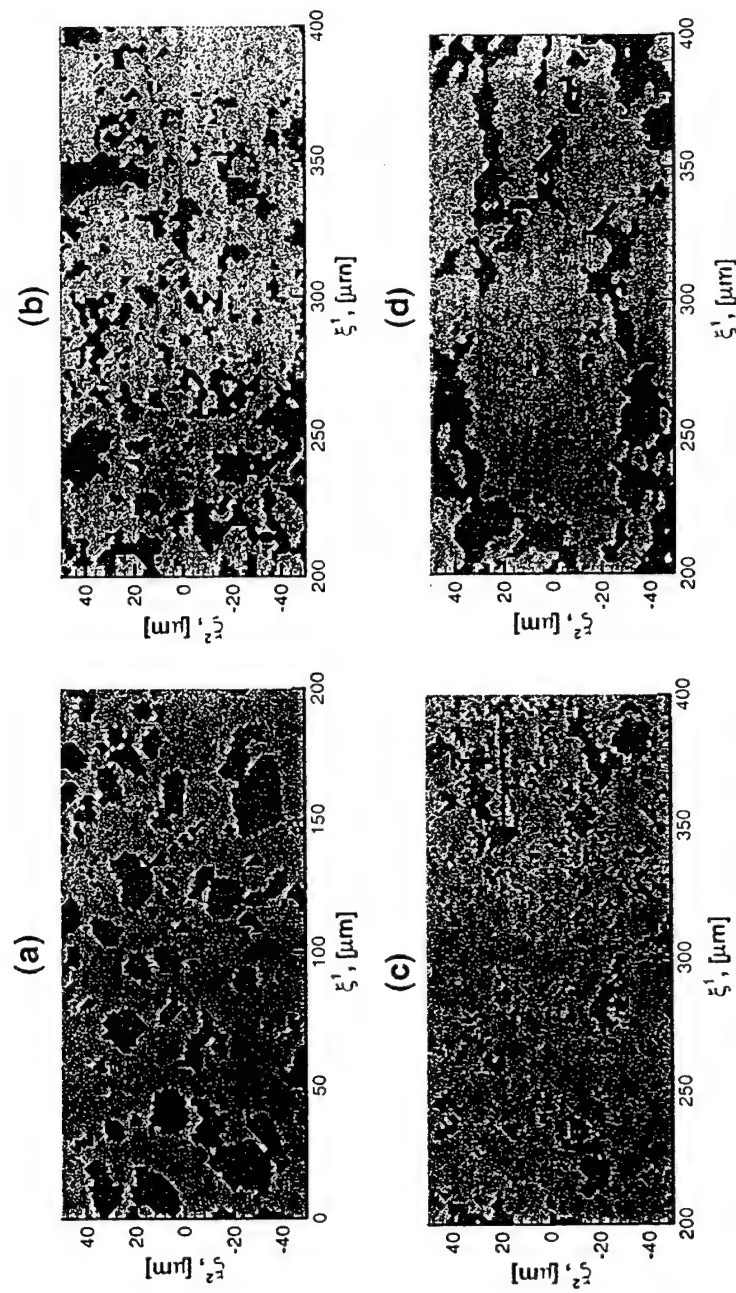


FIG. 4—Microstructural morphologies analyzed: (a)  $TiB_2$  embedded in  $Al_2O_3$ , grain size is 10–20  $\mu m$ , (b)  $TiB_2$  embedded in  $Al_2O_3$ , cell size is approximately 100  $\mu m$ , (c)  $TiB_2$  embedded in  $Al_2O_3$ , grain size is 1–2  $\mu m$ , (d) a network of  $TiB_2$ , filled with  $Al_2O_3$ , cell size is approximately 8–10  $\mu m$ .

TABLE 1—*Bulk material properties.*

Compound	Density kg/m <sup>3</sup>	$K_{IC}$ MPa $\sqrt{\text{m}}$	E GPa	v	$c_L$ , m/s	$c_s$ , m/s	$c_R$ , m/s
$\text{Al}_2\text{O}_3$	3990	4.0	340	0.23	9939	5885	5379
$\text{TiB}_2$	4520	7.2	500	0.12	10694	7027	6267
Homogenized $\text{Al}_2\text{O}_3/\text{Ti}_2\text{B}$ Composite	4120	3.6	415	0.15	10300	6609	5936

1. The choice of the cohesive law parameters assumes that  $\sigma_{\max} = E/10$  for each constituent with  $E$  being the Young's modulus and  $\phi_0 = (1 - v^2)K_{IC}^2/E$  with  $K_{IC}$  being the Mode I fracture toughness of the materials in question. The parameters for the  $\text{Al}_2\text{O}_3/\text{TiB}_2$  interfaces are chosen such that the maximum stress  $\sigma_{\max}$  is lower than that for either the matrix or the reinforcements. Specifically, both  $\sigma_{\max}$  of interfacial work of separation  $\phi_0$  are 1–3 of those for the matrix, consistent with what is typically reported for ceramic composites.

Materials outside the crack-tip region are assumed to be homogeneous and are assigned a set of effective parameters representative of those for the  $\text{Al}_2\text{O}_3/\text{TiB}_2$  ceramic composite. Both regions are discretized in the same manner, using both the bulk and the cohesive surface constitutive descriptions. The specimen is stress-free and at rest initially. Tensile loading is applied by imposing symmetric velocity boundary conditions along the upper and lower edges of the specimen. For the results discussed here, the imposed boundary velocity is  $V_0 = 10$  m/s for each edge with a linear ramp from zero to this maximum velocity in the first 0.01  $\mu\text{s}$  of loading. All other specimen surfaces have traction-free boundary conditions. Specifically, the loading conditions are

$$\dot{u}^2(\xi^1, \pm H, t) = \begin{cases} \pm \frac{t}{0.001} V_0, & t < 0.01 \mu\text{s} \\ \pm V_0, & t \geq 0.001 \mu\text{s} \end{cases} \quad -L < \xi^1 < L \quad (12)$$

$$T^1(\xi^1, \pm H, t) = 0, \quad -L < \xi^1 < L \quad (13)$$

$$T^1(\pm L, \xi^2, t) = T^2(\pm L, \xi^2, t) = 0, \quad -H < \xi^2 < H \quad (14)$$

This set of conditions represents the loading of the pre-crack by a tensile wave with a stress amplitude of 424 MPa [ $(\rho c_L)_{\text{composite}} V_0$ ] and a linear ramp from zero to that value in 0.01  $\mu\text{s}$ .

TABLE 2—*Constitutive parameters for cohesive surfaces.*

Cohesive Surface Pair	$\sigma_{\max}$ , GPa	$\tau_{\max}$ , GPa	$\delta_n, \delta_p$ , nm	$\phi_0$ , J/m <sup>2</sup>
$\text{Al}_2\text{O}_3$	34.0	78.2	0.5	46.2
$\text{TiB}_2$	50.0	11.5	1.0	135.9
Homogenized $\text{Al}_2\text{O}_3/\text{Ti}_2\text{B}$ Composite	41.5	95.5	0.3	33.8
$\text{Al}_2\text{O}_3/\text{TiB}_2$ Interface	11.3	26.1	0.5	15.4

### Finite Element Method

Finite element discretization is based on linear-displacement triangular elements arranged in a "crossed-triangle" quadrilateral pattern. Neighboring elements are connected through cohesive surfaces. Hence, for the uniform mesh region in front of the crack tip in Fig. 3, the cohesive surfaces are initially oriented along four directions, horizontal (0°), vertical (90°), positive and negative 45° ( $\pm 45^\circ$ ). Since a very fine mesh is used (the element size is 1  $\mu\text{m}$ ), arbitrary fracture paths or patterns can be resolved. When the finite element discretization of the displacement field is substituted into the principle of virtual work (Eq 1), the discretized equations of motion take the form

$$\mathbf{M} \frac{\partial^2 \mathbf{U}}{\partial t^2} = \mathbf{R} \quad (15)$$

where  $\mathbf{U}$  is the vector of nodal displacements,  $\mathbf{M}$  is the nodal mass matrix, and  $\mathbf{R}$  is the nodal force vector consisting of contributions from the bulk elements and the cohesive surfaces. A lumped mass matrix is used in Eq 15 instead of the consistent mass matrix for reasons of efficiency and accuracy during explicit time-integration Krieg and Key [36]. The explicit time-integration scheme based on the Newmark  $\beta$ -method with  $\beta = 0$  and  $\gamma = 0.5$  Belytschko et al. [37] is employed to integrate Eq 15.

### Results

To illustrate the progression of fracture in the four microstructures, the distributions of  $\sigma_{22}$  at several different times for four calculations using these microstructures are shown on the corresponding deformed configurations in Figs. 5–8, respectively. The microstructural phase boundaries are outlined by solid dark lines for visualization of the phase morphologies. In order to quantify the progress of crack propagation, the new crack surface areas (or crack lengths in two dimensions) generated in the two phases and along matrix/reinforcement interfaces are calculated separately and analyzed. The crack length histories for these cases are shown in Figs. 9a–d, respectively. The crack lengths in the matrix and along the interfaces as well as the total crack length  $l(t)$  in the composite are shown. Note that  $l(0) = 0$ , therefore, crack lengths referred to here concern new crack surfaces generated and are independent of the initial pre-crack. Since crack propagation occurs mainly in the matrix and along the phase interfaces, the crack length in the TiB<sub>2</sub> reinforcements is relatively small and therefore not shown. The total crack length histories  $l(t)$  shown in Fig. 9 are differentiated with respect to time to yield the rate at which new crack surfaces are generated. Note that  $l$  is the arc length along crack paths. The time derivative  $dl/dt$  may not always represent crack speed due to possible occurrences of multiple crack fronts or simultaneous microcrack formation. However, it can be used as a relative measure of the extent of damage in the materials. On the other hand, when fracture occurs in the form of a single crack,  $dl/dt$  represents the local crack speed as a function of time. For comparison purposes, the apparent crack speed,  $da/dt$ , where  $a$  is the projection of  $l$  in the  $\xi^1$  (horizontal) direction, is also calculated. The apparent crack length  $a$  is taken to be nondecreasing, therefore,  $da/dt \geq 0$ . The apparent crack speed is what is most often measured in experiments. The profiles of both  $dl/dt$  and  $da/dt$  for the four cases are shown in Fig. 10. The oscillations in these profiles show the dynamic and unsteady nature of crack growth in the inhomogeneous material microstructure, although some of the noise may be attributed to errors in the numerical differentiation of  $l(t)$  and  $a(t)$ .

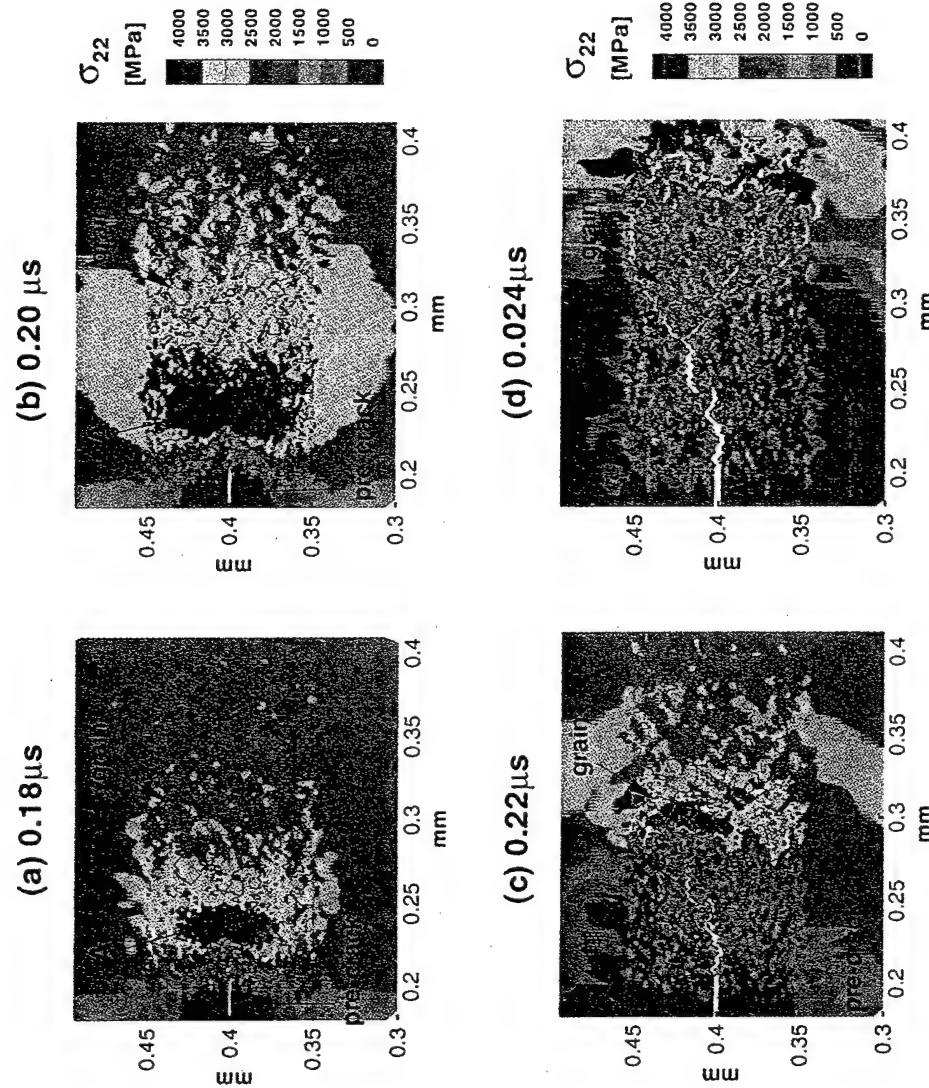


FIG. 5—Distributions of  $\sigma_{22}$  at four different times for a specimen with microstructure in Fig. 4a,  $V_o = 10$  m/s.

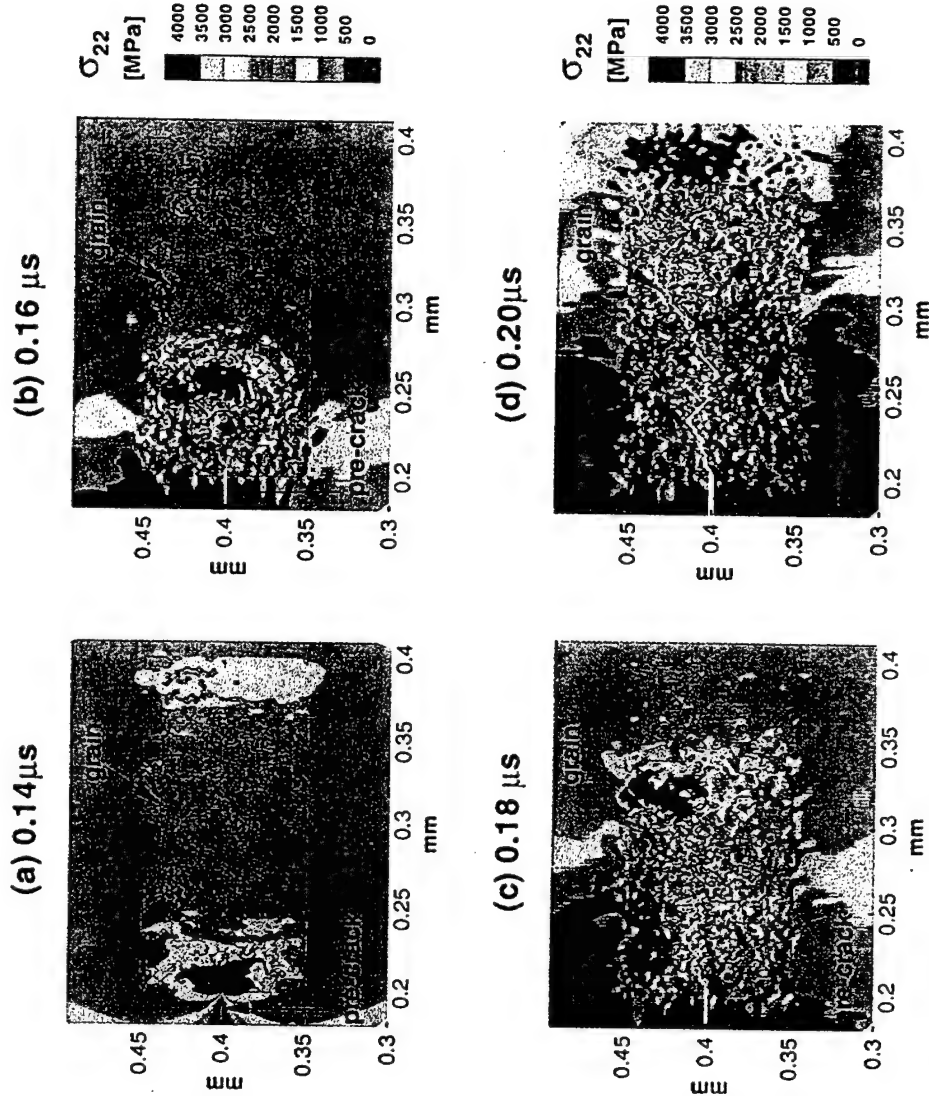


FIG. 6—Distributions of  $\sigma_{22}$  at four different times for specimen with microstructure in Fig. 4b,  $V_a = 10 \text{ m/s}$ .

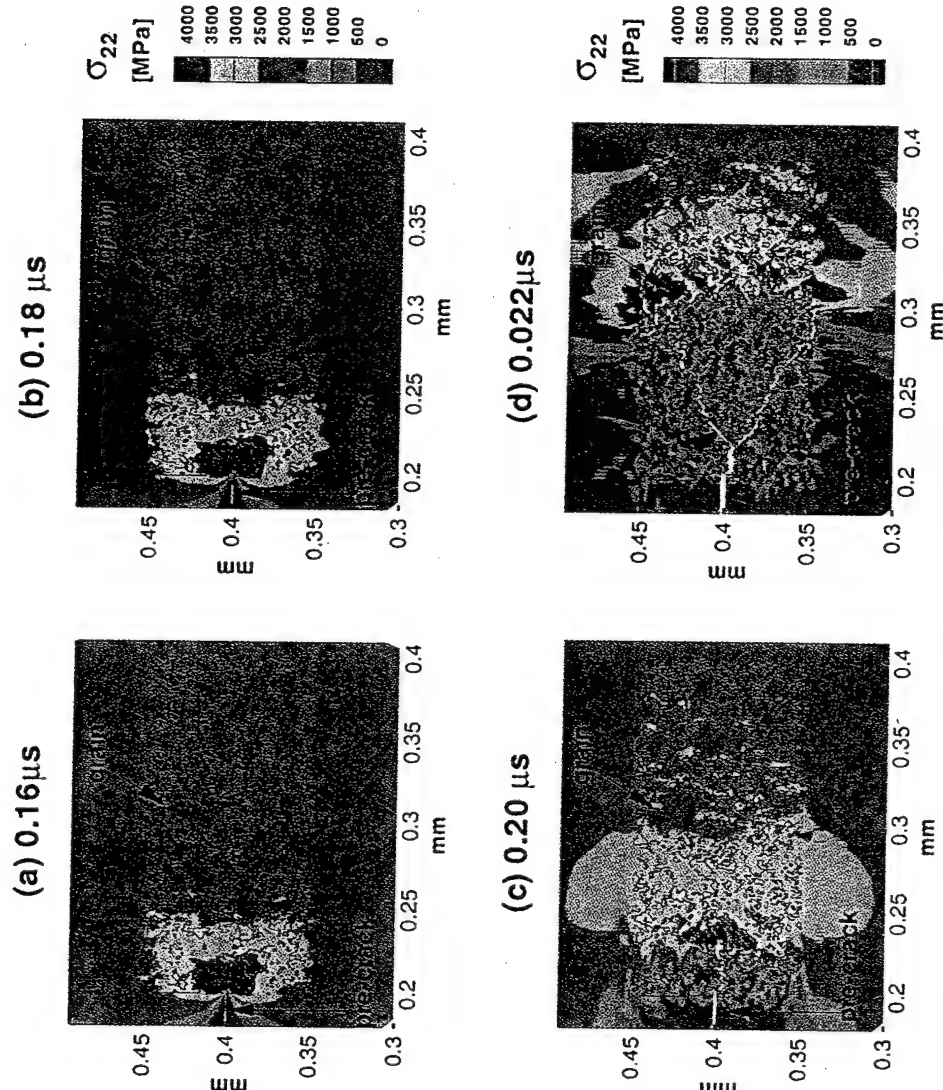


FIG. 7—Distributions of  $\sigma_{22}$  at four different times for a specimen with microstructure in Fig. 4c,  $V_0 = 10 \text{ m/s}$ .

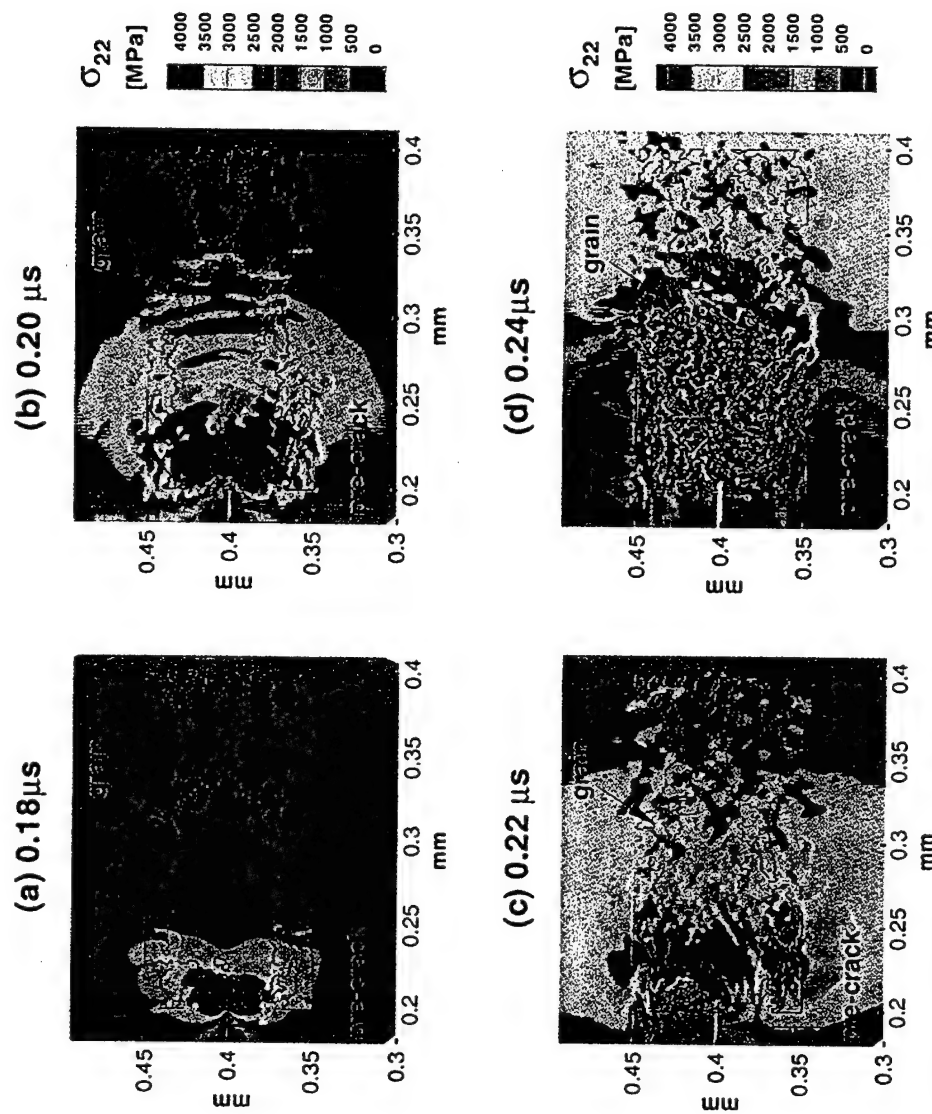
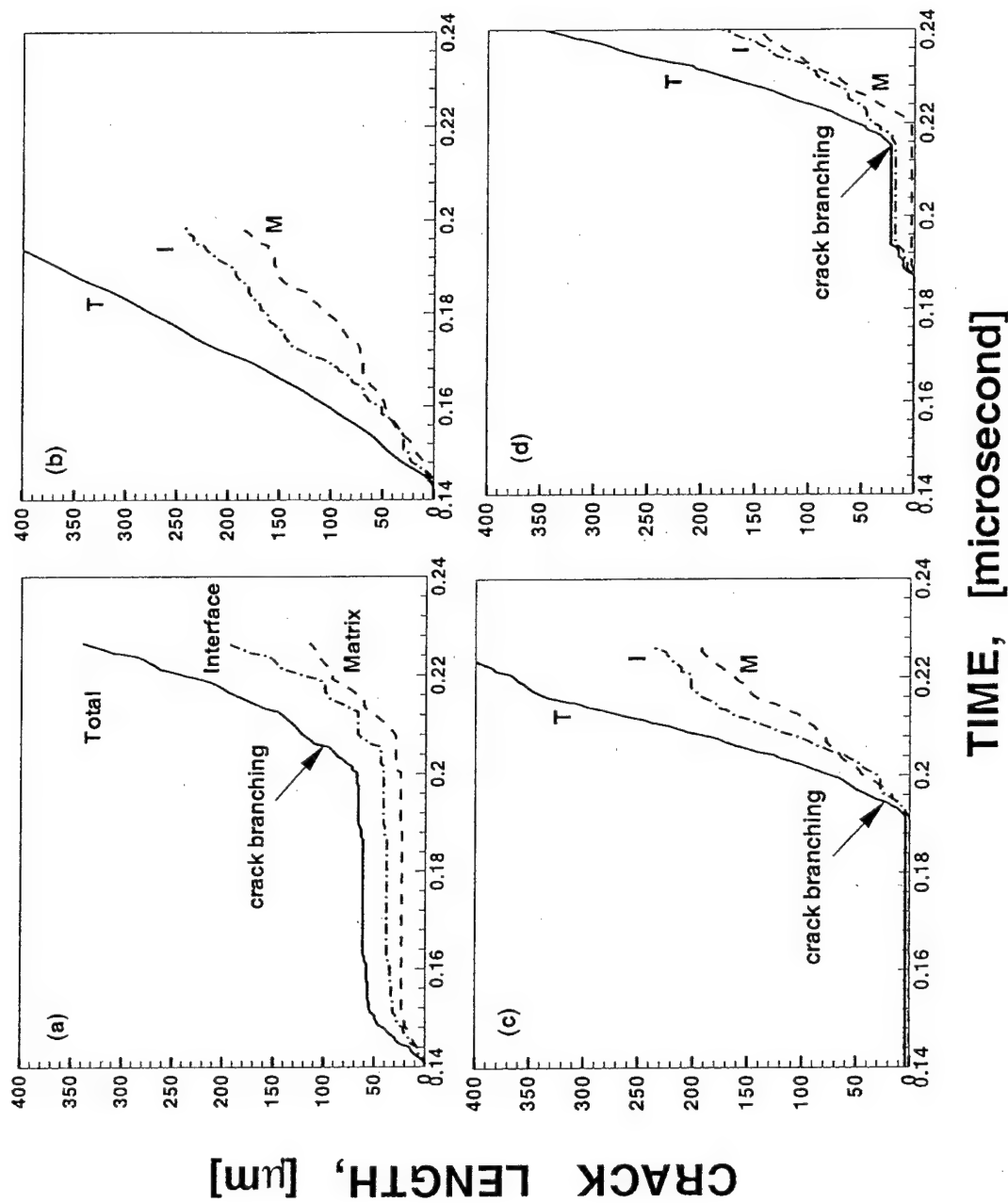


FIG. 8—Distributions of  $\sigma_{22}$  at four different times for a specimen with microstructure in Fig. 4d,  $V_o = 10$  m/s.



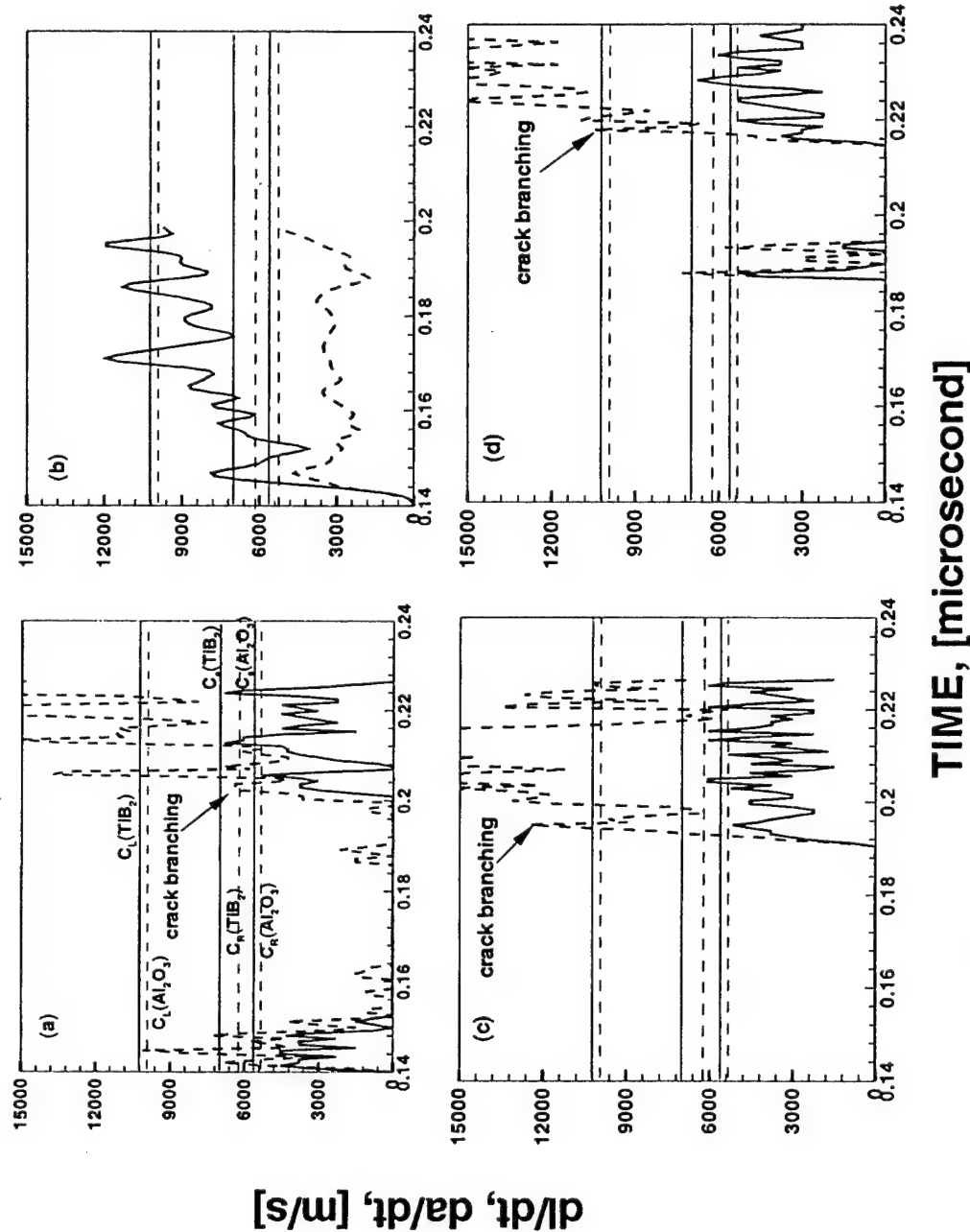


FIG. 10—A comparison of crack speed histories for the four microstructures.

### *Crack Propagation in a Heterogeneous $Al_2O_3/TiB_2$ Microstructure*

First, the results for the microstructure in Fig. 4a are discussed. Figure 5 and Fig. 9a show that crack initiation occurs at approximately 0.14  $\mu$ s. The crack first zigzags in the matrix between small  $TiB_2$  particles and then arrests when the crack tip impinges on a large grain at point A, Figs. 5a-b. This grain represents a stronger obstacle to crack growth due to its higher bulk and cohesive strengths. As a result, the crack is essentially stationary between 0.15 and 0.20  $\mu$ s, see Figs. 9a and 10a. There is an increase in stress intensity in front of the crack tip during this period as indicated by the size of the area with high stresses. The attainment of higher stresses allows the crack to circumvent the impeding grain through the separation of grain/matrix interface, Fig. 5c-d. Part of the debonding process involves primarily local tangential (shear) displacement along the interface. After the grain at A, subsequent propagation is primarily through the matrix and interfaces between small particles and the matrix. The crack eventually branches into two propagating tips at approximately 0.204  $\mu$ s and their overall characteristics are the same as those for the parent crack, Fig. 5d. It can be seen in Fig. 9a that more crack surfaces are created along the phase boundaries than in the matrix, reflecting the effect of the weaker bonding between the phases compares with the cohesive strengths of the constituents.

In Fig. 10a, the average apparent crack speed is approximately 3300 m/s or 61% of the Rayleigh wave speed for the matrix which is the more compliant material in the two constituents in the composite. The local crack speed, on the other hand, is higher. Before crack branching at approximately 0.204  $\mu$ s, the propagation of a single crack is observed (Fig. 5a-b) and  $dl/dt$  represents the local crack tip speed. The average value of this local speed is approximately 6000 m/s. The plot shows that this speed approaches transonic levels, that is, above the Rayleigh wave and shear wave speeds of the matrix phase. Note that after branching two crack fronts are involved and the local crack tip speed for each is one half of what is seen in the profile. Therefore, the mean local crack tip speed is approximately 5500 m/s for each branch, well below the longitudinal wave speeds for the constituents (9939 and 10 694 m/s, respectively) and slightly lower than the mean local tip speed for the crack before branching. These results are consistent with the findings reported in Xu and Needleman [38,39] and the experimental measurements reported in Lambros et al. [40], Huang et al. [41] and Rosakis et al. [42] concerning crack propagation along bimaterial interfaces. Experimentally, apparent crack speeds in the intersonic range have been measured in carbon fiber/polymer matrix composites under impact loading, Rosakis et al. [43].

### *Effects of Different Microstructural Morphologies*

The results in Figs. 5-8 show that crack path is significantly influenced by the microstructural phase morphologies. Fracture occurs primarily along phase boundaries and inside the matrix. Continuous and favorably oriented interfaces (parallel to the direction of crack propagation) facilitate crack growth, see Fig. 8d. Crack branching occurs at different times and different distances of crack extension from the initial crack tip. Also note that no branching is seen in Fig. 6 for microstructure (b). Two other calculations are carried out under the same loading conditions using uniform matrix or grain material properties for the microstructural region in front of the crack tip. The results show that in both cases crack branching occurs after very short distances of crack propagation in the  $\xi^1$  direction from the pre-crack tip. Both distances are smaller than those observed in the composites here. These results demonstrate that material heterogeneities retard or prevent crack branching in composite microstructures. This observation is consistent with the same finding in Xu et al. [31] for

materials with inhomogeneous cohesive strengths but otherwise homogeneous bulk properties.

The time histories of the local crack speed  $d\ell/dt$  and apparent crack speed  $da/dt$  for all four cases shown in Fig. 10 indicate a range of crack initiation times for the microstructures, from 0.12 to 0.19  $\mu\text{s}$ . The microstructures have a clear impact on the fracture initiation time. Temporary arrest of crack propagation due to impediments of larger particles is also observed, see Fig. 9a,d and Fig. 10a,d. The apparent crack speed seems to oscillate around a mean value of approximately 3300 m/s or 61% of the Rayleigh wave speed for the matrix material in all microstructures. This average seems to be independent of the differences in the microstructural morphologies and phase sizes considered. In contrast, the local crack speed seems to be more significantly affected by the microstructural phase distributions. In Fig. 6 for microstructure (b), no branching occurs and the local speed reaches well into the intersonic range, that is the mean crack speed is well above the shear wave speeds of the constituents and approaches 9000 m/s or approximately 90% of the longitudinal wave speed of the matrix material, see Fig. 10b. Recall that this local speed represents the rate of change of arc length along crack paths and is not subject to the limit of physical wave speeds such as  $c_L$  and  $c_s$  of the bulk constituents. In Figs. 5, 7, and 8, crack branching occurs and the mean local crack speed for each tip Figs. 10a, c, and d is approximately 6000, 5800 and 7000 m/s for microstructures (a), (c), and (d), respectively. These values are lower than that in Fig. 10b. It appears that branching reduces local crack tip speeds while allowing overall rate of surface generation to increase.

#### Energy Release Rate

The evolutions of the kinetic energy  $\mathcal{K}$ , strain energy  $\mathcal{W}$ , and cohesive surface energy  $\Phi$  in the whole specimen for the four cases are shown in Fig. 11. The times of crack initiation are clearly signified by upturns in the curves for  $\Phi$  in (a), (c), and (d). In Fig. 11c, the crack arrests shortly after initiation. Earlier crack initiation allows more crack surfaces to be generated, resulting in more energy to be expended in the process (higher  $\Phi$ ) and less strain energy to be stored in the specimen (lower  $\mathcal{W}$ ). This is the case in Figs. 11a-c in which the crack initiation times are between 0.124 and 0.144  $\mu\text{s}$ . On the other hand, delayed crack initiation (Figs. 11d, approximately 0.192  $\mu\text{s}$ ) corresponds to less new crack surfaces and less energy consumption (lower  $\Phi$ ), leading to more strain energy stored in the specimen (higher  $\mathcal{W}$ ). Although crack branching has a clear signature in the profiles for  $\Phi$  and  $\mathcal{K}$  in Fig. 11a for microstructure (a), such an effect can not be easily identified in Figs. 11b-d for other microstructures.

To analyze the energy expended during fracture, the total crack surface energy  $\Phi_{\text{crack}}$  is calculated for each case. This energy is

$$\Phi_{\text{crack}} = \int_{S_{\text{crack}}} \phi_0(x) dS \quad (16)$$

where  $S_{\text{crack}}$  is defined as the part of the internal surface  $S_{\text{int}}$  that satisfies  $\phi(\Delta) \geq 0.99\phi_0$ . In the current analysis,  $\Phi_{\text{crack}}$  is calculated for the first 350  $\mu\text{m}$  of the total crack length  $\ell(t)$ , or for  $0 \leq \ell(t) \leq 350 \mu\text{m}$ . Note that it takes different amounts of time to reach this crack length in different microstructures. The calculated values of  $\Phi_{\text{crack}}$ , the apparent crack length  $a$ , and the time  $t$  at a total crack length of  $\ell = 350 \mu\text{m}$  for the four microstructures are listed in Table 3. Figure 12 compares the histories of  $\Phi_{\text{crack}}$  as function of  $\ell$  and the apparent crack length  $a$  for the four cases considered. This figure and the table show that there is a significant

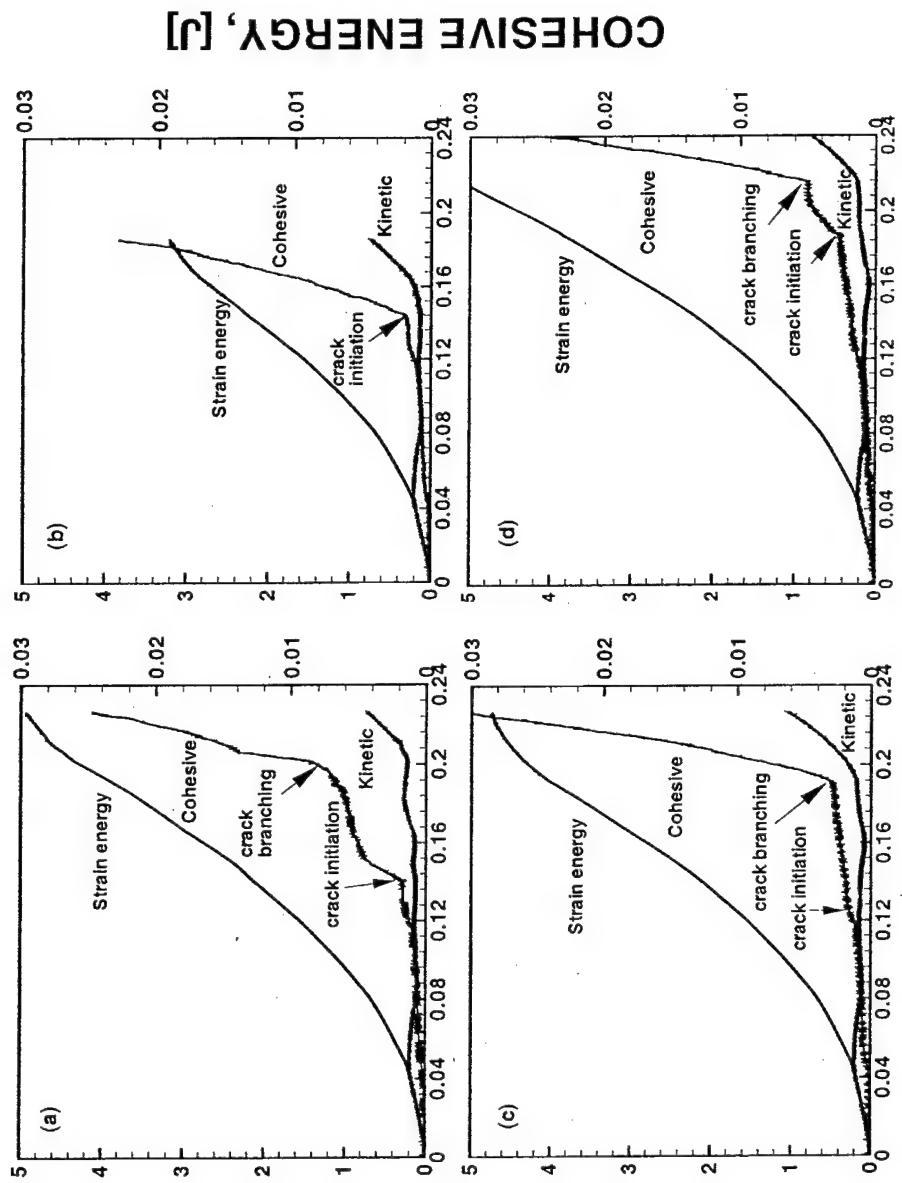


FIG. 11—A comparison of energy evolutions for the four microstructures.

TABLE 3—*Average energy release rates for different microstructures.*

Microstructure	Average size of $\text{TiB}_2$ , $\mu\text{m}$	$\Phi_{\text{crack}} \times 10^{-3}$ , $\text{J}$	Time, $\mu\text{s}$	$a(l)$ at $l = 350 \mu\text{m}$	$\frac{\partial \Phi_{\text{crack}}}{\partial l}$ , $\text{J/m}$	$\frac{\partial \Phi_{\text{crack}}}{\partial a}$ , $\text{J/m}$
(a)	10-20	12.5	0.23	122	35.7	102.5
(b)	8-10	11.0	0.19	142	31.4	77.5
(c)	1-2	10.3	0.22	102	28.6	98.0
(d)	$20 \times 100$	12.1	0.24	110	34.3	110.0

variation of fracture energy among the four microstructures. The waviness in the curves reflects the different values of work of separation  $\phi_0$  in different constituents and along matrix/reinforcement interfaces. The energy release rate or energy consumption per unit length of crack generated is

$$g = \frac{\partial \Phi_{\text{crack}}}{\partial l} \quad (17)$$

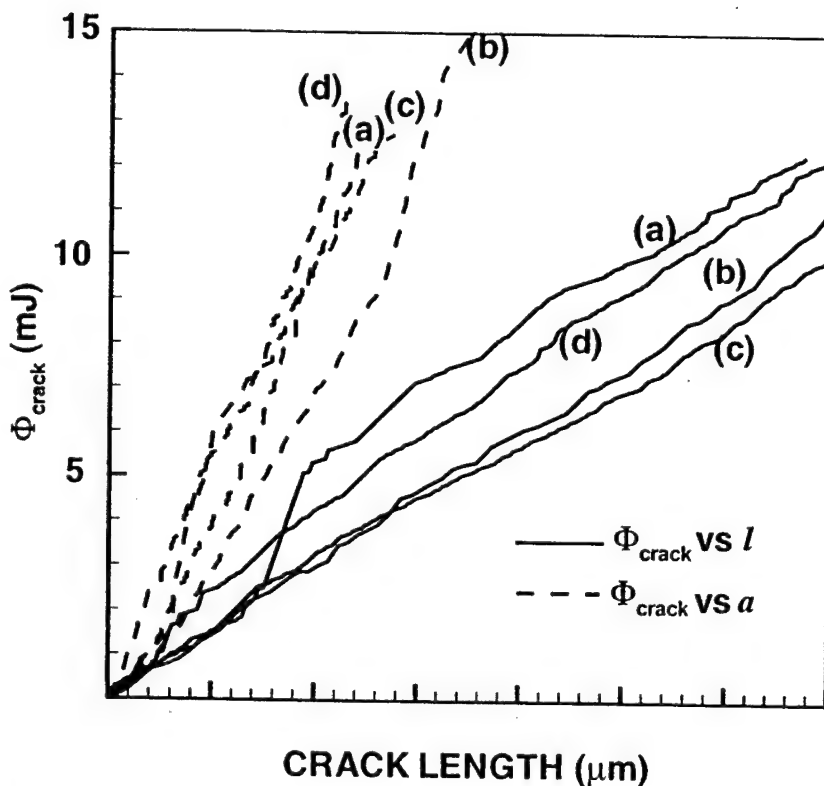


FIG. 12—*Fracture energy  $\Phi_{\text{crack}}$  as functions of local and apparent lengths for the four microstructures.*

When fracture occurs in the form of a single crack propagating solely in the horizontal direction,  $l = a$ ,  $G = \partial\Phi_{\text{crack}}/\partial l = \partial\Phi_{\text{crack}}/\partial a$  represents the energy release rate for crack propagation in the regular fracture mechanics sense. Figure 13 compares histories of the instantaneous energy release rate defined in Eq 17 as a function of  $l$  for the four cases analyzed. In these profiles, there are three characteristic levels which correspond to the works of separation inside the grains ( $\phi_0 = 135.9 \text{ J/m}^2$ ), inside the matrix ( $\phi_0 = 46.2 \text{ J/m}^2$ ) and along the matrix/reinforcement interfaces ( $\phi_0 = 15.4 \text{ J/m}^2$ ). Instantaneous  $G$  values between the above three levels occur when simultaneous fracture happens at multiple sites with different values of  $\phi_0$ . The profiles in the plot show that such incidents occur quite frequently for all four microstructures. Most of these are microcrack sites along the main crack path or paths seen in Figs. 5–8, since all four cases show only one main crack (Fig. 6) or one crack followed by two branches and no large scale microcracking is observed. It can be seen that  $G$  oscillates mainly between  $46.2 \text{ J/m}^2$  and  $15.4 \text{ J/m}^2$ , providing a quantitative measure for the observation made from Figs. 5–9 that crack propagation is primarily through the matrix and the phase boundaries. To facilitate comparison, the average values of  $\partial\Phi_{\text{crack}}/\partial l$  and  $\partial\Phi_{\text{crack}}/\partial a$  corresponding to the four profiles in Fig. 13 are listed in Table 3. Note that it takes different amounts of time for  $l$  to reach  $350 \mu\text{m}$  in different microstructures. For higher resistance to fracture, it is desirable to induce cracks to go through the hard  $\text{TiB}_2$  reinforcements, as seen in Fig. 5a and indicated by the spikes of  $G$  values up to  $135.9 \text{ J/m}^2$  in Fig. 13a. It can be seen that as the average size of  $\text{TiB}_2$  reinforcements is decreased from microstructures (a) to (c) the average energy release rate  $\partial\Phi_{\text{crack}}/\partial l$  decreases, reflecting decreasing amounts of crack growth in higher strength  $\text{TiB}_2$  or matrix in Figs. 13b and 13c. Indeed, Fig. 13c shows that no fracture occurs inside  $\text{TiB}_2$  in microstructure (c) for the duration analyzed. Also, there seems to be a higher fraction of fracture along matrix/grain interfaces that has the lowest work of separation among the three types of fracture sites. The larger sizes of the  $\text{TiB}_2$  reinforcements in microstructure (d) cause its average value of  $\partial\Phi_{\text{crack}}/\partial l$  to be higher. Clearly, there is significant fracture inside the  $\text{TiB}_2$  phase, as indicated in Fig. 13d. However, the existence of continuous and favorably oriented  $\text{TiB}_2/\text{Al}_2\text{O}_3$  boundaries inherent in the morphology of a network of  $\text{TiB}_2$  filled with  $\text{Al}_2\text{O}_3$  colonies also allow cracks to propagate along the interfaces with relatively low hindrance.

### Discussions

The results discussed above show that it is possible to change the fracture resistance of brittle composites by altering microstructural morphologies through favorable material processing conditions. It is conceivable that energy release rates higher than those calculated here may be achieved by other microstructural morphologies not considered since the four variations analyzed represent only a small sample of microstructural morphologies that can be produced by various methods of material synthesis. This analysis did not consider the effects of varying the bulk properties for each phase on the failure behavior of the composites. There are ample opportunities for performance enhancement through the use of constituents with dissipation mechanisms. The effects of various elasto-plastic constituents on fracture should be characterized in future analyses. Interfacial bonding strength between the phases is another factor that can significantly influence the behavior of the materials. In a related analysis, it is found that under certain loading rates this interphase bonding plays a role in determining the characteristics of fracture or the mode of fracture in the  $\text{TiB}_2/\text{Al}_2\text{O}_3$  composites, Zhai et al. [35]. Specifically, when weak interfacial strength exists, microcrack initiation and growth are the principal mode of failure; whereas when strong interfacial strength is derived from material processing, the advancement of a dominant crack and crack branching are observed. It is expected that the fracture behavior of heterogeneous materials

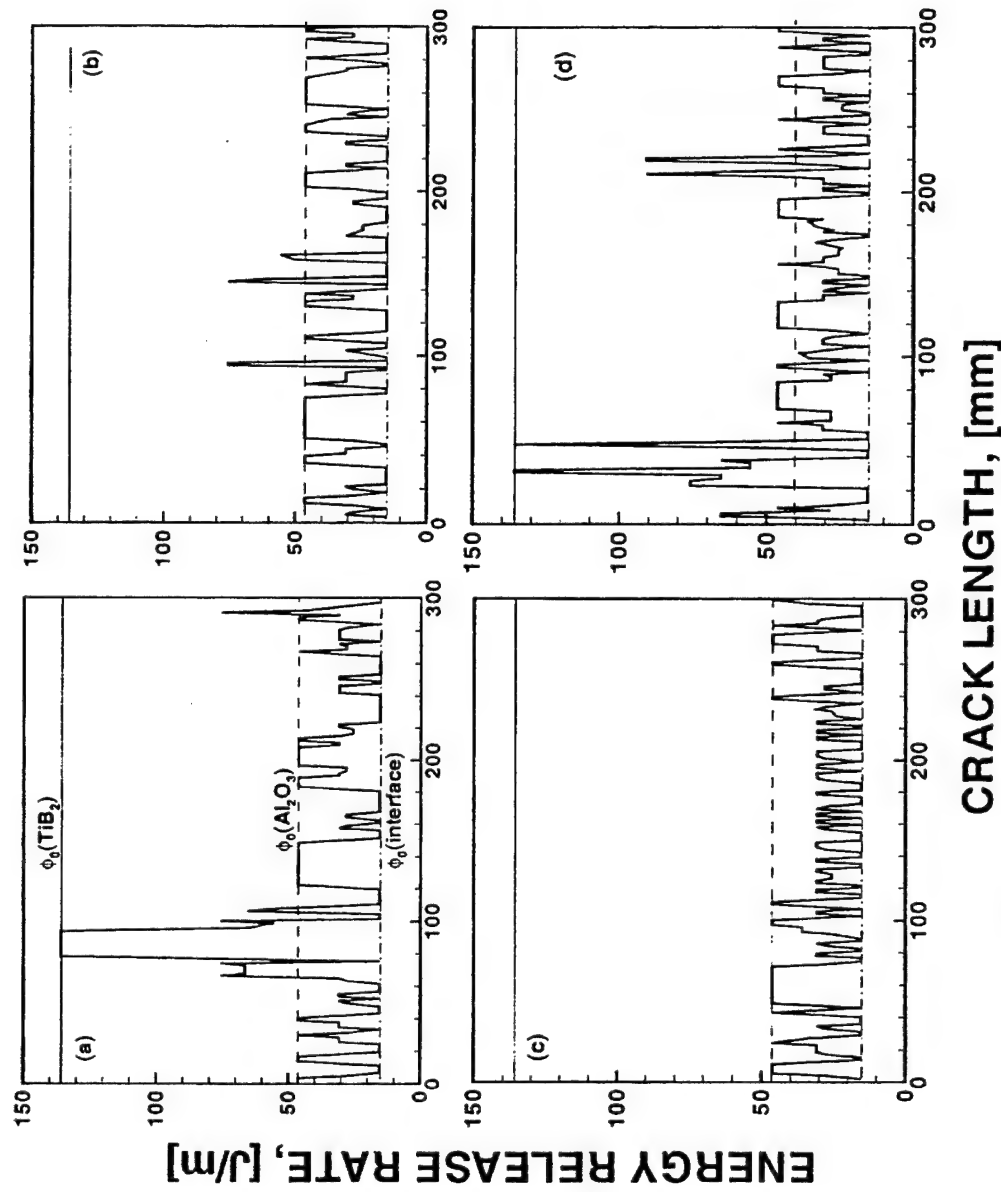


FIG. 13—Energy release rate as functions of local and apparent crack lengths for the four microstructures.

is also loading rate sensitive due to the rate-dependence of bulk constituent behavior and inertia. These issues shall be addressed in future publications.

A micromechanical model that provides explicit account for arbitrary microstructures and arbitrary is used here. The approach incorporates both a constitutive law for the bulk solid constituents and a constitutive law for fracture surfaces. The interfacial separation law can be regarded as a phenomenological characterization of atomic interaction forces. This approach is especially appropriate for analyzing microscopic fracture over a range of length scales because (i) material separation is a natural outcome of bulk constitutive response, interfacial behavior, microstructure, and loading; and (ii) the formulation is free from any fracture initiation, growth, and coalescence criteria that are necessary in most other continuum analyses, therefore circumventing the limitations of failure criteria that are valid only over certain length scales, such as continuum criteria based on the existence of  $K$ -fields. This framework allows for a unified treatment of mix-mode fracture without resorting to the differentiation of fracture into separate modes. The elimination of the need for ad hoc criteria is accompanied by the introduction of the need for interfacial separation laws at various microscopic settings of interest. Therefore, an important task is the development of interfacial constitutive laws appropriate for specific materials and length scales. For specific forms of cohesive laws, the determination of cohesive parameters for constituents is another relevant issue. For example, over a certain size scale the calibration of model parameters by assuming  $\phi_0 = (1 - v^2)K_{IC}^2/E$  may be justifiable for brittle constituents. However, the same assumption may become indefensible if the objective is to quantify nano-scale fracture mechanisms. Indeed, there is a serious lack of experimental characterization as well as understanding for interfacial constitutive behaviors on the sub-micron length scales. Issues include, among others, dissipation in the separation process and the gradient-dependence of traction along interfaces. Kim [44] proposed a relation for interface decohesion that accounts for nonlocal effects on the nano-scale. Significant challenges and opportunities exist for experimental and analytical research on nano-scale and micro-scale interfacial separation mechanisms. As such separation laws are made available and as long as appropriate bulk response laws are used including the quasi-continuum formulation of Tadmor et al. [45], the unique framework off analysis employed here represents a systematic and consistent approach for explicit modeling of fracture over a wide range off length scales.

### Conclusions

The dynamic failure behavior in a class of  $\text{Al}_2\text{O}_3/\text{TiB}_2$  composites is analyzed in the context of fracture in a centered-cracked specimen under remote tensile loading. Numerical simulations are carried out under the conditions of plane strain. A micromechanical framework of analysis has been developed and used, providing an explicit account for arbitrary material microstructural morphologies and resolution for arbitrary, unconstrained fracture patterns. The approach combines constitutive description of bulk material responses and characterization of fracture surface cohesion. The framework of analysis allows mixed-mode fracture behavior of materials with composite microstructures to be examined without resorting to any mode-dependent fracture initiation or propagation criteria. In this analysis, both the bulk and the interfacial constitutive laws are assumed to be hyperelastic. The results of numerical simulations demonstrated the microscopic phase distribution and phase size scale can significantly influence the fracture behavior. Due to their higher cohesive strength and therefore higher energy release rate,  $\text{TiB}_2$  reinforcements represent stronger obstacles to the growth of cracks and increase the energy required in generating the same amount of crack surfaces. The increase in fracture resistance is higher in microstructures with larger

TiB<sub>2</sub> particles. A 25% variation in average energy release rate is observed for the four microstructures of actual Al<sub>2</sub>O<sub>3</sub>/TiB<sub>2</sub> composites prepared by high-temperature synthesis.

#### Acknowledgment

Support from the Army Research Office through grant DAAG55-98-1-0454 is gratefully acknowledged. Calculations reported are carried out on the Cray Computers at the San Diego Supercomputer Center, Jet Propulsion Laboratory and the Goddard Space Center. M. Zhou would like to thank A. Needleman and X.-P. Xu for helpful discussions. Thanks are extended to K. V. Logan for providing micrographs of Al<sub>2</sub>O<sub>3</sub>/TiB<sub>2</sub> composites used in this research.

#### References

- [1] Shockley, D. A., Curran, D. R., Seaman, L., Rosenberg, J. T., and Peterson, S. F., "Fragmentation of Rock Under Dynamic Loads," *International Journal of Rock Mechanics*, Vol. 11, 1974, pp. 303-317.
- [2] Grady, D. E. and Kipp, M. E., "The Micromechanics of Impact Fracture of Rock," *International Journal of Rock Mechanics*, Vol. 16, 1979, pp. 293-302.
- [3] Lankford, J., "Dynamic Compressive Fracture in Fiber-reinforced Ceramic Matrix Composites," *Material Science and Engineering A: Structural Materials: Properties, Microstructure and Processing*, Vol. A107, 1989, pp. 261-268.
- [4] Shockley, D. A., Seaman, L., and Curran, D. R., "The Micro-Statistical Fracture Mechanics Approach to Dynamic Fracture Problems," *International Journal of Fracture*, Vol. 27, 1985, pp. 145-157.
- [5] Brockenbrough, J. R., Suresh, S., and Duffy, J., "An Analysis of Dynamic Fracture in Microcracking Solids," *Philosophy Magazine A*, Vol. 58, 1988, pp. 619-634.
- [6] Longy, F. and Cagnoux, J., "Plasticity and Microcracking in Shock-loaded Alumina," *Journal of American Ceramic Society*, Vol. 72, 1989, pp. 971-979.
- [7] Kishi, T., Takeda, N., and Kim, B. N., "Dynamic Fracture Toughness and Microstructural Fracture Mechanisms in Ceramics," *Ceramic Engineering and Science Process*, Vol. 11, No. 7-8, 1990, pp. 650-664.
- [8] Curtin, W., "Theory of Mechanical Properties of Ceramic-Matrix Composites," *Journal of American Ceramic Society*, Vol. 74, 1991, pp. 2837-2845.
- [9] Shockley, D. A., Machand, A. H., Skaggs, S. R., Cort, G. E., Burkett, M. W., and Parker, R., "Failure Phenomenology of Confined Ceramic Targets and Impact Rods," *International Journal of Impact Engineering*, Vol. 9, 1990, pp. 263-275.
- [10] Suresh, S., Nakamura, T., Yeshurun, Y., Yang, K. H., and Duffy, J., "Tensile Fracture Toughness of Ceramic Materials: Effects of Dynamic Loading and Elevated Temperatures," *Journal of American Ceramic Society*, Vol. 73, 1990, pp. 2457-2466.
- [11] Yang, K. -H. and Kobayashi, A. S., "Dynamic Fracture Response of Alumina and Two Ceramic Composites," *Journal of American Ceramic Society*, Vol. 73 No. 8, 1990, pp. 2309-2315.
- [12] Evans, A. G., "The Mechanical Properties of Reinforced Ceramic, Metal and Intermetallic Matrix Composites," *Material Science and Engineering*, Vol. A143, 1991, pp. 63-76.
- [13] Kishi, T., "Dynamic Fracture Toughness in Ceramic and Ceramics Matrix Composites," *Engineering Fracture Mechanics*, Vol. 40, 1991, pp. 785-790.
- [14] Kobayashi, A. S., "Dynamic Fracture of Ceramics and Ceramic Composites," *Materials Science and Engineering*, Vol. A143, 1991, pp. 111-117.
- [15] Espinosa, H. D., Raiser, G., Clifton, R. J., and Ortiz, M., "Experimental Observation and Numerical Modeling of Inelasticity in Dynamic Loaded Ceramics," *Journal of Hard Materials*, Vol. 3, 1992, pp. 285-313.
- [16] Ahrens, T. J. and Rubin, A. M., "Impact-Induced Tensional Failure in Rock," *Journal of Geophysics Research*, Vol. 98, 1983, pp. 1185-1203.
- [17] Vekinis, G., Ashby, M. F., Shercliff, H., and Beaumont, P. W., "The Micromechanics of Fracture of Alumina and Ceramic-Based Fiber Composite: Modeling the Failure Processes," *Composites Science and Technology*, Vol. 48, 1993, pp. 325-330.
- [18] Lankford, J., "Effect of Hydrostatic Pressure and Loading Rate on Compressive Failure of Fiber-Reinforced Ceramic-matrix Composites," *Compos. Sci. Tech.*, Vol. 51, 1994, pp. 537-543.

- [19] Woodward, R. L., Gooch, W. A., O'Donnell, R. G., Oerciballi, W. J., Baxter, B. J., and Oattie, S. D., "A Study of Fragmentation in the Ballistic Impact of Ceramics," *International Journal of Impact Engineering*, Vol. 15, 1994, pp. 605-618.
- [20] Zhou, S. J. and Curtin, W. A., "Failure of Fiber Composites: A Lattice Green Function Model," *Acta Metallurgica Material*, Vol. 43, 1995, pp. 3093-3104.
- [21] Seaman, L., Curran, D. R., and Murri, W. J., "A Continuum Model for Dynamic Tensile Microstructure and Fragmentation," *Journal of Applied Mechanics*, Vol. 52, 1985, pp. 593-600.
- [22] Curran, D. R., Seaman, L., and Shockley, D. A., "Dynamic Failure of Solids," *Physics, Reports*, Vol. 147, 1987, pp. 253-388.
- [23] Curran, D. R., Seaman, L., Cooper, T., and Shockley, D. A., "Micromechanical Model for Continuum and Granular Flow of Brittle Materials Under High Strain Rate Application to Penetration of Ceramic Targets," *International Journal of Impact Engineering*, Vol. 13, 1993, pp. 53-58.
- [24] Rajendran, A. M., "Modeling the Impact Behavior of AD85, Ceramic under Multiaxial Loading," *International Journal of Impact Engineering*, Vol. 15, 1994, pp. 749-768.
- [25] Johnson, G. R. and Holmquist, T. J., "Computational Constitutive Model for Brittle Materials Subjected to Large Strains, High Rates, and High Pressure," M. A. Meyers, L. E. Murr, and K. P. Staudhammer, Editors, *Shock Wave and High Strain Rate Phenomena in Materials*, 1992, pp. 1075-1081.
- [26] Walter, J., "Material Loading for Terminal Ballistic Simulation, Technical Report," U.S. Army Research Lab., MD, 1992.
- [27] Espinosa, H. D. and Brar, N. S., "Dynamic Failure Mechanisms of Ceramic Bars: Experiments and Numerical Simulations," *Journal of Mechanics and Physics of Solids*, Vol. 43, 1995, pp. 1615-1638.
- [28] Ravichandran, G. and Subhash, G., "A Micromechanical Model for High Strain Rate Behavior of Ceramics," *International Journal of Solids and Structures*, Vol. 32, 1995, pp. 2627-2646.
- [29] Gao, H. J. and Klein, P., "Numerical Simulation of Crack Growth in an Isotropic Solid with Randomized Cohesive Bonds," *Journal of Mechanics and Physics of Solids*, Vol. 46, 1998, pp. 187-218.
- [30] Xu, X.-P. and Needleman, A., "Numerical Simulations of Fast Crack Growth in Brittle Solids," *Journal of Mechanics and Physics of Solids*, Vol. 42, 1994, pp. 1397-1434.
- [31] Xu, X.-P., Needleman, A., and Abraham, F. F., "Effect of Inhomogeneities of Dynamic Crack Growth in an Elastic Solid," *Modeling & Simulation Materials Science and Engineering*, Vol. 5, 1997, pp. 489-516.
- [32] Camacho, G. T. and Ortiz, M., "Computational Modeling of Impact Damage in Brittle Materials," *International Journal of Solids and Structures*, Vol. 33, No. 20-22, 1996, pp. 2899-2983.
- [33] Ortiz, M., "Computational Micromechanics," *Computational Mechanics*, Vol. 18, 1996, pp. 321-338.
- [34] Logan, K. V., "Composite Ceramics, Final Technical Report," USSTACOM DAAE07-95-C-R040, 1996.
- [35] Zhai, J. and Zhou, M., "Finite Element Analysis of Micromechanical Failure Modes in Heterogeneous Brittle Solids," *International Journal of Fracture*, special issue on failure modes in solids, 1998.
- [36] Krieg, R. D. and Key, S. W., "Transient Shell Response by Numerical Time Integration," *International Journal of Numerical Method in Engineering*, Vol. 7, 1973, pp. 273-286.
- [37] Belytschko, T., Chiapetta, R. L., and Bartel, H. D., "Efficient Large Scale Non-linear Transient Analysis by Finite Elements," *International Journal of Numerical Method in Engineering*, Vol. 10, 1976, pp. 579-596.
- [38] Xu, X.-P. and Needleman, A., "Numerical Simulations of Dynamic Interfacial Crack Growth Allowing for Crack Growth Away From the Bond Line," *International Journal of Fracture*, Vol. 74, 1995, pp. 253-275.
- [39] Xu, X.-P. and Needleman, A., "Numerical Simulations of Dynamic Crack Growth Along an Interface," *International Journal of Fracture*, Vol. 74, 1996, pp. 289-324.
- [40] Lambros, J. and Rosakis, A. J., "Shear Dominated Transonic Interfacial Crack Growth in a Bimaterial—I. Experimental Observations," *Journal of Mechanics and Physics of Solids*, Vol. 43, 1995, pp. 169-188.
- [41] Huang, Y., Wang, W., Liu, C., and Rosakis, A. J., "Intersonic Interfacial Crack Growth in a Bimaterial: An Investigation of Crack Face Contact," *Journal of Mechanics and Physics of Solids*, 1998, in press.
- [42] Rosakis, A. J., Samudrala, O., and Singh, R. P., and Shukla, A., "Intersonic Crack Propagation in Bimaterials," *Journal of Mechanics and Physics of Solids*, in press, 1998.

- [43] Rosakis, A. J., Liu, C., Stout, M. G., and Lambros, J., "Dynamic Fracture of Unidirectional Composites," IMECE, Nov. 16-21, 1997, manuscript in preparation.
- [44] Kim, K. S., "Nanomechanics of defects in crystalline solids," in preparation.
- [45] Tadmor, E. B., Ortiz, M., and Phillips, R., "Quasicontinuum Analysis of Defects in Solids. *Philosophy Magazine*," Vol. 73, 1996, pp. 1529-1563.